5-24-2012

Information processing in a midbrain visual pathway

Dihui Lai
Washington University in St. Louis

Department of Physics

Dissertation Examination Committee:
Ralf Wessel, Chair
Dennis Barbour
Anders E. Carlsson
Zohar Nussinov
Barani Raman
Li Yang

INFORMATION PROCESSING IN A MIDBRAIN VISUAL PATHWAY

by
Dihui Lai

A dissertation presented to the
Graduate School of Arts and Sciences
of Washington University in Saint Louis
in partial fulfillment of the
requirements for the degree of
Doctor of Philosophy in Physics

May 2012

Saint Louis, Missouri

Abstract

Visual information is processed in brain via the intricate interactions between neurons. We investigated a midbrain visual pathway (optic tectum and its isthmic nucleus) that is motion sensitive and is thought as part of attentional system. We determined the physiological properties of individual neurons as well as their synaptic connections with intracellular recordings. We reproduced the center-surround receptive field structure of tectal neurons in a dynamical recurrent feedback loop. We reveal in a computational model that the anti-topographic inhibitory feedback could mediate competitive stimulus selection in a complex visual scene. We also investigated the dynamics of the competitive selection in a rate model. The isthmotectal feedback loop gates the information transfer from tectum to thalamic rotundus. We discussed the role of a localized feedback projection in contributing to the gating mechanisms with both experimental and numerical approaches. We further discussed the dynamics of the isthmotectal system by considering the propagation delays between different components. We conclude that the isthmotectal system is involved in attention-like competitive stimulus selection and control the information coding in the motion sensitive SGC-I neurons by modulating the retino-tectal synaptic transmission.

Acknowledgments

I would like to thank Ralf Wessel for his supervision and the opportunity of joining the group. His passion, and scientific insight have been truly encouraging and inspiring.

I thank Anders E. Carlsson and Zohar Nussinov for the guidance and collaboration.

I also want to thank the other members of my dissertation examination committee: Dennis Barbour, Barani Raman and Li Yang.

I owe thanks to Sebastian Brandt, Jing Shao, Matthew Caudill, Debajit Saha, David Morton, Adam Eggebrecht, Jeff Post, Thomas Crockett, for good advices and enjoyable collaborations.

I thank Seth Waldecker for proof reading the thesis.

Last but not least, I thank my family for their caring and support.

Contents

List of Figures

List of Tables

1 Introduction

Information is processed in brains through complex interactions between neurons. Neural connections, forming through chemical synapses or electric gap-junctions, play a fundamental role in determining the activity of the neural network. Dependent on the transmitter released, the neural activity at the presynaptic site could either excite or inhibit the response of postsynaptic neurons. For example, the involvement of glutamate usually leads to depolarization of membrane potential while γ-aminobutyric acid (GABA) is a major inhibitory neurotransmitter in the central nervous system (Koch and Segev, 1998). Synaptic dynamics such as long-term/short-term plasticity, spike-timing-dependent plasticity enable the neural network to accomplish even more complicated behavior such as adaptation and memories. Third party neural transmitter such as acetylcholine (ACh), norepinephrine, dopamine etc., might further modulate the way neurons interacting with each other (Bear et al., 2007). For examples, ACh could enhance the synaptic efficacy between the pre-post neurons (Kawai et al., 2007); Dopamine is involved in altering spike-timing-dependent plasticity (Pawlak et al., 2010). A fundamental question of neuroscience is to understand the role of these interactions in deciding the behavior of neural networks (e.g. rhythmic oscillation, multi-stability) and how the network behavior is related to the macroscopic behaviors of animals (e.g. adaptive behavior, attention, learning).

Together with the cellular and synaptic properties, topological organizations of neural connections are significant in controlling information flow and determining how

information is encoded in neural networks. Recurrent excitatory loops formed between excitatory interneurons determine the bursting activity that drives lamprey locomotion (Grillner, 2003). Recurrent excitation-inhibition organization has been proposed to operate as a coincidence detector in mammalian hippocampus (Buhl et al., 1994). Lateral inhibitions are regarded as an anatomical structure that can serve as a maxima detector (Mao and Massaquoi, 2007). Another striking feature of the brain is the strong feedback delivered from the areas where the neurons send their axons. In the primary visual cortex, neural feedback dominates in certain regions, indicating that the sensory inputs at low-level visual system are greatly influenced by high-level neural activities (Sillito et al., 2006). The understanding of circuit algorithm that is carried by neural connectivity and interactions among their components is also fundamental to neuroscience (Yuste 2008).

We investigated a midbrain visual pathway, consisting of optic tectum (OT) and its satellite isthmic nucleus, which is thought as an attentional control component besides the forebrain networks (Knudsen, 2011). Specifically, a type of wild-field neuron termed stratum griseum centrale (SGC) receives retina efferent from the superficial layer of OT and sends visual information further to the thalamic nucleus rotundus. Neural activities of the tectofugal pathway are modulated by the feedback from isthmic magnocellularis (Imc), parvocellularis (Ipc), and semilunaris (SLu) nucleus. Immunocytochemical staining reveals that two major types of feedback connections are involved in the pathway i.e. topographically organized local cholinergic projections from Ipc/SLu and anti-topographically organized global GABAergic projections from Imc (Wang et al., 2004, 2006). The tectal neuron is motion sensitive and the isthmotectal system is

engaged in competitive selection of salient stimulus in a complex visual scene (Marin et al., 2007; Asadollahi et al., 2010, 2011; Mysore et al., 2010). The response of tectal neuron is also biased by feedback projection from high-level area such as arcopallial gaze field (AGF, Winkowski and Knudsen, 2006, Winkowski and Knudsen, 2008). We investigated the tectofugal pathway and its isthmotectal feedback loop with whole cell recordings and computational modeling. We discussed in different chapters the receptive field organizations of tectal neurons, the rhythmic oscillatory bursting activity observed in the system, the dynamics of competitive interactions and the modulatory effect of the local Ipc feedback.

This dissertation contains seven chapters based on the following papers published in scientific journals and manuscripts in preparation

- Chapter 2: Lai D and Wessel R A dynamical recurrent neural network reproduces the characteristic center/surround response profile (In preparation)
- Chapter 3: Shao J, Lai D, Meyer U, Luksch H, Wessel R (2009) Generating oscillatory bursts from a network of regular spiking neurons without inhibition. J Comput Neurosci 27:591–606
- Chapter 4: Lai D, Brandt S, Luksch H, Wessel R (2011) Recurrent antitopographic inhibition mediates competitive stimulus selection in an attention network. J Neurophysiol 105: 793–805.
- Chapter 5: Lai D, Wessel R. Competitive selection and local feedback modulate population coding of motion-sensitive wild-field neurons (in preparation).

- Chapter 6: Lai D, Carlsson AE, Wessel R. The dynamics of novelty preference in a competitive neural network with adaptation (in preparation).
- Chapter 7: Lai D, Carlsson AE, Nussinov Z, Wessel R. Stability of a three-neuron system with delayed feedback (in preparation).

The receptive field (RF) of a neuron describes an area in the visual space where the presence of a stimulus could evoke the response of the neuron. Classical RFs of center surrounding structure were discovered in retina as well as the primary visual cortex (Kuffler, 1953; Hubel and Wiesel, 1959). A computational model that describes the RF organization by two Gaussian filters is firstly introduced (Rodieck, 1965) and successfully explained the response of retina ganglion cells to motion. This model approach is then wildly applied to similar center-surround RF structure (Soodak, 1986; Cavanaugh et al., 2002) due to its mathematical simplicity and success in explaining experimental data. However, the phenomenological model provides little understanding of the circuit dynamics underlying the RF structure and fails to capture the RF properties such as context dependent (David et al., 2004), contrast dependent (Enroth-Cugell and Robson, 1966; Sceniak et al., 1999) and nonlinearity (Hochstein and Shapley, 1976). In Chapter 2: we reproduced neuronal center/surround RF in a network with recurrent excitation and inhibition. Different from the difference-of-Gaussian (DOG) description, the recurrent network has a global inhibitory feedback instead of locally distributed Gaussian feedforward inhibition. The observed neural center/surrounding RF structure results from the interaction between the excitatory and inhibitory neuron group.

In Chapter 3: We established a neural network composed of tectal L10 and Ipc neurons and reproduced the *in vivo* observed oscillatory bursts of Ipc cells in response to visual stimulation (Marin et al., 2007). While depolarized by step current injections, both L10 and Ipc neurons respond with regular tonic spikes. The neurons show high frequency spiking at the onset of the stimulus and then adapts to a steady state with relatively low firing frequency. We demonstrate in a computational model that oscillatory burst generation at Ipc neurons can be caused by strong and brief feedforward synaptic conductance changes led by the L10 activities. The mechanism is sensitive to spike-rate adaptation. Moreover, the bursting activity is dependent on the correlation in the presented stimuli.

The isthmotectal system competitively selects the most salient stimulus (Marin et al., 2007; Asadollahi et al., 2010, 2011; Mysore et al., 2010) in a complex visual scene. Winner-take-all (WTA) circuit is proposed as the underlying mechanism that subserves the competitive selection. However, classical discussion of WTA circuit has been focused on its functional role as a maxima detector (Mao and Massaquoi, 2007). Its response to dynamical stimulation profile is still poorly understood. In Chapter 4, we investigated an experimentally constrained model where the tectal L10, Ipc and Imc neurons are considered. Various experimental observations are reproduced and predictions are made. We illustrate in the model that the antitopographic inhibitory feedback from Imc neurons mediates winner-take-all mechanisms and enable the network to select globally the strongest stimulus in the visual field. This network is also capable of selecting among the multiple stimuli the most novel one with the facilitation of cellular spike rate adaptation.

Top-down input from forebrain area biases the competitive stimulus selection via its control over the local excitatory and antitopographic inhibitory circuits.

The competitive interactions within isthmotectal system determine the activity of Ipc neurons, the rhythmic bursts of which are found to gate the signal transferring from OT to higher area in the brain e.g. rotundus, entopallium (Marin et al., 2012). Inactivation of Ipc activities impairs the neural responses at the high visual areas. In Chapter 5, we investigated the role of this localized feedback in motion processing with both *in vitro* whole cell recordings and computational modeling. Pulse stimulation at the superficial layer of tectal slices triggers the spiking response of tectal SGC-I neurons in a probabilistic manner (Luksch et al., 2004). The dynamical response suggests the involvement of certain depression mechanisms in retino-tectal transmissions. To further understand the role of Ipc feedback in determining the transmission, we bath applied mecamylamine, an antagonist of nicotinic acetylcholine receptor (nAChR). The recorded change of response implies the blockage of nAChRs slows the recovery speed of retino-SGC synapses from depression. Tectal neurons respond to Ipc stimulation with excitatory EPSPs and spikes. We show that the application of CNQX greatly reduced the response of tectal neurons and the experimental results are consistent with the observation that both cholinergic and glutamatergic pathways are involved in Ipc feedback (Wang et al., 1995; Wang 2003). We illustrate the role of Ipc feedback in motion processing by establishing a model network of the retino-tecto-rotundal pathway and the isthmotectal pathway. We show that the cholinergic feedback of Ipc neurons modulates divisively the response of tectal SGC-I neurons and the very same mechanisms can cause divisive

inhibition (Asadollahi et al., 2011). We also argue that the involvement of a strong Ipc feedback could induce coherent activities across the SGC-I population.

Neurons encode the information of surrounding environment into different patterns of action potentials. The number of action potential occurrence within a unit time window is termed firing rate. In Chapter 2-5, we build neural networks of spiking neuron by specifically considering the occurrence of action potentials. However, it is not always necessary to model the neuron activities with this detail. In Chapter 6 and Chapter 7, we simplify the computational models by considering only neural firing rate and reveal the properties of isthmotectal system from dynamic perspectives.

In Chapter 6, we constructed a network with two neurons mutually inhibiting each other. The model is designed as a simplified version of the competitive network considered in Chapter 4. Stimuli of two different scenarios are considered: static scene and dynamic scene. In a static scene, two stimuli are presented simultaneously while in a dynamic scene the two stimuli are presented in sequential order. We demonstrated that a two dimensional system is sufficient to reproduce WTA selection in a static scene. With weak mutual inhibitions, the network acts in a dynamic region where the neural activity triggered by the two stimuli suppress each other. As the inhibition increases, the network undergoes a nonlinear bifurcation and enables the network to select the stronger stimulus. In a dynamical scene, the parameters associated with the adaptation behavior are critical for novelty preference selection. We show that intermediate adaptation facilitates the

network to select between two stimuli the novel one while weak or strong adaptation leads to WTA and oscillatory behavior respectively.

In Chapter 7, we consider the dynamics of the isthmotectal system by constructing a neural network of three neurons that represent L10, Ipc, and Imc respectively. Propagation delays are introduced and the system is described by a three-dimensional delayed differential equations (DDE) set. We analyzed the stability of the three-neuron system. Rich dynamics (stable oscillation, multi-stability) appear as synaptic strengths vary. The stable region shrinks as the delay increases.

Reference

Asadollahi A, Mysore SP, Knudsen EI (2010) Stimulus-driven competition in a cholinergic midbrain nucleus. Nat Neurosci 13:889-896.

Asadollahi A, Mysore SP, Knudsen EI (2011) Rules of competitive stimulus selection in a cholinergic isthmic nucleus of the owl midbrain. J Neurosci 37:6088-6097.

Bear MF, Connors BW, Paradiso MA (2007) Neuroscience: exploring the brain. Baltimore MD: Lippincott Williams & Wilkins.

Buhl EH, Halasy K, Somogyi P (1994) Diverse sources of hippocampal unitary inhibitory postsynaptic potentials and the number of synaptic release sites. Nature 368:823-828.

Cavanaugh JR, Bair W, Movshon JA (2002) Nature and interaction of signals from the receptive field center and surround in macaque V1 neurons. J Neurophysiol 88:2530-2546.

Desimone R, Duncan J (1995) Neural mechanisms of selective visual attention. Ann Rev Neurosci 18:193-222.

David SV, Vinje WE, Gallant J (2004) Natural stimulus statistics alter the receptive field structure of V1 neurons. J Neurosci 24:6991-7006.

Enroth-Cugell Ch, Robson JG (1966) The contrast sensitivity of retinal ganglion cells of the cat. J Physiol 187: 517-552.

Gonzalo JM, Duran E, Morales C, Gonzalez-Cabrera C, Sentis E, Mpodozis J, Letelier JC (2012). Attentional capture? Synchronized feedback signals from the isthmi boost retinal signals to higher visual areas. J Neurosci 32: 1110-1122.

Grillner S (2003) The motor infrastructure: from ion channels to neuronal networks. Nat Rev Neurosci 4:573-586.

Hubel DH, Wiesel TN (1959) Receptive fields of single neurons in the cat's striate cortex. J Physiol 148:574-591.

Hochstein S, Shapley RM (1976) Linear and nonlinear spatial subunits in Y cat retinal ganglion cells. J Physiol 262:265-284.

Knudsen EI (2007) Fundamental components of attention. Annu Rev Neurosci 30:57-78.

Koch C, Segev I (1998) Methods in neuronal modeling from ions to networks. Cambridge, MA: MIT press.

Knudsen EI (2011) Control from below: the role of a midbrain network in spatial attention. European Journal of Neuroscience 33:1961-1972.

Kuffler SW (1953) Dsicharge patterns and functional organization of mammalian retina, J. Neurophysiol. 16:37-68.

Luksch H, Khanbabaie R, Wessel R (2004) Synaptic dynamics mediate sensitivity to motion independent of stimulus details. Nat Neurosci 7:380-388.

Kawai H, Lazar R, Metherate R (2007) Nicotinic control of axon excitability regulates thalamocortical transmission. Nat Neurosci 10:1168-1175.

Mysore SP, Asadollahi A, Knudsen EI (2010) Global inhibition and stimulus competition in the owl optic tectum. J Neurosci 30:1727-1738.

Mao ZH, Massaquoi SG (2007) Dynamics of winner-take-all Competition in recurrent neural networks with lateral inhibition. IEEE Trans on Neural Netw 18:55-69.

Marin G, Salas C, Sentis E, Rojas X, Letelier JC, Mpodozis J (2007) A cholinergic gating mechanism controlled by competitive interactions in the optic tectum of the pigeon. J Neurosci 27:8112-8121.

Pawlak V, Wickens JR, Kirkwood A, Kerr JND (2010) Timing is not everything: neuromodulation opens the STDP gate. Frontier in synaptic neuroscience 146: 1-14.

Sceniak MP, Ringach DL, Hawken MJ, Shapley R (1999) Contrast's effect on spatial summation by macaque V1 neurons. Nat Neurosci 2: 733-739.

Sillito AM Cudeiro J and Jones HE (2006) Always returning: feedback and sensory processing in visual cortex and thalamus. Trends Neurosci 29:307-316.

Soodak R (1986) Two-dimensional modeling of visual receptive fields using Gaussian subunits. Proc Natl Acad Sci 83:9259-9263.

Wang Y, Major DE, Karten HJ (2004) Morphology and connections of nucleus isthmi pars magnocellularis in chicks (gallus gallus). J Comp Neurol 469:275-297.

Wang Y, Luksch H, Brecha NC, Karten HJ (2006) Columnar projections from the cholinergic nucleus isthmi to the optic tectum in chicks (gallus gallus): a possible substrate for synchronizing tectal channels. J Comp Neurol 494:7–35.

Winkowski DE, Knudsen EI (2006) Top-down gain control of the auditory space map by gaze control circuitry in the barn owl. Nature 439:336-339.

Winkowski DE, Knudsen EI (2008) Distinct Mechanisms for Top-Down Control of Neural Gain and Sensitivity in the Owl Optic Tectum. Neuron 60:698-708.

Wang SR, Wu GY, Felix D (1995) Avian Imc-tectal projection is mediated by acetylcholine and glutamate. NeuroReport 6:757-760.

Wang SR (2003) The nucleus isthmi and dual modulation of the receptive field of tectal neurons in non-mammals. Brain Research Reviews 41:13–25.

Yuste R (2008) Circuit neuroscience: the road ahead. Frontier in Neuroscience 2:6-9.

2 A dynamical recurrent neural network reproduces the characteristic center/surround response profile

Receptive field (RF) describes a spatial region where the presence of a stimulus can evoke the response of a neuron. Center/surround organized RF is found common throughout the whole visual system and is normally considered as a structure resulted from feedward excitation and inhibition. Here we investigated a circuitry model and reveal that the characteristic response of a center/surround RF could be reproduced through the dynamics of an interactive network with local excitation and global inhibition. This model also predicts stimulus dependent behavior of a RF structure.

2.1 Introduction

Antagonistic center/surround RF is common throughout the visual pathway (Kuffler, 1953; Hubel and Wiesel, 1959, 1961; Kapadia et al. 1999). A common description of the RF is by a linear filter whose kernel is the difference of two independent Gaussian functions (DOG), which was originally introduced for the on-off/off-on type retinal ganglion cells (Rodieck and Stone 1965; Rodieck 1965). The DOG model is also wildly adopted as phenomenological descriptions for RFs of neurons in primary visual cortex (Sceniak et al., 1999, 2001; Chen et al., 2012). The computational model captures the physiological properties of excitatory and inhibitory neural response to visual stimulation and successfully predicts the response of retinal ganglion cells to motion (Rodieck 1965).

However, the linear DOG model fails to account multiple properties of center/surround RFs such as nonlinearity (Enroth-Cugell and Robson, 1966), contrast and context dependence (Sceniak et al., 1999; Worgotter and Eysel, 2000). The neural RF is also altered dynamically by statistics of natural stimuli (David et al., 2004, Talebi and Baker Jr, 2012).

To interpret various properties of neural RFs, phenomenological models with sophisticated designs are introduced (Hochstein and Shapley, 1976; Soodak, 1986; Victor JD 1987; Cauvanaugh et al., 2002). However, RF structure of a neuron is essentially determined by the interactive mechanisms of the intricate networks it connects to. Understanding the structure in terms of neurobiological components and the interactive dynamics is fundamental to neuroscience. Efforts have been made to unveil the circuitry mechanisms with different approaches (McMahon et al., 2004; Olshausen and Field, 1996; Anderson et al., 2001, Demb et al., 1999). So far, computational models have been focusing on the discussion of the spatial origins of RF structure (Schwabe et al., 2006; Somers et al., 1998) but the temporal dynamics of RFs are rarely talked.

Here, we study the center-surround RF structure in the context of a concrete neural network, where two population (excitatory and inhibitory) of spiking neurons form mutual connections with each other. Different from common local inhibitory feedback (Somers et al., 1998), the model includes a group of inhibitory neurons that project globally to the excitatory group. We show that the center-surround RF is generated in the recurrent feedback loop via the dynamical interaction between the two populations.

2.2 Methods

2.2.1 Recurrent neural network with global inhibitory feedback

We consider a recurrent network consisting of 2 linear arrays: the excitatory group and inhibitory group (Fig. 2.2a). Each group contains 300 neurons that are modeled as leaky-integrate-fire neuron with spike-rate adaptation. Below spiking threshold $V_{\theta,i}$, the membrane potential of ith neuron V_i evolves according to the differential equation $\tau_i dV_i / dt = E_i - V_i - R_i\left(I_{sra,i} + I_{s,i} - I_{e,i}\right)$. Whenever the membrane potential V_i reaches the threshold $V_{\theta,i}$, V_i is instantaneously reset to $V_{reset,i}$ and interpreted as a spike. The other cellular parameters are denoted as following: the reset potential $V_{reset,i}$, the resting membrane potential E_i, the membrane input resistance R_i, and the membrane time constant τ_i.

The firing-rate of the neurons is modulated by spike-rate adaptation current $I_{sra,i} = g_{sra,i}(t)(V_i - E_{sra,i})$. Each time a spike occurs, the spike-rate adaptation conductance $g_{sra,i}$ increases by an amount $\Delta g_{sra,i}$ i.e., $g_{sra,i}(t^+) \rightarrow g_{sra,i}(t^-) + \Delta g_{sra,i}$ and subsequently decays exponentially with adaptation time constant $\tau_{sra,i}$, i.e., $\tau_{sra,i} dg_{sra,i} / dt = -g_{sra,i}$ until the next spike occurs. The synaptic current $I_{s,i} = \sum_j g_{ij} P_{ij} w_{ij}(V_i - E_{ij})$ from neuron j to neuron i is proportional to the open probability P_{ij} of the synaptic conductance, which has the form of

$P_{ij}(t) = B_{ij} \sum_k \left(e^{-(t-t_j^k)/\tau_{1,ij}} - e^{-(t-t_j^k)/\tau_{2,ij}} \right)$. The normalization factor $B_{ij} = ((\tau_{2,ij} / \tau_{1,ij})^{\tau_{rise,ij}/\tau_{1,ij}} - (\tau_{2,ij} / \tau_{1,ij})^{\tau_{rise,ij}/\tau_{2,ij}})^{-1}$ ensures that the peak value of P_{ij} generated by a single spike to be 1. The synaptic rise time is given by $\tau_{rise,ij} = \tau_{1,ij}\tau_{2,ij} / (\tau_{1,ij} - \tau_{2,ij})$. The maximum synaptic conductance is denoted g_{ij}, E_{ij} is the synaptic reversal potential, and w_{ij} is the weight matrix. The time constants $\tau_{1,ij}$ (fall time) and $\tau_{2,ij}$ ($\tau_{1,ij} > \tau_{2,ij}$) determine the time course of synaptic current. The variable t_j^k represents the time at which neuron j generates the spike k. A summation is performed over all spikes generated by neuron j.

In order to make the network specific we choose the parameter values of excitatory, inhibitory neurons and synapses based on in vitro intracellular recordings in the avian isthmotectal system (Shao et al. 2009) unless stated otherwise. All conductance are expressed in terms of an average membrane conductance, $g_m = 2.78$ nS. For the basic cellular parameters the values are: $V_{\theta,E} = -39$ mV, $V_{\theta,I} = -40$ mV, $V_{reset,E} = -50$ mV, $V_{reset,I} = -60$ mV, $E_E = -55$ mV, $E_I = -64$ mV, $R_E = 480$ MΩ, $R_I = 240$ MΩ, $\tau_E = 104$ ms, $\tau_I = 50$ ms. The subscription E/I indicates the excitatory/inhibitory neuron group. For the spike-rate adaptation the parameter values are: $\tau_{sra,E} = 50$ ms, $\tau_{sra,I} = 80$ ms, $\Delta g_{sra,E} = 0.375 g_m$, $\Delta g_{sra,I} = 2.25 g_m$, and $E_{sra,E} = E_{sra,I} = -70$ mV. The synaptic time constants for the excitatory synapses are: $\tau_{1,IE} = 7.6$ ms, $\tau_{2,IE} = 0.47$ ms (Shao et al. 2009). The synaptic time constants for the inhibitory projections are $\tau_{1,EI} = 5.6$ ms and $\tau_{2,EI} = 0.3$ ms, which are commonly used for GABAergic synapse (Destexhe et al. 1994).

The synaptic reversal potentials $E_{IE} = 0.0$ mV, $E_{EI} = -80.0$ mV, are consistent with literature values for excitatory and inhibitory synapses (Koch 1999). The maximum synaptic conductances for the excitatory and inhibitory projections are held fixed, $g_{IE} = 1.5 g_m$ and $g_{EI} = 0.24 g_m$. All others are specified in the text.

We assume that the network includes topographic feedforward and global feedback connections, which are incorporated in the weight matrix w_{ij}. Gaussian distribution describes the feedforward projections. For instance, the topographic projection from excitatory neuron j to inhibitory neuron i follows $w_{ij} = e^{-(i-j)^2/(2\Delta_{IE}^2)}$, where Δ_{IE} describes the width of the distribution and $\Delta_{IE} = 16$. The global feedback projection is generated according to a homogeneous distribution $w_{ij} = 1$.

The external excitatory stimulus, are modeled as a series of α-function $I_0(t) = \frac{a_s t}{\tau_s} \exp(-t/\tau_s)$ of frequency f, where $a_s = 0.6$ and $\tau_s = 5.6$ ms. The stimulus is centered at neuron #c and of half width s, i.e., $2s+1$ neurons of the excitatory neuron centered at location c receive stimulus input formulated by $I_{e,i} = I_0(t) H(i-(c-s)) H(c+s-i)$. The Heaviside step function, H, expresses that the current to L10 neurons is non-zero between neuron $\#(c-s)$ and $\#(c+s)$ and zero elsewhere.

The output neuron is modeled using Hill's function of the form $ar^n/(r^n+b^n)$. Here r is the input firing rate from presynaptic neurons, a is the saturation firing rate, b is the input firing rate when the output reaches the half of its saturation value, and n describes the steepness of the response curve. These parameters are chose as $a=40$, $b=20$, $n=2$.

2.2.2 Difference of Gaussian

To compare our results with the DOG model, the simulated size-response curve is fitted by DOG function of the form $k_e\int_{-w}^{w} e^{-(2t/r_e)^2}\,dt - k_i\int_{-w}^{w} e^{-(2t/r_i)^2}\,dt$, where r_e and r_i are the size of the excitatory and inhibitory receptive field respectively. The relative strength of the two parts are indicated by the coefficients k_e and k_i.

2.3 Results

2.3.1 A recurrent neural network with local excitation and global inhibition

Widespread lateral connections in cortical and sub-cortical areas (Gilbert, 1992; Gilbert et al., 1996; Wang, 2004) are likely to substrate the integration of spatial information of the visual world. To understand the RF structure that could result from such network organizations, we consider a network with two arrays of neurons: one excitatory group and one inhibitory group. The excitatory neurons project topographically to the inhibitory neurons, whereas, the inhibitory neurons projects globally to every excitatory neuron (Fig. 2.1a). The stimuli are spots of increasing size and deliver Poisson spike trains/regular pulse trains to the excitatory neuron group. In analogy to the linear-filter

description, we introduce an output neuron that receives input from excitatory neurons around the stimulus center, which could be interpreted as the neuron's excitatory receptive field (eRF). The output neuron transfers the average firing-rate of its eRF through a sigmoid function. The parameters of the sigmoid function are chosen so that the output neuron faithfully represents the activity of its eRF without reaching the saturation branches of the sigmoid function.

2.3.2 A feedforward size-response profile mimics recurrent circuit responses

In the presence of regular spike train, the response curve of the output neuron follows the characteristic response profile of a center/surround RF: as the stimulus size increases the neuron response reaches a peak and then fall to a non-zero steady state. Specifically, for small size spots, parts of the output neuron's eRF are activated, which excite the corresponding inhibitory neurons as well. With increasing spot size, more excitatory neurons are activated and the response climbing to the peak accordingly. As the spot size reaches beyond the eRF of the output neuron, the excitatory neurons within eRF increasingly receive more lateral inhibitions. As a result, the response of the output neuron starts to decrease. Intuitively, further increase of the spot size would induce more inhibition and eventually terminate the activity of the output neuron. However, the neuron reaches a steady state of non-zero firing rate **(**Fig. 2.1b**).**

The non-zero asymptote of the response curve is a result of the dynamic interaction between the excitatory and inhibitory neurons. The inhibitory neurons are driven by the pre-synaptic excitatory neurons. Under the stimulation of periodic pulse train, the

inhibitory current always occurs within a short period after the spikes of the excitatory neurons. As the stimulus size increases, more inhibitory neurons are activated and the inhibitory conductance increases proportionally. With stimulus of small size, the membrane potential of the center excitatory neuron is far above the synaptic reversal potential ~ -80 mV. Therefore, the inhibition current is proportional to the synaptic conductance. With larger stimulus, the membrane potential is hyperpolarized close to the synaptic reversal potential. As a result, although the synaptic conductance increases, the inhibitory current saturates **(**Fig. 2.1c**)**, which is also known as shunting. Accordingly, the firing-rate of the neuron within the eRF decreases and finally reaches the steady state. On the other hand, the decreased firing rate of excitatory neuron leads to lower activities of the inhibitory neurons and therefore reduces inhibitory current, which further enhances the saturation of the inhibitory current.

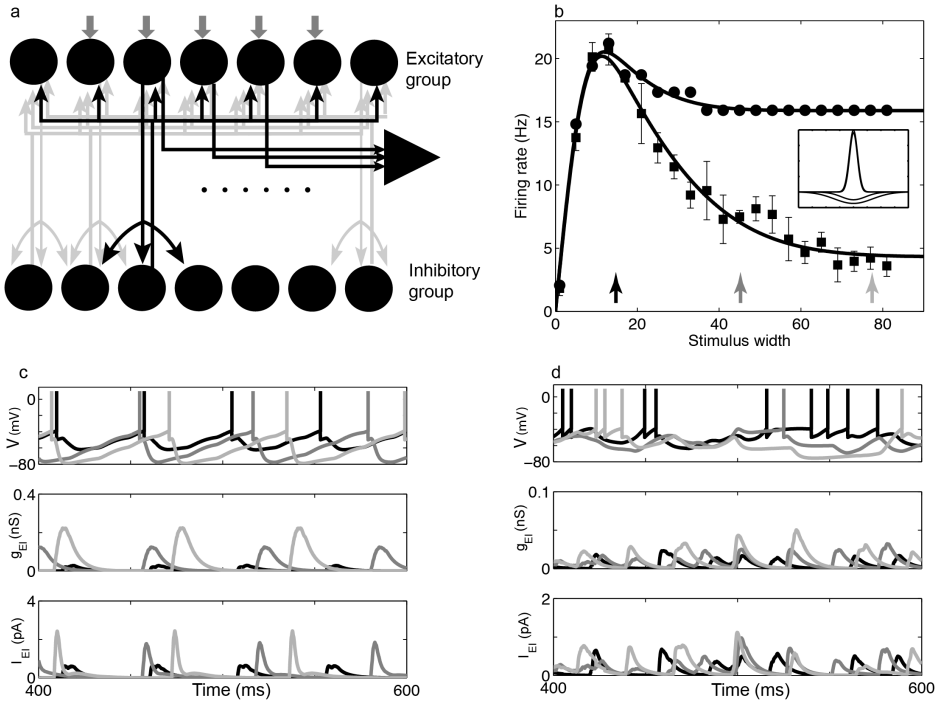

Figure 2.1 a) A recurrent neural network with excitation and inhibition. The feedforward projections are topographic excitation of Gaussian distribution. The feedbacks are global

inhibition of homogeneous distribution. Stimulus is modeled as pulse trains of alpha-function fed into the excitatory group. The output neuron transfers the average firing rate of the excitatory neurons around the stimulus center through a sigmoid function. b) The response curves to stimulus of periodic pulse train and Poisson pulse train (60Hz) are indicated by filled circle and square respectively. The simulated results are fitted to DOG model (solid line). The inset shows the excitatory and inhibitory components of the DOG model. The excitatory components of the two response curves are close while response curve to Poisson pulse train shows relatively larger inhibitory surrounding. c) From top to bottom shows the time course of membrane potential, synaptic conductance, and synaptic currents of the center excitatory neuron respectively. The stimuli are periodic pulse train. The gray level indicates width of the stimulus (also pointed out by arrows in b). d) From top to bottom shows the time course of membrane potential, synaptic conductance, and synaptic currents of the center excitatory neuron respectively. The stimuli are Poisson pulse train. The gray level indicates width of the stimulus (also pointed out by arrows in b).

2.3.3 The response curve is modulated by the spatio-temporal pattern of the stimulus

Neuron RFs are stimulus dependent (Kapadia et al. 1999; Solomon et al. 2002, Angelucci et al., 2002). To view how stimulus pattern would affect the RF structure in the model, we stimulate the network with spatially uncorrelated Poisson pulse train. As the stimulus size increases, the response curve reaches a peak then decreases, maintaining the characteristic shape. However, comparing to regular spike train, the response to the Poisson spike trains shows lower steady state firing-rate and suggests a larger surround inhibition (Fig. 2.1b). Driven by spatially uncorrelated Poisson spike trains, the excitatory neurons fire randomly and so do the inhibitory neurons. Considering the excitatory neuron at the center of the stimulus, its synaptic conductance changes every time an inhibitory neuron fires regardless of its location (due to the global inhibitory feedback). Therefore, although the spike timings vary greatly among individual inhibitory neurons, the synaptic conductance deflections of the excitatory neuron distribute evenly along the

time-axis (Fig. 2.1d). With increased stimulus size, the deflection happens more frequently and with higher amplitude. Since the spiking time is random now, the deflections do not necessarily occur during the hyperpolarizing phase of the excitatory neuron and the inhibitory current saturation only happens occasionally. Therefore, a larger inhibition effects is expressed after the current is integrated by the excitatory neuron.

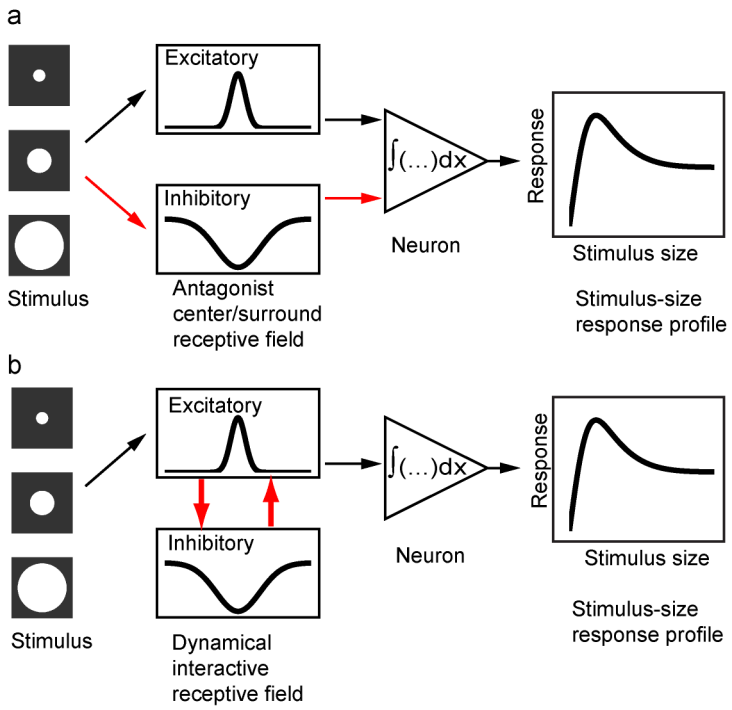

Figure 2.2 Comparison between linear-filter description and the recurrent network description. a) In a linear filter description, stimulus excites the excitatory and the inhibitory component of the RF. The output neuron sums up the two components. Since the inhibitory surround has a larger spatial extension than the excitatory center, the response curve reaches a peak and then decreases as the stimulus size increases. b) In the new recurrent network description, the stimulus only activates the excitatory neural group. The excitatory group and the inhibitory group interact though the feedback loop. The activity of the excitatory group is read out by the output neuron and the response curve shows the same characteristic shape as of in the filter description.

2.4 Discussion

Linear-filter has been used as a standard technique in describing neuron RF. This idea that roots in the difference-of-Gaussian (DOG) model (Rodieck, 1965; Einevoll and Plesser, 2004) has also been applied to cells of simple to complex RF structures (Rust et al., 2005). However, the assumption of non-interactive RF subunits behind the description is only for mathematic simplicity but not biologically based (Fig. 2.2a). We use a completely different approach and build a model that is based on concrete neural circuitry. We construct a network consisting of topographic excitation and global inhibition (Fig. 2.2b). Topographic excitation is common in the visual pathway and wide-field inhibition is also an anatomical structure shared among visual systems having center/surround RF (Rockland et al. 1982; Rockland and Lund 1983; Mysore, 2010). The model reproduced the characteristic response of a center/surround RF. Moreover, in the network model, stimulus-dependent RF structure comes naturally as an inherited property of dynamic interaction between excitatory and inhibitory subunits.

2.5 Reference

Angelucci A, Levitt JB, Walton EJS, Hupe JM, Bullier J, Lund JS (2002) J Neurosci 22: 8633-8646

Anderson JS, Lampl I, Gillespie DC, Ferster D (2001) Membrane potential and conductance changes underlying length tuning of cells in cat primary visual cortex. J Neurosci 21:2104-2112.

Brown SP, He S, Masland RH (2000) Receptive field microstructure and dendritic geometry of retinal ganglion cells, Neuron 27: 371-383

Cavanaugh JR, Bair W, Movshon JA (2002) Nature and interaction of signals from the receptive field center and surround in macaque V1 neurons. J Neurophysiol. 88: 2530-2546

Chen K, Song XM, Li CY (2012) Contrast-dependent variations in the excitatory classical receptive field and suppressive nonclassical receptive field of cat primary visual coretex, Cerebral Cortex, doi:10.1093

Demb JB, Haarsma L, Freed MA, Sterling P (1999) Functional circuitry of the retinal ganglion cell's nonlinear receptive field. J Neurosci. 19: 9756-9767

David SV, Vinje WE, Gallant JL (2004) Natural stimulus statistics alter the receptive field structure of V1 neurons, J Neurosci. 24:6991-7006

Enroth-Cugell Ch, Robson JG (1966) The contrast sensitivity of retinal ganglion cells of the cat J. Physiol. 187: 517-552

Einevoll GT and Plesser HE (2005), Response of the difference-of-Gaussians model to circular drifting-grating patches, Visual Neuroscience, 22: 437-446

Gilbert CD (1992), Horizontal integration and cortical dynamics, Neuron 9: 1-13.

Gilbert CD, Das A, Ito M, Kapadia M, Wetheimer G (1996), Spatial integration and cortical dynamics, Proc. Natl. Acad. Sci. 93: 615-622

Hubel DH, Wiesel TN (1961), Integrative action in the cat's lateral geniculate body, J. Physiol. 155: 385-398.

Hubel DH, Wiesel TN (1959), Receptive fields of single neurons in the cat's striate cortex, J. Physiol. 148: 574-591.

Hochstein S, Shapley RM (1976). Linear and nonlinear spatial subunits in Y cat retinal ganglion cells J. Physiol. 262: 237-264.

Kuffler SW (1953), Dsicharge patterns and functional organization of mammalian retina, J. Neurophysiol. 16: 37-68.

Kapadia M, Westheimer G, Gilbert CD (1999), Dynamics of spatial summation in primary visual cortex of alert monkeys, Proc. Natl. Acad. Sci, 96:12073-12078

McMahon MJ, Packer OS, Dacey DM (2004) The classical receptive field surround of primate parasol ganglion cells is mediated primarily by a non-GABAergic pathway. J Neurosci. 24: 3736-3745.

Olshausen BA and Field DJ (1996) Emergence of simple-cell receptive field properties by learning a sparse code for natural images. Letters to Nature, 381:607-609.

Soodak R (1986) Two-dimensional modeling of visual receptive fields using Gaussian subunits. 83: 9259-9263.

Rodieck RW, Stone J (1964) Analysis of receptive fields of cat retinal ganglion cells. J Neurophysiol. 28: 833-849.

Rodieck, RW (1965). Quantitative analysis of cat retinal ganglion cell response to visual stimuli Vision Res: 583-601

Rockland KS, Lund JS (1983) Intrinsic laminar lattice connections in primate visual cortex. J. Comparative Neurol. 216: 303-318

Rockland KS, Lund JS, Humphrey AL (1982) Anatomical banding of intrinsic connections in striate cortex of tree shrews. J. Comparative Neurol. 209 41-58

Somers DC, Todorov EV, Siapas AG, Toth LJ, Kim DS, Sur M (1998) A local circuit approach to understanding integration of long-range inputs in primary visual cortex. 8:204-217

Solomon SG, White AJR, Martin PR (2002) Extraclassical receptive field properties of parvocellular, magnocellular, and koniiocellular cells in the primate lateral geniculate nucleus, Journal of Neuroscience, 22: 338-349

Schwabe L, Obermayer K, Angelucci A, Bressloff PC (2006) The role of feedback in shaping the extra-classical receptive field of cortical neurons: a recurrent network model, J Neurosci. 26: 9117-9129.

Sceniak MP, Ringach DL, Hawken MJ, Shapley R (1999) Contrast's effect on spatial summation by macaque V1 neurons, Nat Neurosci 2: 733-739

Sceniak MP, Hawken MJ, Shapley R (2001) Visual spatial characterization of macaque V1 neurons, J Neurophysiol 85: 1873-1887.

Talebi V and Baker Jr C (2012) Natural versus synthetic stimuli for estimating receptive field models: a comparison of predictive robustness.32: 1560-1576.

Victor JD (1987) The dynamics of the cat retinal X cell centre. J Physiol. 386: 219-246

Worgotter F, Eysel UT (2000) Context, state and the receptive fields of striatal cortex cells, Trends Neurosci. 23: 497-503.

Wang Y, Major DE & Karten, HJ (2004) Morphology and connections of nucleus isthmi pars magnocellularis in chicks. J. Comparative Neurol. 469: 275-297

3 Generating oscillatory bursts from a network of regular spiking neurons without inhibition

Avian nucleus isthmi pars parvocellularis (Ipc) neurons are reciprocally connected with the tectal layer 10 (L10) neurons and respond with oscillatory bursts to visual stimulation. Our *in vitro* experiments show that both neuron types respond with regular spiking to somatic current injection and that the feedforward and feedback synaptic connections are excitatory, but of different strength and time course. To elucidate mechanisms of oscillatory bursting in this network of regularly spiking neurons, we investigated an experimentally constrained model of coupled leaky integrate-and-fire neurons with spike-rate adaptation. The model reproduces the observed Ipc oscillatory bursting in response to simulated visual stimulation. A scan through the model parameter volume reveals that Ipc oscillatory burst generation can be caused by strong and brief feedforward synaptic conductance changes. The mechanism is sensitive to the parameter values of spike-rate adaptation.

3.1 Introduction

Oscillatory bursts play an important role in stimulus encoding (Gabbiani et al. 1996; Lesica, Stanley 2004; Oswald et al. 2004; Reinagel et al. 1999) and in the communication between neurons (Izhikevich et al. 2003; Lisman 1997; Sherman 2001). Mechanisms of oscillatory burst generation (Coombes and Bressloff 2005) range from the interaction of fast and slow currents in single neurons (Izhikevich 2007; Krahe and Gabbiani 2004;

Rinzel and Ermentrout 1998; Wang and Rinzel 2003) to the interaction of neurons in networks typically consisting of excitatory and inhibitory connections (Buzsaki 2006; Traub et al. 2004). Here, we investigate oscillatory burst generation in a recurrently connected network of spiking neurons with excitatory synapses, where activity-dependent adaptation replaces the stabilizing role of inhibition.

The avian isthmo-tectal system (Fig. 3.1) plays a key role in visual information processing (Cook 2001; Maczko et al. 2006; Marin et al. 2007; Wang 2003). It consists of three key anatomical elements. A subpopulation of tectal layer 10 (L10) neurons receive retinal inputs and project to the ipsilateral nucleus isthmi pars parvocellularis (Ipc) and the nucleus isthmi pars magnocellularis (Imc) in a topographic fashion (Wang et al. 2004, 2006). The cholinergic Ipc neurons form topographic reciprocal connections with the tectum, where their axons terminate in a columnar manner ranging from layer 2 to 12 (Wang et al. 2006). The GABAergic Imc neurons consist of two cell types. One type projects broadly to the Ipc, whereas the other type projects upon tectal layers 10 to 13 (Wang et al. 2004).

Ipc neurons respond with fast oscillatory bursts to flashing or moving visual stimulations (Fig. 3.1(a); Marin et al. 2005). Because of the extensive arborisation of Ipc axons in upper tectal layers (Wang et al. 2006), the Ipc oscillatory bursts (Marin et al. 2005) are also detected in extracellular recordings from superficial and intermediate tectal layers (Knudsen 1982; Neuenschwander and Varela 1993; Neuenschwander et al. 1996). Thus, as pointed out by Marin and co-workers, oscillatory burst recordings in the tectum may

falsely be interpreted as oscillatory bursts originating in the tectum (Marin et al. 2005). The oscillatory bursts in tectal recordings disappear after injecting micro-drops of lidocaine into the corresponding area of the Ipc nucleus (Marin et al. 2005), thus confirming the role of the Ipc neurons in the oscillatory burst generation. The Ipc nucleus receives two inputs (Fig. 3.1(b), (c)). It receives glutamatergic (Hellmann et al. 2001; Marin et al. 2007) and possibly cholinergic (Britto et al. 1992; Wang et al. 2006) inputs from a subpopulation of tectal L10 neurons, characterized by unusual "shepherd's crook" axons that arise from the apical dendrite and then make a U-turn to leave the tectum through deeper layers (Wang et al. 2006). It receives GABAergic input from the adjacent Imc nucleus (Wang et al. 2004). Importantly, the Ipc oscillatory burst responses persist when the Imc nucleus is inactivated via local application of CNQX (see Fig. 6D in Marin et al. 2007). Further, the retinal inputs to L10 neuron dendrites in upper tectal layers (Fig. 3.1(c)) show no evidence of bursting; rather in vivo recordings seem to suggest that spots of light produce continuous and long-lasting evoked potentials in superficial tectal layers (Holden 1980; Letelier et al. 2000). These observations narrow down the possible mechanisms for the observed Ipc oscillatory burst generation to the reciprocally connected L10 and Ipc neurons. For instance, the delays in the reciprocal connection (Meyer et al. 2008) could imply the involvement of delayed feedback in the induction of oscillatory dynamics (Brandt et al. 2006; Brandt and Wessel 2007; Brandt et al. 2007; Chacron et al. 2005; Doiron et al. 2003; Laing and Longtin 2003; Milton 1996).

To investigate the mechanisms of the observed oscillatory bursting in Ipc, we conducted whole-cell recordings from L10 and Ipc neurons combined with synaptic stimulations in

chick brain slice preparations (Fig. 3.1(b)). Based on the in vitro experimental results, we built a model network consisting of reciprocally connected leaky integrate-and-fire neurons, representing L10 and Ipc neurons, and tested under what conditions this experimentally constrained model network reproduces the observed bursting activity in Ipc.

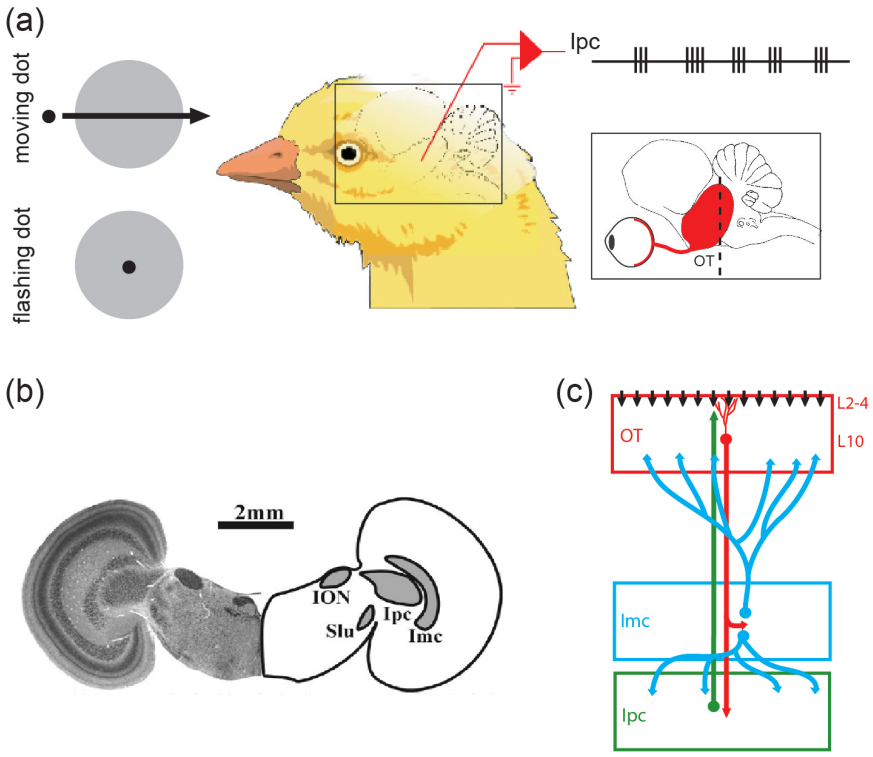

Figure 3.1 Schematic drawings of *in vivo* and *in vitro* recording set-ups. (**a**) Recordings *in vivo* showed that nucleus isthmi pars parvocellularis (Ipc) neurons responded to moving dots and flashing dots with oscillatory bursts (Marin et al. 2005). The rectangle inset shows a schematic lateral view of the chick brain with the retina, optic nerve, and optic tectum (OT) in red. The dashed line indicates the approximate location of the transverse slicing. (**b**) A transverse slice of the chick midbrain both in histological image and corresponding outlines (scale bar = 2 mm). The nucleus isthmo-opticus (ION) and the nucleus semilunaris (SLu) are not considered in this study. The patch-electrode schematic indicates a typical recording location from an Ipc neuron. The dashed rectangle indicates the location of the schematic circuitry described in (c). (**c**) Schematic drawings of the isthmo-tectal circuitry consisting of the retinal ganglion cells axons (vertical black arrows), the tectal layer 10 (L10) neurons (red), the Ipc neurons (green), and the nucleus isthmi pars magnocellularis (Imc) neurons (blue).

3.2 Methods

3.2.1 Experiments

White Leghorn chick hatchlings (Gallus gallus) of less than 3 days of age were used in this study. All procedures used in this study were approved by the local authorities and conform to the guidelines of the National Institutes of Health on the Care and Use of Laboratory Animals. Animals were injected with ketamine (40 mg per kg, i.m.). Brain slices of the midbrain were prepared following published protocols (Dye and Karten 1996; Luksch et al. 2001). Briefly, preparations were done in 0°C, oxygenated, and sucrose-substituted saline (240 mM sucrose, 3 mM KCl, 5 mM $MgCl_2$, 0.5 mM $CaCl_2$, 1.2 mM NaH_2PO_4, 23 mM $NaHCO_3$, and 11 mM D-glucose). After decapitation, the brains were removed from the skull, and the forebrain, cerebellum, and medulla oblongata were discarded. A midsagittal cut was used to separate the tectal hemispheres. The tectal hemispheres were sectioned at 500 μm on a tissue slicer (Vibroslice, Campden or VF-200, Precisionary Instruments) in either the transverse or the horizontal plane. Slices were collected in oxygenated saline (120 mM NaCl, 3 mM KCl, 1 mM $MgCl_2$, 2 mM $CaCl_2$, 1.2 mM NaH_2PO_4, 23 mM $NaHCO_3$, and 11 mM D-glucose) and kept submerged in a chamber that was bubbled continuously with carbogen (95% oxygen, 5% CO_2) at room temperature. The slice was then transferred to a recording chamber (RC-26G, Warner Instruments) mounted on a fixed-stage upright microscope equipped with differential interference contrast optics (BX-51WI, Olympus). The slice was held gently to the bottom of the chamber with an anchor of nylon threads, and the chamber was perfused continuously with oxygenated saline at room temperature. The potential effects

of temperature or age on measured cellular and synaptic properties were not addressed in this study. The L10 and Ipc neurons are visible with DIC optics.

Local electrical stimulation was achieved by inserting bipolar tungsten electrodes under visual control into either the tectal layers 10/11, or the Ipc nuclei with a three-axis micromanipulator (U-31CF, Narishige). Electrodes were custom-built from 50-µm diameter, insulated tungsten wires (California Fine Wire) that were glued together with cyanoacrylate and mounted in glass micro capillaries for stabilization. The wires protruded several hundred µm from the capillaries, and the tips were cut at an angle. Stimulus isolators (Isolated Pulse Stimulator 2100, AM Systems) generated biphasic current pulses (20 – 200 µA, 500 µs).

Whole-cell recordings were obtained with glass micropipettes pulled from borosilicate glass (1.5 mm OD, 0.86 mm ID, AM Systems) on a horizontal puller (P-97, Sutter Instruments or DMZ Universal Puller, Zeitz Instruments) and were filled with a solution containing 100 mM K-Gluconate, 40 mM KCl, 10 mM HEPES, 0,1 mM $CaCl_2$, 2 mM $MgCl_2$, 1.1 mM EGTA, 2 mM Mg-ATP, pH adjusted to 7.2 with KOH. Electrodes were advanced through the tissue under visual guidance with a motorized micromanipulator (MP-285, Sutter Instruments) while constant positive pressure was applied and the electrode resistance was monitored by brief current pulses. Once the electrode had attached to a membrane and formed a seal, access to the cytosol was achieved by brief suction. Whole-cell recordings were performed with the amplifier (Axoclamp 2B, Axon Instruments or SEC-05L, npi-electronic) in the bridge mode (current clamp). The series

resistance was estimated by toggling between the bridge and the DCC (discontinuous current clamp) mode, and subsequently compensated with the bridge balance. Depolarizing and hyperpolarizing currents were injected through intracellular electrodes. Analog data were low-pass filtered (4-pole Butterworth) at 1 kHz, digitized at 5 kHz, stored, and analyzed on a PC equipped with a PCI-MIO-16E-4 and LabView software (both National Instruments).

Labeling of a subset of recorded neurons was carried out as described previously (Luksch et al. 1998; Mahani et al. 2006). In brief, whole-cell patch recordings were obtained as described above. Additionally, the electrode solution contained 0.5% Biocytin (w/v) to label the recorded neurons. Individual cells were filled intracellularly with 2 nA of positive current injection over 3 minutes through the patch electrode. After recording and labeling, slices were kept in oxygenated ACSF for an additional 30 minutes and subsequently fixed by immersion in 4% paraformaldehyde in PB for at least 4 hours. Slices were then washed in phosphate buffer (PB, 0.1 M, pH 7.4) for at least 4 hours, immersed in 15% sucrose in PB for at least 4 hours and then immersed in 30% sucrose in PB for 12 hours, and resectioned at 60 µm on a freezing microtome. The sections were collected in PB and the endogenous peroxidase blocked by a 15-minute immersion in 0.6% hydrogen peroxide in methanol. The tissue was washed several times in PB, and then incubated in the avidin-biotin complex solution (ABC Elite kit, Vector Labs) and the reaction product visualized with a heavy-metal intensified DAB protocol. Following several washes in PB, the 60 µm-thick sections were mounted on gelatin-coated slides, dried, dehydrated, and coverslipped. Sections were inspected for labeled neurons, and

only data from cells that could unequivocally be classified according to published criteria (Wang et al. 2004, 2006) were taken for further analysis. Cells were reconstructed at medium magnification (10x or 20x) with a camera lucida on a Leica microscope and projected onto the 2D plane.

3.2.2 Two-neuron model

We investigated the network dynamics of two reciprocally connected model neurons, representing the L10 and the Ipc neuron in the avian isthmotectal system. Each model neuron is of the leaky integrate-and-fire type with spike-rate adaptation. The dynamic of the membrane potentials V_{L10} and V_{Ipc} are determined by two coupled differential equations:

$$\tau_{m,L10}\frac{dV_{L10}}{dt} = E_{r,L10} - V_{L10} - R_{m,L10}(I_{sra,L10} + I_{Ipc\to L10} - I_{e,L10}) \quad (1)$$

$$\tau_{m,Ipc}\frac{dV_{Ipc}}{dt} = E_{r,Ipc} - V_{Ipc} - R_{m,Ipc}(I_{sra,Ipc} + I_{L10\to Ipc}) \quad (2)$$

where $E_{r,L10}$ denotes the resting membrane potential of the L10 neuron, $R_{m,L10}$ is the membrane input resistance, and $\tau_{m,L10}$ is the membrane time constant. The measured membrane time constants (Table 3.1) are larger than the measured axonal delays (Meyer et al. 2008). Thus delays in synaptic voltage responses of leaky integrate-and-fire model neurons are dominated by the membrane time constants. Therefore, we did not explicitly include axonal delays in the network model. When the membrane potential V_{L10} reaches the threshold $V_{\theta,L10}$ it is reset to $V_{reset,L10}$ instantaneously. This is interpreted as the

occurrence of a spike. The external current input $I_{e,L10}$ to the L10 neuron represents the stimulus from the retinal ganglion cell. The spike-rate adaptation current,

$$I_{sra,L10} = g_{sra,L10}(t)(V_{L10} - E_{sra,L10}) \tag{3}$$

has the adaptation reversal potential $E_{sra,L10}$, and the time varying adaptation conductance $g_{sra,L10}(t)$, which evolves according to the differential equation

$$\tau_{sra,L10} \frac{dg_{sra,L10}}{dt} = -g_{sra,L10} \tag{4}$$

Whenever the neuron fires a spike, the adaptation conductance changes according to

$$g_{sra,L10}(t^+) \rightarrow g_{sra,L10}(t^-) + \Delta g_{sra,L10} \tag{5}$$

The synaptic current

$$I_{Ipc\rightarrow L10} = g_{Ipc\rightarrow L10} P_{Ipc\rightarrow L10}(t)(V_{L10} - E_{Ipc\rightarrow L10}) \tag{6}$$

from the Ipc neuron to the L10 neuron projection is proportional to the open probability $P_{Ipc\rightarrow L10}(t)$ of the synaptic conductance, where $g_{Ipc\rightarrow L10}$ is the maximum synaptic conductance and $E_{Ipc\rightarrow L10}$ is the synaptic reversal potential. The open probability $P_{Ipc\rightarrow L10}(t)$ of the synaptic conductance from the Ipc to the L10 neuron has the form

$$P_{Ipc\rightarrow L10}(t) = B_{Ipc\rightarrow L10} \sum_k \left(\exp(-\frac{t - t_{Ipc}^k}{\tau_{1,Ipc\rightarrow L10}}) - \exp(-\frac{t - t_{Ipc}^k}{\tau_{2,Ipc\rightarrow L10}}) \right) \tag{7}$$

where the normalization factor

$$B_{Ipc\rightarrow L10} = \left(\left(\frac{\tau_{2,Ipc\rightarrow L10}}{\tau_{1,Ipc\rightarrow L10}} \right)^{\tau_{rise,Ipc\rightarrow L10}/\tau_{1,Ipc\rightarrow L10}} - \left(\frac{\tau_{2,Ipc\rightarrow L10}}{\tau_{1,Ipc\rightarrow L10}} \right)^{\tau_{rise,Ipc\rightarrow L10}/\tau_{2,Ipc\rightarrow L10}} \right)^{-1} \tag{8}$$

ensures that the peak value of $P_{Ipc\rightarrow L10}(t)$ generated by a single spike equals to 1, the variable t_{Ipc}^{k} represents the time at which the Ipc neuron generates the *kth* spike, and a summation is performed over all spikes generated by the Ipc neuron. The time constant $\tau_{1,Ipc\rightarrow L10}$ and $\tau_{2,Ipc\rightarrow L10}$ $(\tau_{1,Ipc\rightarrow L10} > \tau_{2,Ipc\rightarrow L10})$ determine the time course of the synaptic conductance change. The synaptic rise time is $\tau_{rise,Ipc\rightarrow L10} = \frac{\tau_{1,Ipc\rightarrow L10}\tau_{2,Ipc\rightarrow L10}}{\tau_{1,IpcL10} - \tau_{2,Ipc\rightarrow L10}}$, while $\tau_{1,Ipc\rightarrow L10}$ represents the fall time. The variables and parameters of the Ipc model neuron in Eq. (2) are all analogous to those of the L10 model neuron. The Ipc model neuron does not receive an external current input.

The Ipc steady-state response (taken to start 100 ms after stimulus onset) is represented by the "burst score" (Fig. 3.5). A spike preceded by an inter-spike-interval (ISI) of more than 10 ms and followed by an ISI of less than 4 ms is classified as the beginning of a burst. Subsequent spikes with ISIs of less than 4 ms are part of the burst. All other spikes are classified as isolated (Sillito and Jones 2002). The burst score is defined by the number of bursts divided by the sum of the number of bursts and the number of isolated spikes in the steady-state response. The score equals 1 when all spikes belong to bursts and equals 0 when all spikes are isolated. When the firing rate exceeds 1000 Hz the Ipc response is classified as diverging.

3.2.3 Population model with uncorrelated noise

For the population model of L10 and Ipc neurons (Fig. 3.6a) each individual neuron is of the leaky integrate-and-fire type with spike-rate adaptation as described above. Each population consists of 400 neurons. When referring to an individual neuron, we use the subscript i for L10 neurons and the subscript j for Ipc neurons. The dynamics of the membrane potentials V_i (L10 neuron i) and V_j (Ipc neuron j) are determined by the coupled differential equations:

$$\tau_{m,L10}\frac{dV_i}{dt} = E_{r,L10} - V_i - R_{m,L10}(I_{sra,i} + I_{Ipc\to i} - I_{e,i} + \chi_i) \tag{9}$$

$$\tau_{m,Ipc}\frac{dV_j}{dt} = E_{r,Ipc} - V_j - R_{m,Ipc}(I_{sra,j} + I_{L10\to j} + \chi_j) \tag{10}$$

The synaptic currents, $I_{L10\to j}$ and $I_{Ipc\to i}$, are similar in form to the one described above, Eq. (7), but now include contributions from a population of presynaptic neurons. For instance, the synaptic current in Ipc neuron j

$$I_{L10\to j} = \sum_i g_{L10\to Ipc} P_{ji}(t) W_{ji}(V_j - E_{L10\to Ipc}) \tag{11}$$

includes contributions from all L10 synaptic inputs to Ipc neuron j. The synaptic conductance is the product of the maximum synaptic conductance, $g_{L10\to Ipc}$, and the weight distribution

$$W_{ji} = \exp\left(-\frac{(i-j)^2}{2\Delta^2_{L10\to Ipc}}\right) \tag{12}$$

of width $\Delta_{L10\to Ipc}$. The latter reflects the narrow topographic projection from L10 to Ipc (Wang et al. 2006). The open probability of the synaptic conductance from L10 neuron i to Ipc neuron j has the form

$$P_{ji}(t) = B_{L10\to Ipc} \sum_k \left(\exp(-\frac{t - t_i^k}{\tau_{1,L10\to Ipc}}) - \exp(-\frac{t - t_i^k}{\tau_{2,L10\to Ipc}}) \right) \qquad (13)$$

The time constants and the normalization factor are the same as described above. The variable t_i^k represents the time at which the L10 neuron i generates the *kth* spike. The total synaptic current received by Ipc neuron j is therefore a sum of all the synaptic currents from the population of L10 neurons. The expression for the synaptic current $I_{Ipc\to i}$ received by L10 neuron i has a similar form.

The external current input, $I_{e,i} = (I_0 + \eta_{e,i})H(i-160)H(240-i)$, to L10 neuron i represents the stimulus from the retinal ganglion cell. This external current input has a constant component I_0 and a noise component $\eta_{e,i}$. The Heaviside step function, H, expresses that the current is non-zero to the L10 neurons numbered between 160 and 240 and zero elsewhere. The noise component, $\eta_{e,i}$, is modeled as uncorrelated white noise of standard deviation σ_e, i.e., $\langle \eta_{e,i}(t)\eta_{e,i'}(t') \rangle = 2\sigma_e^2 \delta(t-t')\delta_{ii'}$.

To allow for spontaneous activity, each L10 and Ipc neuron receives an uncorrelated noise current, χ_i and χ_j, respectively. The noise currents are modeled as uncorrelated white noise, i.e. $\langle \chi_i(t)\chi_{i'}(t') \rangle = 2\sigma_{L10}^2 \delta(t-t')\delta_{ii'}$ and $\langle \chi_j(t)\chi_{j'}(t') \rangle = 2\sigma_{Ipc}^2 \delta(t-t')\delta_{jj'}$ of standard deviation σ_{L10} and σ_{Ipc}, respectively.

In one set of simulations, we implemented an after-depolarization to the Ipc leaky integrate-and-fire model neurons using a phenomenological description (Doiron et al.

2007). When an Ipc spike occurs, an after-depolarizing current $I_{ADP} = Ax(t)$ is evoked after a time delay τ_{ADP}. Here $x(t)$ evolves according to the set of two differential equations $\frac{dx}{dt} = y$ and $\frac{dy}{dt} = -\alpha^2 x - 2\alpha y + \alpha^2 \sum_i \delta(t - t_i - \tau_{ADP})$, where t_i is the time at which the Ipc neuron spikes, α is the inverse of the time constant of the depolarization current and A is the current amplitude. The ADP current parameters ($A = 0.7$ nA, $\tau_{ADP} = 0.5$ ms, $\alpha = 4.5$ s^{-1}) were chosen for the simulated after-depolarization to match a large recorded after-depolarization.

The source code for the model is accessible at http://physics.wustl.edu/dlai/#Codes.

3.3 Results

3.3.1 Cellular and synaptic properties of L10 and Ipc neurons

A total of 12 neurons located in tectal layer 10 were recorded and were sufficiently labeled for unequivocal identification as shepherd's crook neurons. The Ipc nucleus receives glutamatergic inputs from a subpopulation of L10 neurons with the characteristic shepherd's crook axon (Wang et al. 2006). This type of neuron consists of an apical dendrite, several basal dendrites, and an axon originating from the apical dendrite with a characteristic U-turn before it courses towards the deep tectal layers (Fig. 3.2(a)). The average resting membrane potential was –59 ± 8 (mean ± SD, n = 12) mV, the average input resistance was 349 ± 198 MΩ, and the average membrane time constant was 105 ± 77 ms. We analyzed the cellular properties of the L10 neurons with depolarizing somatic

current injections from 0.01 to 0.2 nA. The recorded L10 neurons responded with a regular series of action potentials (Fig. 3.2(b)). The average firing rates, determined from the total number of spikes divided by the duration of the current pulse, increased approximately linearly with current amplitude (Fig. 3.2(c)). The average instantaneous onset firing rates, determined from the inverse of the first interspike intervals in response to the onset of the current pulse, were larger than the average firing rates (Fig. 3.2(c)), thus indicating some level of spike-rate adaptation.

A total of 45 cells were recorded in the Ipc nucleus and 27 of them were labeled sufficiently to allow for the attribution to the Ipc nucleus. The filled Ipc neurons were round or oval in shape and had a bipolar dendritic structure (Fig. 3.2(d)). The efferents from Ipc neurons terminate in the optic tectum in "paintbrush" terminal fields in a columnar manner (Wang et al. 2006). The average resting membrane potential was –61 ± 7 mV, the input resistance was 114 ± 37 MΩ, and the average membrane time constant was 35 ± 15 ms. The recorded Ipc neurons responded with a regular sequence of spikes to depolarizing current injections in the range from 0.1 to 1.0 nA injected into the soma (Fig. 3.2(e)). The average firing rates increased approximately linearly with current amplitude (Fig. 3.2(f)). For current amplitudes above ~0.5 nA, the average instantaneous onset firing rates were larger than the average firing rates (Fig. 3.2(f)), thus indicating some level of spike-rate adaptation. For completeness, we tested the possibility of intrinsic bursting from hyperpolarized levels, such as the T current-mediated bursting in thalamic relay neurons (McCormick and Huguenard 1992; Sherman 2001; Wang 1994;

Zhan et al. 1999). We observed regular spiking in response to depolarizing current steps from hyperpolarized levels of -90 mV in Ipc neurons (data not shown).

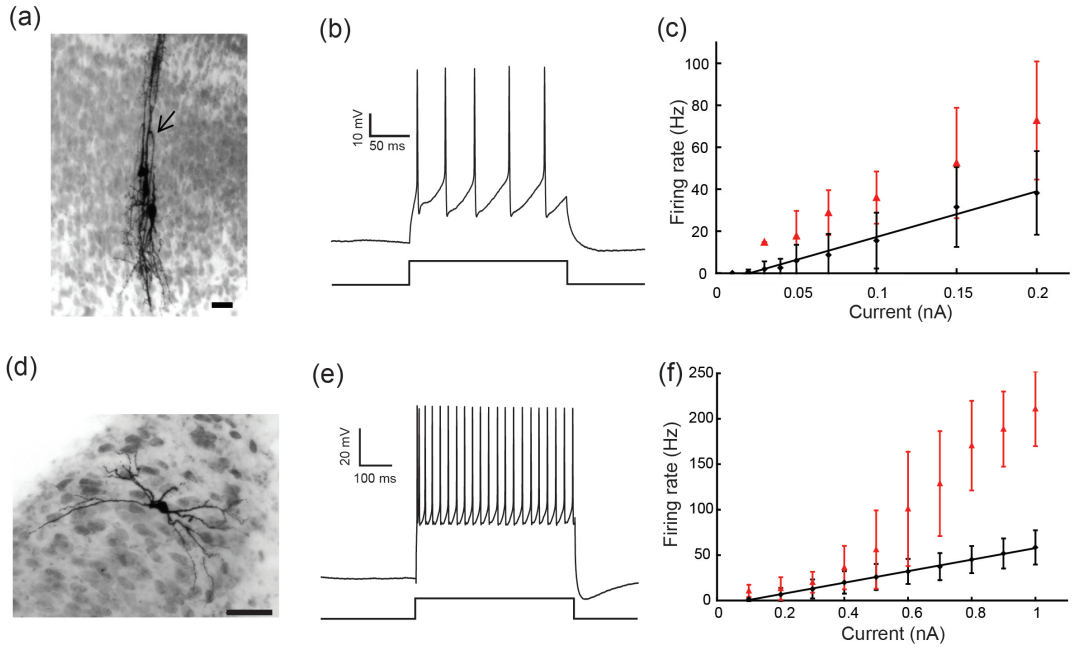

Figure 3.2 Morphological and electrophysiological properties of L10 and Ipc neurons. (**a**) Intracellular biocytin fills of three tectal L10 neurons. The U-shaped axon (arrow head) characterizes the center neuron as a shepherd's crook neuron, which projects to the nucleus isthmi. A U-shaped axon is also visible for the left neuron. Scale bar = 20 µm. (**b**) Response of a representative L10 neuron to a 0.1 nA current step. (**c**) Average firing rate (black diamonds) and instantaneous firing rate (the inverse of the first interspike intervals, red triangles) vs. current for the population of recorded L10 neurons. The black line represents a linear fit ($F(I) = 217.86 \times I - 4.61$; $r^2 = 0.9821$) of the firing rate, F, as a function of the injected current, I, to the measured average firing rate data points. (**d**) Intracellular biocytin fill in an Ipc neuron (scale bar = 50 µm). (**e**) Response of a representative Ipc neuron to a 0.5 nA current step. (**f**) Average firing rate (black diamonds) and instantaneous firing rate (the inverse of the first interspike intervals, red triangles) vs. current for the population of recorded Ipc neurons. The black line represents a linear fit ($F(I) = 63.427 \times I - 5.73$; $r^2 = 0.9988$) of the firing rate as a function of the injected current to the measured average firing rate data points.

Neuron	τ_m*(ms)*	R_m(MΩ)	E_r*(mV)*	V_θ*(mV)*	V_{reset}*(mV)*	τ_{sra}*(ms)*	Δg_{sra}*(nS)*	E_{sra}*(mV)*
L10	104	480	−55	−39	−50	50	1.25	−70
Ipc	25	135	−61	−40	−50	60	8.15	−70

Table 3.1 Single neuron parameters. Abbreviations: τ_m = membrane time constant, R_m = membrane input resistance, E_r = resting membrane potential, V_θ = threshold for spiking, V_{reset} = reset voltage, τ_{sra} = spike-rate adaptation time constant, Δg_{sra} = spike-rate adaptation conductance increment, E_{sra} = spike-rate adaptation reversal potential.

To measure the amplitude and time courses of the reciprocal synaptic connections between L10 and Ipc neurons, we positioned an extracellular stimulus electrode in either structure and recorded the response to local extracellular electrical stimulation in the other one. Recorded Ipc neurons responded to the stimulation in tectal layer 10 with fast and strong EPSPs that could generate one to three action potentials for sufficiently strong stimulation (Fig. 3.3(a)). The synapse showed little depression (Fig. 3.3(a) inset). From seven recorded L10 → Ipc connections we estimated the values for the synaptic time constants, $\tau_{1,L10\to Ipc} = 7.2 \pm 4.7$ ms and $\tau_{2,L10\to Ipc} = 0.47 \pm 0.16$ ms, by matching the time course of model neuron synaptic responses (Sec. 2.2) to the recorded subthreshold EPSPs. The feedback connection was qualitatively different. Recorded L10 neurons responded to brief electrical stimulation within the Ipc nucleus with small and long lasting EPSPs (Fig. 3.3(b)). The large L10 membrane time constant of approximately 100 ms precludes a reliable estimation of the synaptic time constant for the Ipc → L10 connection from the voltage response. Therefore, we limited the quantification of the synaptic responses to the time course of the EPSPs. The recorded EPSPs dropped to 37 % of their peak value after 87 ± 8 ms (n = 3 cells). These observations indicate that in the avian isthmo-tectal system the synaptic conductance change is strong and brief in the

feedforward direction, L10 → Ipc, and weak and long-lasting in the feedback direction, Ipc → L10.

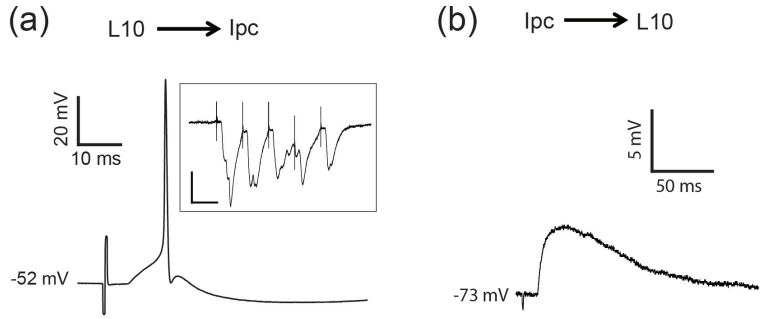

Figure 3.3 Synaptic properties of the L10 → Ipc and the Ipc → L10 connections. (**a**) Brief electrical stimulation with a biphasic current pulse (200 μA, 500 μs) in tectal layer 10 evoked an EPSPs plus spikes or just EPSPs in the recorded Ipc neurons. Inset: Synaptic current recorded from an Ipc neuron in voltage clamp in response to electrical stimulation in tectal layer 10 with a train of 5 pulses of 20 ms interval. The membrane potential was held at –70 mV (scale bars = 20 ms, 200 pA). (**b**) Brief electrical stimulation in the Ipc nucleus evoked long-lasting EPSPs in recorded L10 neurons. Note the different scale bars in (a) and (b).

3.3.2 Determining experimentally constrained model parameters

For our model investigation into the mechanisms of oscillatory burst generation, we considered leaky integrate-and-fire model neurons, representing the L10 and the Ipc neuron in the avian isthmotectal system. The cellular properties of a model neuron (Eq. (1) to (5)) are specified by 8 parameters. We constrained the parameters by comparing the simulated responses of the L10 and Ipc model neurons (Eq. (1) and (2)) to depolarizing current injections (Fig. 3.4) with the experimental results (Fig. 3.2). A L10 (Fig. 3.4(a)) or Ipc (Fig. 3.4(b)) model neuron responds with a regular spike train to an injected current pulse. Because of the spike-rate adaptation (Eq. (3) to (5)), a model neuron responds with a short inter-spike-interval (ISI) between successive spikes at the

onset of a current pulse. The ISI then increases with time t after the current pulse onset and reaches a steady state within the duration of the current pulse. From the simulated spike train, we calculated the average firing rate, dividing the number of spikes by the duration of the current pulse. We repeated this procedure for different current amplitudes. We then derived the model F-I curve by fitting a linear function through the calculated average firing rates (Fig. 3.4(c), (d)). We also calculated the inter-spike-interval (ISI) between successive spikes in the simulated spike train and fitted an exponential function to the calculated values (Fig. 3.4(e), (f)). All 8 cellular parameter values (Table 3.1) were tuned within their experimental constraints until the model F-I curve and the ISI functions for all current amplitudes (Table. 3.2 and 3.3) matched the experimental data (Fig. 3.4(c) to (f)). The 8 cellular parameter values for each neuron were then kept fixed for all the simulations presented in the paper.

The model contains two types of synapses (Eq. (6) to (8)), each of which is described by 4 parameters. We adopted the synaptic reversal potential from the literature. The L10 → Ipc projection is mediated in part by glutamate receptor subtypes GluR1 or GluR2/3 (Hellmann et al. 2001) and is blocked by CNQX (Marin et al. 2007). Therefore, we assume a standard value of $E_{L10\rightarrow Ipc} = 0$ mV for the synaptic reversal potential of the glutamate receptor channel complex (Koch 1999). Ipc neurons also show a strong somatic staining for the α7 subunit of nicotinic acetylcholine receptors (nAChR) (Britto et al. 1992; Wang et al. 2006). Since the reversal potential for the nAChR channel complex of –5 mV (Koch 1999) is close to the synaptic reversal potential of 0 mV, we did not add the nAChR channel complex as a separate pathway in the model L10 → Ipc

projection. Ipc neurons project with dense cholinergic axonal terminals across many tectal layers (Bagnoli et al. 1992; Hellmann et al. 2001; Medina and Reiner 1994; Sorenson et al. 1989; Wang et al. 2006). Therefore, for the Ipc →L10 projection, we assumed $E_{Ipc\to L10} = -5$ mV, which is a typical reversal potential for the nAChR channel complex (Koch 1999). The time course of the synaptic conductance change is determined by two time constants (Eq. (7)). For the Ipc model neuron with AMPA synaptic conductances (Hellmann et al. 2001; Marin et al. 2007) typical rise time values, $\tau_{rise,L10\to Ipc} = 0.32$ ms, and fall time values, $\tau_{1,L10\to Ipc} = 5.6$ ms, were taken from the literature (Destexhe et al. 1994) and are consistent with the estimates based on our recordings (Fig. 3.3a). Matching L10 model neuron synaptic response to the recordings (Fig. 3.3b) led to a synaptic rise time of $\tau_{rise,Ipc\to L10} = 1.1$ ms and a fall time of $\tau_{1,Ipc\to L10} = 10$ ms. With the chosen values for the synaptic time constants, the time courses of the model synaptic responses (Fig. 3.4(g), (h)) reproduce slow EPSPs in the L10 neuron (Fig. 3.3(b)) and fast EPSPs in the Ipc neuron (Fig. 3.3(a)). Note that the maximum synaptic conductance is not constrained by the in vitro measurement. The extracellular stimulation was not limited to single-axon stimulation, rather the number of stimulated synaptic inputs depended on the chosen stimulus current and the position of the stimulus electrode relative to the presynaptic axons.

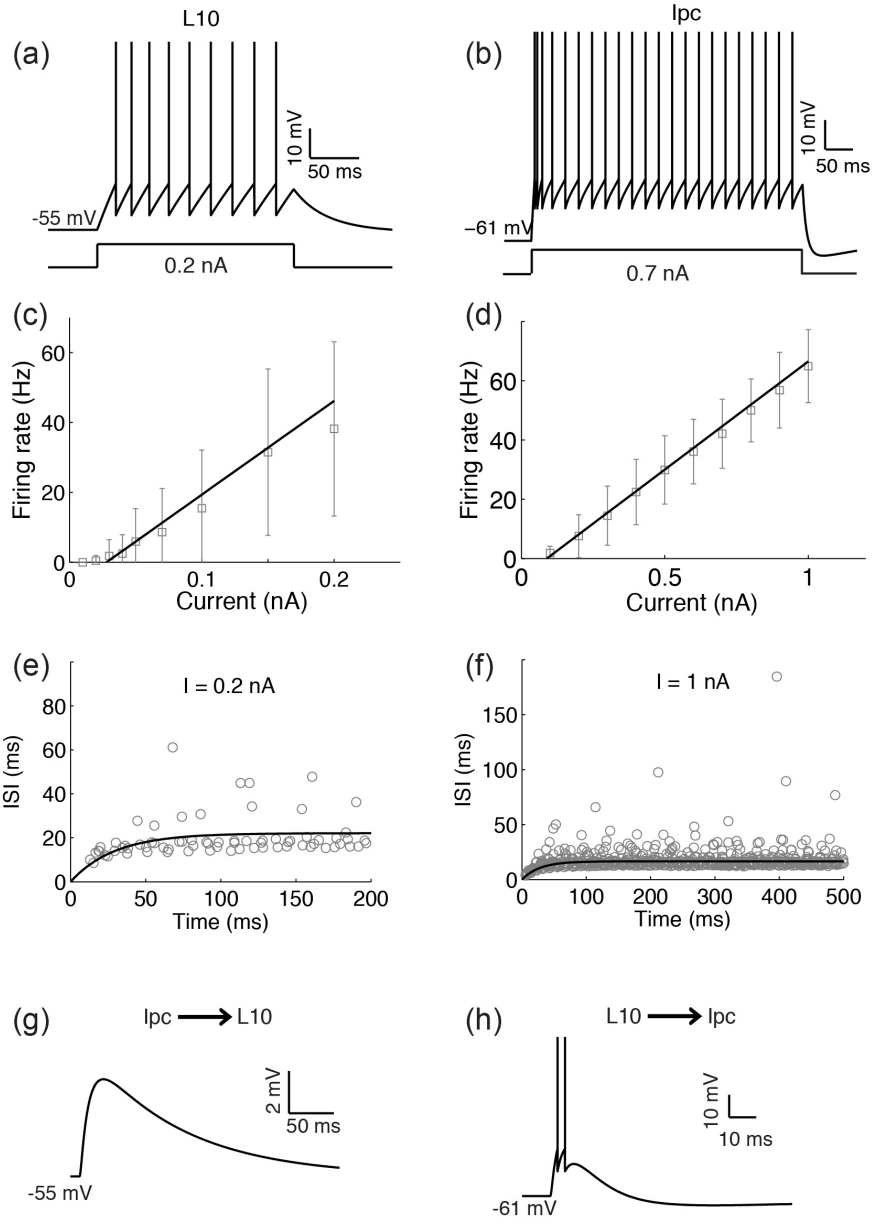

Figure 3.4 Cellular and synaptic properties of L10 and Ipc model neurons. (**a**) The response of the L10 model neuron to an injected current pulse of 0.2 nA amplitude. (**b**) The response of the Ipc model neuron to an injected current pulse of 0.7 nA amplitude. (**c**) The fitted F-I curve of the L10 model neuron, $F(I) = 268.4 \times I - 7.5$; $r^2 = 0.9883$. The experimental data (average firing rates from Fig. 3.2(c)) of the recorded real L10 neurons in response to current injections are shown for comparison (gray squares). (**d**) The fitted F-I curve of the Ipc model neuron, $F(I) = 73.0 \times I - 6.5$; $r^2 = 0.9992$. The experimental data (average firing rates from Fig. 3.2(f)) of the recorded real Ipc neurons in response to current injections are shown for comparison (gray squares). (**e**) The fitted ISI curve, $ISI(t) = A(1 - \exp(-t / B))$, of the L10 model neuron for a current injection of

0.2 nA (see Table 3.2). The experimental data from 9 recorded real L10 neurons in response to the same current injection are shown for comparison (gray circles). (**f**) The fitted ISI curve, $ISI(t) = A(1 - \exp(-t/B))$, of the Ipc model neuron for a current injection of 1.0 nA (see Table 3.3). The experimental data from 18 recorded real Ipc neurons in response to the same current injection are shown for comparison (gray circles). (**g**) The synaptic response of the L10 model neuron to a single pre-synaptic action potential. The synaptic parameters were $g_{Ipc \to L10} = 2.08$ nS, $\tau_{1,Ipc \to L10} = 10$ ms, $\tau_{2,Ipc \to L10} = 1$ ms and the cellular parameters were the same as described in the text and Table 3.1. (**h**) The synaptic response of an Ipc neuron to a single pre-synaptic action potential. The synaptic parameters were $g_{L10 \to Ipc} = 5.2$ nS, $\tau_{1,L10 \to Ipc} = 5.6$ ms, $\tau_{2,L10 \to Ipc} = 0.3$ ms, and the cellular parameters were the same as described in the text and Table 3.1. The synaptic input caused the Ipc neuron to spike two times in a short period of time. The number of spikes depends on the chosen value of the maximum synaptic conductance.

3.3.3 Mechanisms of oscillatory bursting in a reciprocally coupled pair of L10 and Ipc model neurons

Armed with the biologically plausible and experimentally constrained description of the cellular and synaptic properties of individual L10 and Ipc model neurons, we next investigated whether a reciprocally coupled pair of neurons (Fig. 3.5(a)) could generate oscillatory bursting in the Ipc model neuron in response to a plausible retinal representation of a flash of light. Since a brief flash of light generates long-lasting evoked potentials in tectal superficial layers in vivo (Holden 1980; Letelier et al. 2000), we simulated the retinal input by a depolarizing current pulse of 0.2 nA amplitude and 350 ms duration into the L10 model neuron. For the chosen values of a strong L10 → Ipc and a weak Ipc → L10 maximum synaptic conductance, the current injection generates a regular sequence of spikes with an average firing rate of 51 Hz in the L10 model neuron (Fig. 3.5(b)). Concurrently, the Ipc model neuron responds with a short burst of spikes to

every presynaptic L10 spike, thus generating oscillatory bursting in the Ipc model neuron (Fig. 3.5(c)).

Our model simulation shows that the recorded oscillatory bursts in Ipc neurons in response to a flash of light (Marin et al. 2005) can be mediated by feedforward mechanisms alone. Qualitatively, the following sequence of events causes Ipc oscillatory bursts. The retina and its tectal projection transform a brief flash of light into a long-lasting L10 synaptic current (approximated as an external current input in the model), which in turn causes the L10 neuron to spike. The L10 neuron spike generates a large depolarizing synaptic current in the Ipc neuron. The synaptic current is sufficiently strong to generate a spike and to push the membrane potential repeatedly from the reset value to the threshold for spiking, thus generating a burst of multiple spikes with ISIs of less than 4 ms. A synaptic and a cellular mechanism jointly contribute to the termination of the burst; the short duration of the synaptic current, determined by the synaptic fall time, $\tau_{1,L10\to Ipc}$, and the activation of the spike-rate adaptation current with every Ipc spike. The arrival of the next L10 spike, approximately 20 ms after the previous one in the displayed simulation (Fig. 3.5(b)), evokes the next burst in the Ipc neuron. Since the L10 neuron responds to the flash-induced long-lasting L10 synaptic current with a regular spike train, the Ipc neuron also responds with a regular sequence of bursts. In short, regular sequences of L10 spikes are transformed into regular sequences of Ipc bursts.

Current (nA)	A (ms)		B (ms)		r^2	
	Exp	Theo	Exp	Theo	Exp	Theo
0.1	31.53	51.37	22.35	48.57	0.092	0.996
0.15	24.74	30.97	27.13	35.90	0.046	0.998
0.2	22.78	22.11	26.55	29.33	0.089	0.980

Table 3.2 Fitting ISI curves, $ISI = A(1-\exp(-t/B))$, to calculated ISI data points from recorded and simulated spike trains for L10 neurons. The small r^2 values for the experimental data are due to the large variations of ISI values between cells, which are also reflected in the large SD of the measured firing rates (Fig. 3.2). The values of A, B and r^2 for 0.2 nA correspond to Fig. 3.4(e)

This mechanism of Ipc oscillatory burst generation is valid for the parameter area that represents a strong feedforward L10 → Ipc and a weak feedback Ipc → L10 maximum synaptic conductance (Fig. 3.5(d)). For reduced L10 → Ipc maximum synaptic conductance, only sequences of Ipc spikes rather than bursts are generated. Interestingly, the Ipc → L10 feedback can render the L10 spike train more irregular, but is not necessary for the Ipc burst generation. Rather, for increased Ipc → L10 feedback maximum synaptic conductance, the two neurons excite each other continuously and the system transitions into a diverging regime. Another important parameter is the feedforward synaptic fall time, $\tau_{1,L10\to Ipc}$, which contributes to the termination of the burst. For increasing values of $\tau_{1,L10\to Ipc}$, significant temporal summation of EPSPs occurs in the Ipc neuron, the Ipc spike-rate adaptation is not enough to terminate the bursts, and the system transitions into a diverging regime (Fig. 3.5(e), (f)). The numerical value of $\tau_{1,L10\to Ipc}$ at which the transition to divergence occurs decreases with decreasing ISI of the L10 neuron, which of course depends on the chosen value of the retinal input; 0.2 nA for

the simulation results shown in Fig. 3.5. For decreasing values of the feedforward synaptic fall time, $\tau_{1,L10\to Ipc}$, the time for burst generation is too short and only isolated Ipc spikes occur. Thus, there is a limited range of parameter values for burst generation (Fig. 3.5(f)). With decreasing $\tau_{1,L10\to Ipc}$ values the burst generation becomes more robust to the value of the feedforward maximum synaptic values, $g_{L10\to Ipc}$.

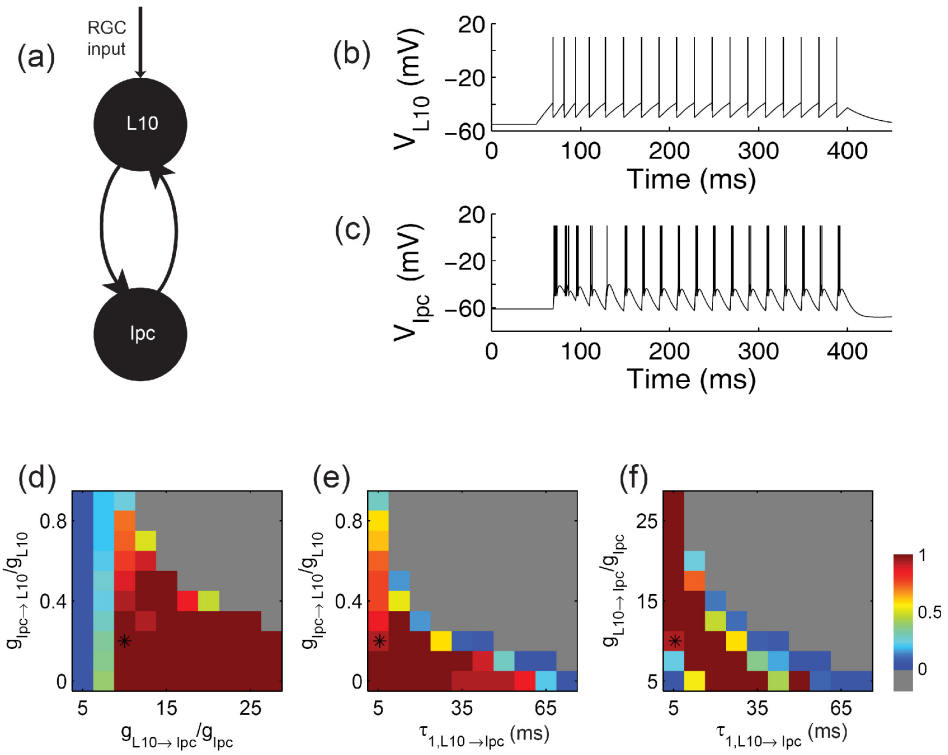

Figure 3.5 Generation of oscillatory bursting in a pair of model neurons with recurrent excitation. (**a**) Schematic drawing of the reciprocally coupled pair of L10 and Ipc model neurons with retinal (RGC) inputs to the L10 model neuron. (**b**) and (**c**) Responses of the reciprocally coupled L10 and Ipc model neurons to depolarizing current injection into the L10 model neuron. The injected current had a duration of 350 ms (starting at time = 50 ms) and an amplitude of 0.2 nA. The cellular and synaptic parameter values were chosen as described in the text and Table 3.1. The maximum synaptic conductances relative to the membrane conductance were $g_{L10\to Ipc}/g_{Ipc}=10$ and $g_{Ipc\to L10}/g_{L10}=0.2$. The Ipc burst score (see Methods) for this trace equals $14/15\cong 0.93$. (**d**), (**e**), (**f**) Ipc responses for three cross sections through the 3-dimensional parameter space spanned by the maximum synaptic conductances $g_{L10\to Ipc}/g_{Ipc}$ and $g_{Ipc\to L10}/g_{L10}$, and by the feedforward synaptic

fall times $\tau_{1,L10\to Ipc}$. The three cross sections intersect the point (asterisk) 10, 0.2, 5.6 ms, respectively, which is also the parameter set chosen for the sample trace in (b) and (c). The Ipc responses are represented in pseudo color by the burst score. When all spikes belong to bursts the score is 1 (red), when all spikes are isolated the score is 0 (blue), when the firing rate exceeds 1000 Hz the Ipc response is classified as diverging (gray).

3.3.4 A population of L10 and Ipc neurons with spontaneous activity

Does the mechanism of oscillatory bursting in a reciprocally coupled pair of L10 and Ipc model neurons extend to populations of neurons? Because of the finite width of the L10→Ipc projection (Wang et al. 2006), an Ipc neuron, embedded within the isthmo-tectal system, receives synaptic inputs from more than one L10 neuron. Further, because of the high level of spontaneous activity (Maczko et al. 2006; Sherk 1979), the Ipc neuron may receive uncorrelated inputs at such a high frequency that it will spike tonically, not burst. This raises an important question: Under what conditions does this simple mechanism of oscillatory burst generation break down in a population of L10 and Ipc neurons with spontaneous activity when each Ipc neuron receives inputs from many L10 neurons?

To address this question we investigated a population model of L10 and Ipc neurons with topographic reciprocal excitation (Fig. 3.6(a)) and spontaneous activity. Important model parameters are the widths, $\Delta_{L10\to Ipc}$ and $\Delta_{Ipc\to L10}$, of the projections, which determine the strength of synaptic inputs from other neurons, and the standard deviations, σ_e, σ_{L10} and σ_{Ipc},of the noise currents, which determine the uncorrelated activity of neurons. For a set of parameters within the bursting regime, a stimulus current step delivered to a group of L10 neurons (centered around L10 neuron #200) generates oscillatory bursts in Ipc

neuron #200 (Fig. 3.6(b)). Because of the width and the strength of the L10 → Ipc projection, the spiking activity spreads to numerous Ipc neurons beyond the group of Ipc neurons that correspond to the topographic projection of the directly stimulated group of L10 neurons. In contrast, the feedback projection, Ipc → L10, of the same width, is too weak to generate L10 spikes beyond the group of directly stimulated L10 neurons. The feedback projection does however cause dispersion in the timing of L10 spikes, i.e., because of the larger summation of excitatory feedback, L10 neurons in the center spike earlier than L10 neurons away from the center. The uncorrelated L10 activity introduces variability in the Ipc burst duration.

For narrow feedback, i.e., $\Delta_{Ipc \to L10}$ is small, the number of correlated L10 inputs to an Ipc neuron increases with increasing width, $\Delta_{L10 \to Ipc}$, of the feedforward projection and thus the Ipc neuron generates more bursts rather than isolated spikes (Fig. 3.6(c)). However, for broad feedback, L10 spike trains from neurons away from the center are less correlated. Thus, with increasing width of the feedforward projection, Ipc burst generation increases only over a narrow range then the Ipc activity diverges. In this parameter region, the adaptation current is not sufficient to prevent the system from diverging.

Because of the strong feedforward synapse, Ipc burst generation is very sensitive to uncorrelated noise in L10 neurons. The mechanism of feedforward burst generation breaks down when the value of the standard deviations, σ_e or σ_{L10}, of the noise currents approach the chosen mean value, 0.18 nA, of the stimulus current (Fig. 3.6(d) and (e)).

Because of the weak feedback connection and suppressive effect of adaptation current, Ipc burst generation is much less sensitive to uncorrelated noise current into Ipc neurons (Fig. 3.6(f)).

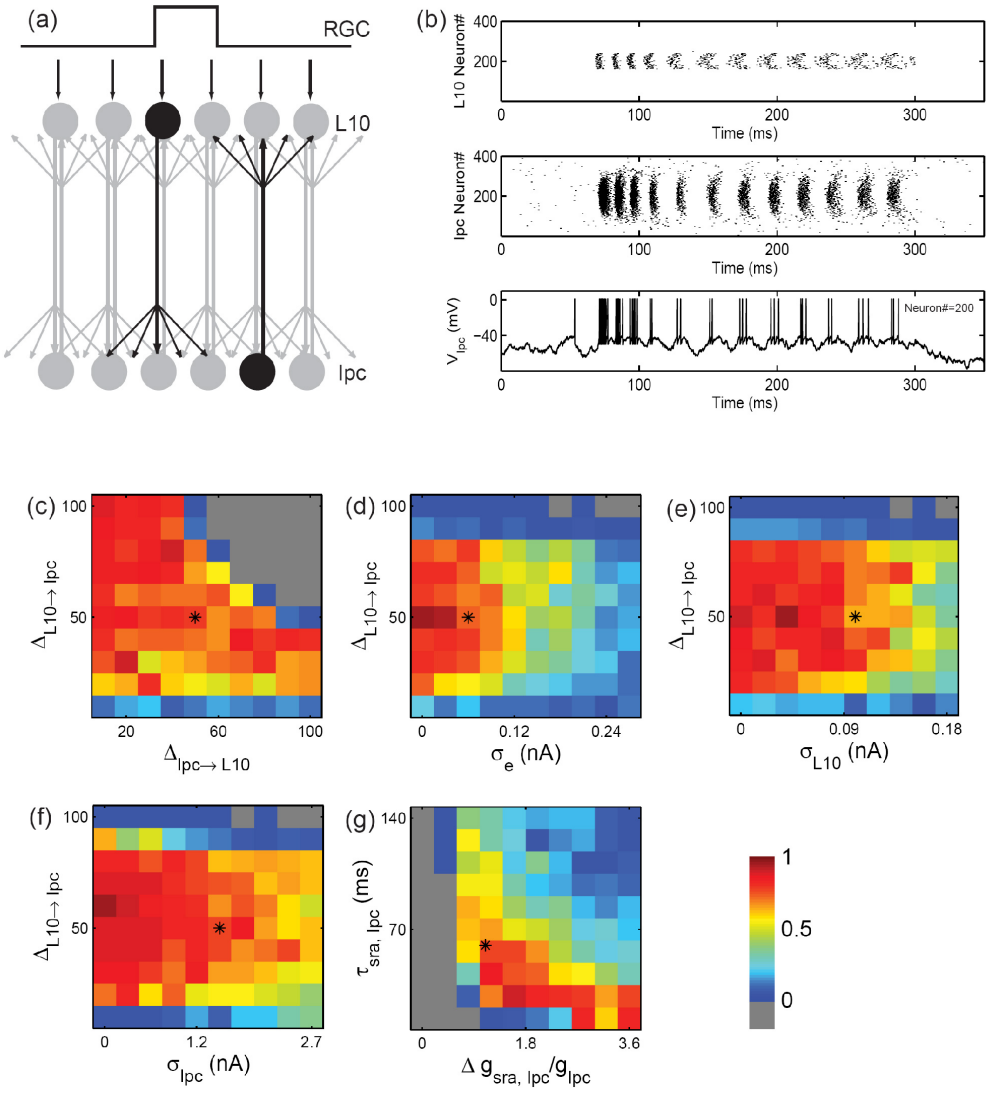

Figure 3.6 Generation of oscillatory bursts in a population model with recurrent excitation and uncorrelated noise. (**a**) Schematic drawing of the reciprocally coupled populations of L10 and Ipc model neurons with local RGC inputs to a small group of L10 neurons. The projections are topographic, but have a certain width as indicated by the spread of arrows. (**b**) Sample L10 and Ipc population responses (raster plot of spikes) to a stimulus current step delivered to 80 neurons centered on L10 neuron #200. The concurrent voltage response of Ipc neuron #200 is shown in the bottom trace. Single

neuron parameters are listed in Table 3.1. The stimulus, synaptic, and noise parameters are: $I_0 = 0.18$ nA, $g_{L10\to Ipc} = 1.85$ nS, $g_{Ipc\to L10} = 4.69\times10^{-3}$ nS, $\Delta_{L10\to Ipc} = 50$, $\Delta_{Ipc\to L10} = 50$, $\sigma_e = 0.06$ nA, $\sigma_{Ipc} = 1.5$ nA, $\sigma_{L10} = 0.1$ nA. The stimulus current is turned on at $t = 50$ ms and lasts for 250 ms. (**c**) to (**f**) Ipc responses for four cross sections through the 5-dimensional parameter space spanned by the spatial width of the synaptic weight distributions $\Delta_{L10\to Ipc}$ and $\Delta_{Ipc\to L10}$, and the white noise standard deviations σ_e, σ_{Ipc}, and σ_{L10}. The four cross sections intersect the point (asterisk) 50, 50, 0.06 nA, 1.5 nA, 0.1 nA, respectively, which is also the parameter set chosen for the sample trace in (b). The Ipc responses are represented in pseudo color (see Fig. 3.5) by the "average burst score", which is the burst score (see Methods) averaged over 5 trials. (**g**) Ipc responses for different values of the Ipc spike-rate adaptation increment, $\Delta g_{sra,Ipc}$, and the decay time constant, $\tau_{sra,Ipc}$. All other parameters are as in (b).

In contrast, Ipc burst generation is less sensitive to noise in L10 neurons when the noise is correlated. Because of common inputs to adjacent L10 neurons, noise correlations in the L10 input currents are likely to exist. Given the potential importance of noise correlations for burst generation and stimulus representation in sensory systems (Chacron and Bastian 2008), we investigated the role of noise correlations in the isthmo-tectal system. We simulated the population model with correlated noise, $\eta_{e,i}$, in the external current input, $I_{e,i} = (I_0 + \eta_{e,i})$, to the subset of L10 neurons, labeled $i = 160$ to $i = 240$. The noise correlation in the external current input to two L10 neurons, i and i', decreases with distance as described by $\left\langle \eta_{e,i}(t)\eta_{e,i'}(t')\right\rangle = 2\sigma_e^2 \exp(-|i-i'|/\lambda)\delta(t-t')$, where λ represents a correlation length (Abbott and Dayan 1999). In the limit of $\lambda \to 0$, we recover the case of uncorrelated noise, $\left\langle \eta_{e,i}(t)\eta_{e,i'}(t')\right\rangle = 2\sigma_e^2\delta(t-t')\delta_{ii'}$. It is instructive to start the simulation with uncorrelated noise with a large standard deviation, $\sigma_e = 0.2$ nA, comparable to the value of the constant component, I_0. In this case, L10

neurons produce largely uncorrelated spike trains and Ipc neurons do not burst (burst score below 0.3; Fig. 3.6(d)). However, with increasing noise correlation, spike trains of stimulated L10 neurons become more correlated and Ipc bursting resumes. For instance, with a correlation length of $\lambda = 30$ the burst score reaches 0.9 (data not shown).

The Ipc spike-rate adaptation conductance is determined by the decay time constant, $\tau_{sra,Ipc}$, and the conductance increment, $\Delta g_{sra,Ipc}$. Interestingly, the two-dimensional parameter space reveals a narrow region for Ipc burst generation (Fig. 3.6(g)). For the conductance increment decreasing from this region, the Ipc neuron activity diverges as expected, since spike-rate adaptation is the only activity-dependent regulatory mechanism in this network of reciprocal excitation. For the conductance increment increasing from this region, the Ipc neuron produces isolated spikes, rather than bursts, to synaptic inputs. Similarly, Ipc activity diverges with decreasing decay time constant and transitions to tonic spiking when the time constant increases.

Since some Ipc recordings displayed a spike after-depolarization (ADP) and since in general ADPs can provide a mechanism for bursting (Higgs and Spain 2009), the potential role of ADPs in the case of Ipc bursting was evaluated. We implemented ADPs in the Ipc model neuron using a simple formalism (Doiron et al. 2007), where each Ipc spike triggers a delayed depolarizing current (see Sec. 2.3). Simulation results with the ADP included indicate that the ADP is not necessary for Ipc burst generation; however the ADP slightly enlarges the region of parameter space for burst generation (data not shown) compared to Ipc model neurons without ADPs (Fig. 3.6(g)).

3.4 Discussion

We measured the cellular and synaptic properties of avian L10 and Ipc neurons in vitro. We found regular spiking neurons with spike-rate adaptation. We also found reciprocal excitation, with a strong and brief feedforward L10 → Ipc and a weak and long-lasting feedback Ipc → L10 synaptic conductance change. Our simulation of an experimentally constrained excitatory neural network reveals that Ipc oscillatory burst generation in response to simulated retinal inputs to L10 neurons can be mediated by regular L10 neuron spiking combined with Ipc burst responses to an L10 spike. The mechanism requires a strong and brief feedforward synaptic conductance change and is aided by Ipc spike-rate adaptation. The measured weak and long-lasting feedback synaptic conductance change is not necessary for Ipc oscillatory burst generation. Increasing components of uncorrelated Ipc inputs force a transition from oscillatory bursting to irregular tonic spiking.

3.4.1 Excitatory neural networks with adaptation

The mechanisms of oscillatory burst generation typically have in common a fast excitatory current causing a train of spikes and an activity-dependent slow inhibitory current that interrupts the spike train (Izhikevich 2007; Marder and Calabrese 1996). However, purely excitatory neural networks can produce oscillatory bursts as well (Feller 1999; O'Donovan 1999; Smith et al. 1991). In these networks, recurrent excitation mediates episodes of activity, which is terminated by activity-dependent depression or adaptation (Hansel et al. 1995; Nesse et al. 2008; Tabak et al. 2000; Tabak and Rinzel

2005; Van Vreeswijk and Hansel 2001; Vladimirski et al. 2008) rather than inhibitory synaptic currents.

Adaptation affords a rich repertoire of neurophysiological effects (Kohn 2007). Our model simulations indicate that the Ipc spike-rate adaptation current plays an important role in terminating the burst. The oscillatory bursts in Ipc neurons are evoked by the strong projection from periodically firing L10 neurons. Without the adaptation current, the burst duration is largely determined by the synaptic fall time, $\tau_{1,L10\to Ipc}$. For increasing values of $\tau_{1,L10\to Ipc}$, a small increase in maximum synaptic conductance, $g_{L10\to Ipc}$ and $g_{Ipc\to L10}$, would push the system from bursting to diverging. In contrast, when the Ipc spike-rate adaptation current is present, it provides an activity-dependent negative feedback that terminates the bursts after a few spikes. Ipc spike-rate adaptation thus enlarges the volume for bursting in the three-dimensional parameter space (Fig. 3.5(d), (e), (f)). Two parameters, the decay time constant, $\tau_{sra,Ipc}$, and the conductance increment, $\Delta g_{sra,Ipc}$, specify the Ipc spike-rate adaptation conductance. The population model investigation reveals a narrow area for bursting in this two-dimensional parameter space (Fig. 3.6(g)).

Current (nA)	A (ms)		B (ms)		r^2	
	Exp	Theo	Exp	Theo	Exp	Theo
1	17.47	16.68	20.47	27.48	0.36	0.97
0.9	19.36	18.73	20.85	28.56	0.25	0.97
0.8	22.62	21.37	22.04	30.15	0.25	0.96
0.7	27.22	24.84	24.21	31.94	0.24	0.96
0.6	32.44	28.68	29.55	34.68	0.15	0.95
0.5	42.67	36.82	33.81	38.30	0.089	0.95
0.4	52.22	48.49	34.09	44.42	0.027	0.91

Table 3.3 Fitting ISI curves, $ISI = A(1-\exp(-t/B))$, to calculated ISI data points from recorded and simulated spike trains for Ipc neurons. The small r^2 values for the experimental data are due to the large variations of ISI values between cells, which are also reflected in the large SD of the measured firing rates (Fig. 3.2). The values of A, B and r^2 for 1.0 nA correspond to Fig. 3.4(f).

Spike-rate adaptation is often mediated by potassium currents with slow inactivation (Brown et al. 1990; Brownstone 2006; Lewis et al. 1986; Storm 1990). In the phenomenological description chosen for our model, the parameter values for the spike-rate adaptation (Table 3.1) are experimentally constrained by the measured $F(I)$ and $ISI(t)$ curves (Fig. 3.4). The fact that the $ISI(t)$ curves for model and real neurons are well matched for all current injection values considered (Fig. 3.4(e), (f) and Table 3.2, 3.3), indicates that the leaky integrate-and-fire model provides a good approximation for the real L10 and Ipc neurons.

3.4.2 Brief feedforward synaptic conductance changes

Even with the experimentally constrained spike-rate adaptation included, oscillatory burst generation requires the synaptic fall time, $\tau_{1,L10\rightarrow Ipc}$, to be well below 100 ms (Fig. 3.5(e), (f)). With increasing synaptic fall times the excitatory synaptic potentials in the Ipc neuron sum. As a result the system activity transits into the diverging regime even for small synaptic conductances. This model result is consistent with the observation that the L10 → Ipc projection is mediated by AMPA-type glutamate receptors (Hellmann et al 2001; Marin et al. 2007) and possibly by nicotinic acetylcholine receptors (Britto et al. 1992; Wang et al. 2006); both of which have the required short synaptic fall times (Destexhe et al. 1994).

3.4.3 Neuronal noise produces variable burst durations

The consequences of neuronal noise and correlations on the integrative properties of neural systems have received increasing attention in recent years (Averbeck et al. 2006; Chance et al. 2002; Destexhe and Contreras 2006; Destexhe and Rudolph 2009; Fox et al. 2006; Wolfart et al. 2005). Ipc bursts in vivo have variable burst durations (Marin et al. 2005). Our population model provides a simple explanation. Uncorrelated L10 activities, mediated by noise currents, add variability to the Ipc burst duration (Fig. 3.6(b)). With increasing noise levels the Ipc response transitions from bursting to irregular spiking (Fig. 3.6(d), (e)). Because of the weak feedback connection and the suppressive effect of adaptation current, the mechanism of Ipc burst generation is less sensitive to noise currents into Ipc neurons (Fig. 3.6(f)).

3.4.4 The cholinergic feedback is weak

We recorded a slow and long-lasting Ipc → L10 synaptic potential change (Fig. 3.3(b)). This observation is consistent with, but does not test, the previously discussed hypothesis that the cholinergic feedback to the optic tectum might be mediated by a paracrine mode of synaptic transmission (Gruberg et al. 1994; Sargent et al. 1989; Sereno and Ulinski 1987; Wang et al. 2006).

Our model simulations indicate that the Ipc → L10 feedback is not necessary for the Ipc oscillatory burst generation (Fig. 3.5(d)). However, these model results can not exclude the possibility that feedback may contribute to the oscillatory burst generation in vivo via mechanisms not included in the simple model. For instance, cholinergic feedback may control the excitability (Kawai et al. 2007) of RGC axons, the calcium influx into RGC axon terminals (Dudkin and Gruberg 2003) and thus synaptic transmission, or may activate GABAergic tectal circuits (Luksch and Golz 2003) with potentially inhibitory effect on L10 neurons.

Feedback in our model can affect the oscillatory burst pattern. With increasing feedback strength the L10 spike train pattern, and thus the Ipc oscillatory burst pattern, becomes more irregular. Interestingly, the related concept of spike-triggered feedback currents has previously been included in leaky integrate-and-fire models to provide more realistic model responses (Jolivet et al. 2004; Paninski et al. 2004 Pillow et al. 2005).

When the Ipc → L10 feedback increases above a critical value, the L10 and Ipc neuron excite each other continuously and the system transitions into a diverging regime (Fig. 3.5(d)). The latter observation is consistent with the 'no-strong-loops hypothesis' (Crick and Koch 1998), which states that a strong excitatory loop formed between two cortical areas would lead the system into uncontrolled oscillations (Schnitzler and Gross 2005).

Although the Ipc → L10 feedback is apparently weak and is not required for the oscillatory burst generation, cholinergic feedback is involved in tectal visual processing. For instance, cholinergic feedback enhances calcium influx into optic nerve fiber terminals in frog (Dudkin and Gruberg 2003) and inactivation of cholinergic feedback prevents visual responses in the ascending visual pathway to the nucleus rotundus in birds (Marin et al. 2007). Bursts facilitate synaptic transmission across unreliable synapses via increased transmitter release (Izhikevich et al. 2003; Lisman 1997; Sherman 2001). We expect this effect to be significant for paracrine transmission in the cholinergic feedback as well. In conclusion, delivering the cholinergic feedback via oscillatory bursting Ipc axon terminals in the tectum is likely to be of great importance for the population coding of visual information in the intricate retino-tecto-rotundal pathway (Khanbabaie et al. 2007; Luksch et al. 1998, 2001, 2004; Mahani et al. 2006; Marin et al. 2003).

3.5 Acknowledgement

The authors thank Gonzalo Marin for stimulating discussions that helped to define key model assumptions and thank Michael Ariel, Adam Eggebrecht, and Gonzalo Marin for critical reading of early versions of the manuscript.

3.6 Grants

The work was supported by National Eye Institute Grant R01 EY-15678 to R. Wessel and by DFG Grant Lu 622 8-2 to H. Luksch.

3.7 Reference

Abbott LF, & Dayan P (1999) The effect of correlated variability on the accuracy of a population code. Neural Computation 11: 91-101.

Averbeck BB, Latham PE, & Pouget A (2006) Neural correlations, population coding and computation. Nature Reviews Neuroscience 7: 358-366.

Bagnoli P, Fontanesi G, Alesci R, & Erichsen J (1992) Distribution of neuopeptide Y, substance P, and choline acetyltransferase in the developing visual system of the pigeon and effects of unilateral retina removal. Journal of Comparative Neurology 318: 392-414.

Brandt SF, Pelster A, & Wessel R (2006) Variational calculation of the limit cycle and its frequency in a two-neuron model with delay. Phys Rev E 74: 036201.

Brandt SF, & Wessel R (2007) Winner-take-all selection in a neural system with delayed feedback. Biol Cybernetics 97: 221-228.

Brandt SF, Pelster A, & Wessel R (2007) Synchronization in a neuronal feedback loop through asymmetric temporal delays. Europhysics Letters 79: 38001.

Britto LR, Keyser KT, Lindstrom JM, & Karten HJ (1992) Immunohistochemical localization of nicotinic acetylcholine receptor subunits in the mesencephalon and diencephalon of the chick (Gallus gallus). Journal of Comparative Neurology 317: 325-340.

Brown DA, Gähwiler BH, Griffith WH, & Halliwell JV (1990) Membrane currents in hippocampal neurons. Progress in Brain Research 83: 141-160.

Brownstone RM (2006) Beginning at the end: repetitive firing properties in the final common pathway. Progress in Neurobiology 78: 156-172.

Buzsaki G (2006) Rhythms of the brain. Oxford University Press.

Chacron MJ, Longtin A, & Maler L (2005) Delayed excitatory and inhibitory feedback shape neural information transmission. Physical Review E 72: 051917.

Chacron MJ, & Bastian J (2008) Population coding by electrosensory neurons. Journal of Neurophysiology 99: 1825-1835.

Chance FS, Abbott LF, & Reyes AD (2002) Gain modulation from background synaptic input. Neuron 35: 773-782.

Crick F, & Koch C (1998) Constraints on cortical and thalamic projections: the no-strong-loops hypothesis. Nature 391: 245-250.

Cook RG (2001) Avian visual cognition. Available on-line at: www.pigeon.psy.tufts.edu/avc/

Coombes S, & Bressloff PC (2005) Bursting: the genesis of rhythm in the nervous system. World Scientific Press.

Destexhe A, Mainen ZF, & Sejnowski TJ (1994) Synthesis of models for excitable membranes, synaptic transmission and neuromodulation using a common kinetic formalism. Journal of Computational Neuroscience 1: 195-230.

Destexhe A, & Contreras D (2006) Neuronal computations with stochastic network states. Science 314: 85-90.

Destexhe A, & Rudolph M (2009) Neuronal noise. Springer.

Doiron B, Chacron MJ, Maler L, Longtin A, Bastian J (2003) Inhibitory feedback required for network oscillatory responses to communication but not to prey stimuli. Nature 421: 539-543.

Doiron B, Oswald AMM, & Maler L (2007) Interval coding. II. Dendrite-dependent mechanisms. Journal of Neurophysiology 97: 2744-2757.

Dudkin EA, & Gruberg ER (2003) Nucleus isthmi enhances calcium influx into optic nerve fiber terminals in Rana pipiens. Brain Research 969: 44-52.

Dye JC, & Karten HJ (1996) An in vitro study of retinotectal transmission in the chick: role of glutamate and GABA in evoked field potentials. Visual Neuroscience13:747–758.

Feller MB (1999) Spontaneous correlated activity in developing neural circuits. Neuron 22: 653-656.

Fox MD, Snyder AZ, Zacks JM, & Raichle ME (2006) Coherent spontaneous activity accounts for trial-to-trial variability in human evoked brain responses. Nature Neuroscience 9: 23-25.

Gabbiani F, Metzner W, Wessel R, & Koch C (1996) From stimulus encoding to feature extraction in weakly electric fish. Nature 384: 564-567.

Gruberg ER, Hughes TE, & Karten HJ (1994) Synaptic interrelationships between the optic tectum and ipsilateral nucleus isthmi in Rana pipiens. Journal of Comparative Neurology 339: 353-364.

Hansel D, Mato G, & Meunier C (1995) Synchrony in excitatory neural networks. Neural Computation 7: 307-337.

Hellmann B, Manns M, & Güntürkün O (2001) Nucleus isthmi, pars semilunaris as a key component of the tectofugal visual system in pigegons. Journal of Comparative Neurology 436: 153-166.

Higgs MH, & Spain WJ (2009) Conditional bursting enhances resonant firing in neocortical layer 2-3 pyramidal neurons. Journal of Neuroscience 29: 1285-1299.

Holden AL (1980) Field potentials evoked in the avian optic tectum by diffuse and punctiform luminous stimuli. Experimental Brain Research 39: 427-432.

Izhikevich EM (2007) Dynamical Systems in Neuroscience: The Geometry of Excitability and Bursting. Cambridge, MA: The MIT Press.

Izhikevich EM, Desai NS, Walcott EC, & Hoppensteadt FC (2003) Bursts as a unit of neural information: selective communication via resonance. Trends in Neuroscience 26: 161-167.

Jolivet R, Lewis TJ, & Gerstner W (2004) Generalized integrate-and-fire models of neuronal activity approximate spike trains of a detailed model to a high degree of accuracy. Journal of Neurophysiology 92: 959-976.

Kawai H, Lazar R, & Metherate R (2007) Nicotinic control of axon excitability regulates thalamocortical transmission. Nature Neuroscience 10: 1168-1175.

Khanbabaie R, Mahani A, & Wessel R (2007) Contextual interaction of GABAergic circuitry with dynamic synapses. Journal of Neurophysiology 97: 2802-2811.

Knudsen EI (1982) Auditory and visual maps of spaces in the optic tectum of the owl. Journal of Neuroscience 2: 1177-1194.

Koch C (1999) Biophysics of Computation: Information Processing in Single neurons. New York: Oxford University Press, p. 85-116.

Kohn A (2007) Visual adaptation: Physiology, mechanisms, and functional benefits. Journal of Neurophysiology 97: 3155-3164.

Krahe R, & Gabbiani F (2004) Burst firing in sensory systems. Nature Review Neuroscience 5: 13-23.

Laing CR, & Longtin A (2003) Dynamics of deterministic and stochastic paired excitatory-inhibitory delayed feedback. Neural Computation 15: 2779-2822.

Lesica NA, & Stanley GB (2004) Encoding of natural scene movies by tonic and burst spikes in the lateral geniculate nucleus. Journal of Neuroscience 24: 10731-10740.

Letelier JC, Mpodozis J, Marin G, Morales D, Rozas C, Madrid C, & Velasco M (2000) Spatiotemporal profile of synaptic activation produced by the electrical and visual stimulation of retinal inputs to the optic tectum: a current source density analysis in the pigeon (Columbia livia). European Journal of Neuroscience 12: 47-57.

Lewis DV, Huguenard JR, Anderson WW, & Wilson WA (1986) Membrane currents underlying bursting pacemaker activity and spike frequency adaptation in invertebrates. Advances in Neurology 44: 235-261.

Lisman J (1997) Bursts as a unit of neural information: making unreliable synapses reliable. Trends in Neuroscience, 20: 38-43.

Luksch H, Cox K, & Karten HJ (1998) Bottlebrush dendritic endings and large dendritic fields: motion-detecting neurons in the tectofugal pathway. Journal of Comparative Neurology 396:399–414.

Luksch H, Karten HJ, Kleinfeld D, & Wessel R (2001) Chattering and differential signal processing in identified motion sensitive neurons of parallel visual pathways in chick tectum. Journal of Neuroscience 21:6440– 6446.

Luksch H, & Golz S (2003) Anatomy and physiology of horizontal cells in layer 5b of the chicken optic tectum. Journal of Chemical Neuroanatomy 25: 185-194.

Luksch H, Khanbabaie R, & Wessel R (2004) Synaptic dynamics mediate sensitivity to motion independent of stimulus details. Nature Neuroscience 7: 380-388.

Maczko KA, Knudsen PF, & Knudsen EI (2006) Auditory and visual space maps in the cholinergic nucleus isthmi pars parvocellularis in the barn owl. Journal of Neuroscience 26: 12799-12806.

Mahani AS, Khanbabaie R, Luksch H, & Wessel R (2006) Sparse spatial sampling for the computation of motion in multiple stages. Biological Cybernetics 94: 276-287.

Marin G, Letelier JC, Henny P, Sentis E, Farfan G, Fredes F, Pohl N, Karten H, & Mpodozis J (2003) Spatial organization of the pigeon tecto-rotundal pathway: An

interdigitating topographic arrangement. Journal of Comparative Neurology 458:361-380.

Marin G, Mpdozis J, Sentis E, Ossandon T, & Letelier JC (2005) Oscillatory bursts in the optic Tectum of birds represent re-entrant signals from the nucleus isthmi pars parvocellularis. Journal of Neuroscience 25: 7081-7089.

Marin G, Salas C, Sentic E, Rojas X, Letelier JC, & Mpodozis J (2007) A cholinergic gating mechanism controlled by competitive interactions in the optic tectum of the pigeon. Journal of Neuroscience 27: 8112-8121.

Marder E, & Calabrese R (1996) Principles of rhythmic motor pattern generation. Physiological Reviews 76: 687-717.

McCormick DA, & Huguenard JR (1992) A model of the electrophysiological properties of thalamocortical relay neurons. Journal of Neurophysiology 68: 1384-1400.

Medina L, & Reiner A (1994) Distribution of choline acetyltransferase immunoreativity in the pigeon brain. Journal of Comparative Neurology 342: 497-537.

Meyer U, Shao J, Chakrabarty S, Brandt SF, Luksch H, & Wessel R (2008) Distributed delays stabilize neural feedback systems. Biological Cybernetics 99: 79-87.

Milton J (1996) Dynamics of small neural populations. CRM Monograph Series.

Nesse WH, Borisyuk A, & Bressloff PC (2008) Fluctuation-driven rhythmogenesis in an excitatory neuronal network with slow adaptation. Journal of Computational Neuroscience 25: 317-333.

Neuenschwander S, & Varela FJ (1993) Visually triggered neuronal oscillations in the pigeon: an autocorrelation study of tectal activity. European Journal of Neuroscience 5: 870-881.

Neuenschwander S, Engel AK, Konig P, Singer W, & Varela FJ (1996) Synchronization of neuronal responses in the optic tectum of awake pigeons. Visual Neuroscience 13: 575-584.

O'Donovan MJ (1999) The origin of spontaneous activity in developing networks of the vertebrate nervous system. Current Opinion in Neurobiology 9: 94-104.

Oswald AM, Chacron MJ, Doiron B, Bastian J, & Maler L (2004) Parallel processing of sensory input by bursts and isolated spikes. Journal of Neuroscience 24: 4351-4362.

Paninski L, Pillow JW, & Simoncelli EP (2004) Maximum likelihood estimation of a stochastic integrate-and-fire neural encoding model. Neural Computation 16: 2533-2561.

Pillow JW, Paninski L, Uzzell VJ, Simoncelli EP, & Chichilnisky EJ (2005) Prediction and decoding of retinal ganglion cell responses with a probabilistic spiking model. Journal of Neuroscience 25: 11003-11013.

Reinagel P, Godwin D, Sherman SM, & Koch C (1999) Encoding of visual information by LGN bursts. Journal of Neurophysiology 81: 2558-2569.

Rinzel J, & Ermentrout B (1998) Analysis of neural excitability and oscillations. In: Koch C and Segev I (Eds), Methods of neuronal modeling: From Synapses to networks, 2nd edition, pp. 252-291, Cambridge: Bradford.

Sargent PB, Pike SH, Nadel DB, & Lindstrom JM (1989) Nicotinic acetylcholine receptor-like molecules in the retina, retinotectal pathway, and optic tectum of the frog. Journal of Neuroscience 9: 565-573.

Sillito AM, & Jones HE (2002) Corticothalamic interactions in the transfer of visual information. The Philosophical Transactions of the Royal Society B 357: 1739-1752

Schnitzler A, & Gross J (2005) Normal and pathological oscillatory communication in the brain. Nature Reviews Neuroscience 6: 285-296.

Sereno MI, & Ulinski PS (1987) Caudal topographic nucleus isthmi and the rostral nontopographic nucleus isthmi in the turtle, Pseudemys scripta. Journal of Comparative Neurology 261: 319-346.

Sherk H (1979) A comparison of visual-response properties in cat's parabigeminal nucleus and superior colliculus. J Neurophysiol 42: 1640-1655.

Sherman SM (2001) Tonic and burst firing: dual modes of thalamocortical relay. Trends in Neurosciences 24: 122-126.

Smith JC, Ellenberger HH, Ballanyi K, Richter DW, & Feldman JL (1991) Pre-Bötzinger complex: A brainstem region that may generate respiratory rhythm in mammals. Science 254: 726-729.

Sorenson EM, Parkinson D, Dahl JL, & Chiappinelli VA (1989) Immunohistochemical localization of choline acetyltransferase in the chicken mesencephalon. Journal of Comparative Neurology 281: 641-657.

Storm JF (1990) Potassium currents in hippocampal pyramidal cells. Progress in Brain Research 83: 161-187.

Tabak J, Senn W, O'Donovan MJ, & Rinzel J (2000) Modeling of spontaneous activity in developing spinal cord using activity-dependent depression in an excitatory network. Journal of Neuroscience 20: 3041-3056.

Tabak J, & Rinzel J (2005) Bursting in excitatory neural networks. In: Coombes S, Bressloff PC (Eds.) Bursting: the genesis of rhythm in the nervous system. Hackensack World Scientific, pp. 273-301.

Traub RD, Bibbig A, LeBeau FEN, Buhl EH, & Whittington MA (2004) Cellular mechanisms of neuronal population oscillations in the hippocampus in vitro. Annual Review of Neuroscience 27: 247-248.

Van Vreeswijk C, & Hansel D (2001) Patterns of synchrony in neural networks with spike adaptation. Neural Computation 13: 959-992.

Vladimirski BB, Tabak J, O'Donovan MJ, & Rinzel J (2008) Episodic activity in a heterogeneous excitatory network, from spiking neurons to mean field. Journal of Computational Neuroscience 25: 39-63.

Wang XJ (1994) Multiple dynamic modes of thalamic relay neurons: rhythmic bursting and intermittent phase-locking. Neuroscience 59: 21-31.

Wang SR (2003) The nucleus isthmi and dual modulation of the receptive field of tectal neurons in non-mammals. Brain Research Reviews 41: 13-25.

Wang Y, Major DE, & Karten HJ (2004) Morphology and connections of nucleus isthmi pars magnocellularis in chicks (gallus gallus). Journal of Comparative Neurology 469: 275-297.

Wang Y, Luksch H, Brecha NC, & Karten HJ (2006) Columnar projections from the cholinergic nucleus isthmi to the optic tectum in chicks (gallus gallus): a possible substrate for synchronizing tectal channels. Journal Comparative Neurology 494: 7-35.

Wang XJ, & Rinzel J (2003) Oscillatory and bursting properties of neurons. In: Arbib MA (ed) Handbook of brain theory and neural networks. MIT Press, pp. 835-840.

Wolfart J, Debay D, LeMasson G, Destexhe A, & Bal T (2005) Synaptic background activity controls spike transfer from thalamus to cortex. Nature Neuroscience 8: 1760-1767.

Zhan XJ, Cox C, Rinzel J, & Sherman SM (1999) Current clamp and modeling studies of low threshold calcium spikes in cells of the cat's lateral geniculate nucleus. Journal of Neurophysiology 81: 2360-2373.

4 Recurrent antitopographic inhibition mediates competitive stimulus selection in an attention network

Topographically-organized neurons represent multiple stimuli within complex visual scenes and compete for subsequent processing in higher visual centers. The underlying neural mechanisms of this process have long been elusive. We investigate an experimentally-constrained model of a midbrain structure, the optic tectum and the reciprocally connected nucleus isthmi. We show that a recurrent antitopographic inhibition mediates the competitive stimulus selection between distant sensory inputs in this visual pathway. This recurrent antitopographic inhibition is fundamentally different from surround inhibition in that it projects upon all locations of its input layer, except to the locus from which it receives input. At a larger scale, the model reveals how a focal top-down input from a forebrain region, the arcopallial gaze field, biases the competitive stimulus selection via the combined activation of a local excitation and the recurrent antitopographic inhibition. Our findings reveal circuit mechanisms of competitive stimulus selection and should motivate a search for anatomical implementations of these mechanisms in a range of vertebrate attentional systems.

4.1 Introduction

The process of vision as the competitive interaction in a dynamical neural system is poorly understood (Rabinovich et al. 2008). Spike trains from topographically-organized

neurons in early visual pathways represent the occurrence of a stimulus in the retinal image. When multiple visual stimuli appear at different locations (Fig. 4.1), the neural populations compete for dominance and only the winning representations propagate to higher visual centers for further processing (Desimone and Duncan 1995; Kastner and Ungerleider 2000). Such competitive neural interaction is thought to mediate the selection of the most salient stimulus in a given parameter space from complex visual scenes (Itti and Koch 2001; Knudsen 2007).

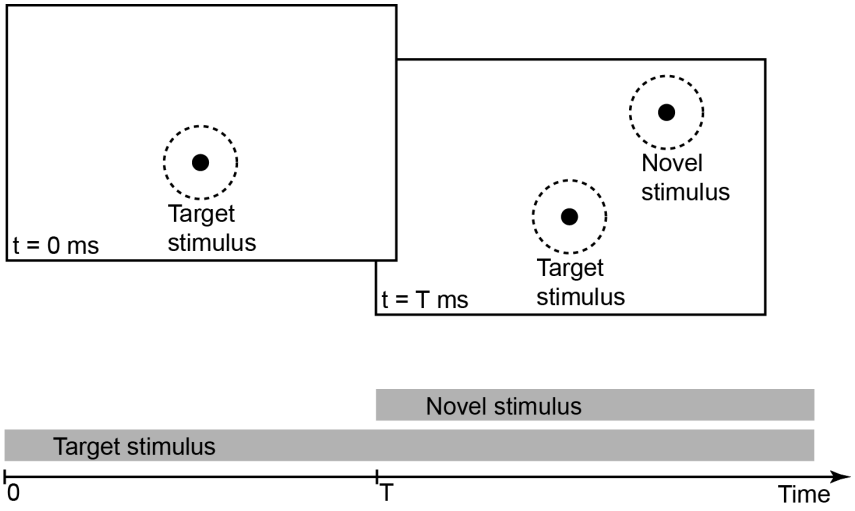

Figure 4.1 Presentation of multiple visual stimuli. The presentation of a target (black dot) at t = 0 ms within a neuron's receptive field (dashed circle), followed by the presentation of a novel stimulus (black dot) at a later time, t = T ms, at a distant location within another neuron's receptive field (dashed circle). The timings of the two stimuli are indicated by the gray bars.

Understanding competitive neural interaction in terms of the neurobiological components and the systems dynamics is a major goal in neuroscience. A prime candidate mechanism for competition among inputs is mutual inhibition (Sum et al. 1999; Mao and Massaquoi 2007), which is present in phenomenological models of shifting attention aimed at selecting salient stimuli from visual scenes (Koch and Ullman 1985; Olshausen et al.

1993; Usher and Niebur 1996; Lee et al. 1999; Reynolds et al. 1999). Here we present a comprehensive microcircuit-level investigation of competitive input selection for time-varying stimuli (Fig. 4.1) within a concrete neural circuit, the superior colliculus, a midbrain structure that receives sensory information and directs the animal's gaze and attention (Stein and Meredith 1993; Hall and Moschovakis 2004; Bisley 2010; Mulckhuyse and Theeuwes 2010).

The superior colliculus represents the locations of stimuli as a topographic map of space and participates in stimulus selection when competing visual stimuli are present (Ignashchenkova et al. 2004; McPeek and Keller 2004; Li and Basso 2005; Müller et al. 2005; Lovejoy and Krauzlis 2010). Similarly, the avian optic tectum (homolog of the superior colliculus in mammals) and its satellite, the nucleus isthmi (homolog of the parabigeminal nucleus in mammals) participate in stimulus competition (Marin et al. 2007; Mysore et al. 2010; Asadollahi et al. 2010), which is further modulated by top-down inputs from a forebrain region (Winkowski and Knudsen 2008). Within the avian isthmotectal circuitry (Wang et al. 2004, 2006) we consider the tectal layer 10 neurons (L10), the parvocellular (Ipc) and two types of magnocellular (Imc) isthmic neurons (Fig. 4.2*a*). In this circuit, the GABAergic Imc projection to the optic tectum displays a heterotopic organization (Wang et al. 2004), i.e., a given Imc neuron does not project back to the locus in the optic tectum from which it receives L10 input, but projects upon all other locations in that layer. In this sense, the Imc projection to the optic tectum can be termed 'antitopographic'.

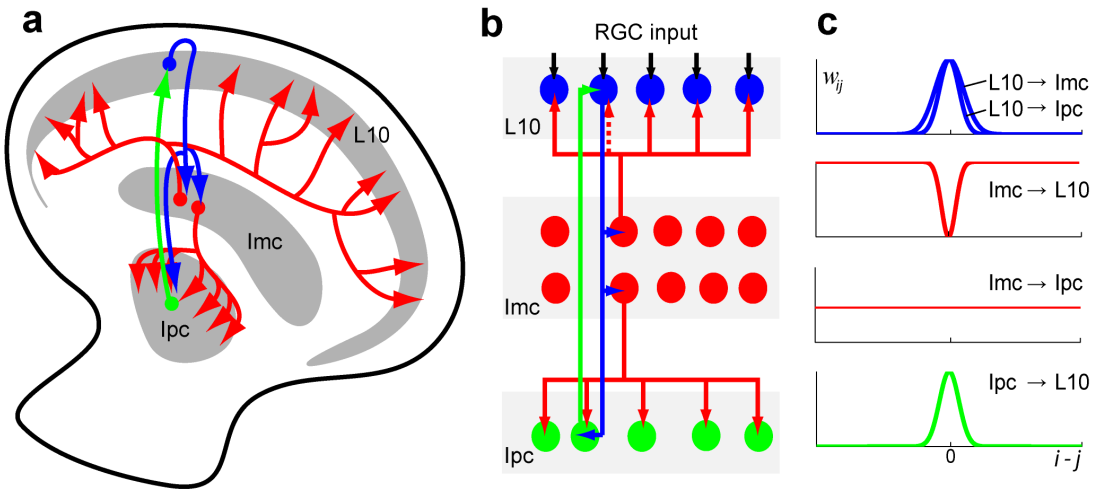

Figure 4.2 Anatomical features of the avian isthmotectal system. *A*, Schematic of the connectivity pattern as seen in a transverse section of the optic tectum and nucleus isthmi. Tectal layer 10 (L10) neurons (blue) receive retinal inputs (not shown) in upper tectal layers and project topographically to the parvocellular (Ipc, green) and magnocellular (Imc, red) isthmic nuclei. The Ipc feedback projection to the optic tectum is topographic, whereas the Imc feedback projection is antitopographic. In addition, Imc neurons mediate a global projection to the Ipc nucleus. *B*, Schematic of the model circuitry consisting of retinal ganglion cell inputs (RGC, black) and L10 (blue), Ipc (green), and two morphological types of Imc (red) neurons. *C*, In the population model, the topographies of the 5 projections are described by Gaussian spatial distributions of the synaptic weights, w_{ij}.

We designed an experimentally-constrained model network of the isthmotectal system (Fig. 4.2*b* and 4.2*c*) and undertook a detailed investigation of the structural and physiological parameter space relevant for stimulus competition. Specifically, we show how the superposition of topographic and antitopographic visual information emerges as a key organizational feature of the isthmotectal system, how the antitopographic projection mediates competitive stimulus selection, and how localized top-down inputs modulate this process. The model reproduces in vivo observations of stimulus competition in owl and pigeon and generates experimentally testable and nontrivial predictions. In addition, a model investigation beyond the experimental constraints

reveals an alternative mechanism of competitive stimulus selection in a network with homogeneous inhibition and strong topographic excitation.

4.2 Methods

The model network consists of 4 linear arrays; L10 and Ipc neurons, and two types of Imc neurons (Fig. 4.2). Each array contains 300 neurons. These neurons respond to somatic current injection with regular spiking, and show spike-rate adaptation and linear frequency-current curves (Shao et al. 2009). Therefore, each neuron in the network is modeled as leaky integrate-and-fire type, including a spike-rate adaptation conductance. In short, the membrane potential V_i of neuron i evolves according to the differential equation, $\tau_i \frac{dV_i}{dt} = E_i - V_i - R_i\left(I_{sra,i} + I_{s,i} + I_{noise,i} - I_{e,i}\right)$. $V_i < V_\theta$ When the membrane potential V_i reaches the threshold $V_{\theta,i}$ it is instantaneously reset to $V_{reset,i}$, which is interpreted as the occurrence of a spike. The basic cellular parameters are the threshold $V_{\theta,i}$, the reset potential $V_{reset,i}$, the resting membrane potential E_i, the membrane input resistance R_i, and the membrane time constant τ_i.

Each neuron receives a spike-rate adaptation current $I_{sra,i}$, a sum of synaptic currents $I_{s,i}$, and a noise current $I_{noise,i}$. The L10 neurons also receive an external excitatory current $I_{e,i}$, which represents the stimulus from the retinal ganglion cells. The spike-rate adaptation current is given by $I_{sra,i} = g_{sra,i}(t)(V_i - E_{sra,i})$ and has the adaptation reversal potential $E_{sra,i}$. The spike-rate adaptation conductance $g_{sra,i}$ increases by an amount

$\Delta g_{sra,i}$ immediately after a spike, i.e., $g_{sra,i}(t^+) \rightarrow g_{sra,i}(t^-) + \Delta g_{sra,i}$, and subsequently decays exponentially with adaptation time constant $\tau_{sra,i}$, i.e., $\tau_{sra,i} \frac{dg_{sra,i}}{dt} = -g_{sra,i}$, until the next spike occurs.

The synaptic current $I_{s,i} = \sum_j g_{ij} P_{ij} w_{ij} (V_i - E_{ij})$ from neuron j to neuron i is proportional to the open probability P_{ij} of the synaptic conductance, where g_{ij} is the maximum synaptic conductance, E_{ij} is the synaptic reversal potential, and w_{ij} is the weight matrix (see below) for the given network. The open probability has the form $P_{ij}(t) = B_{ij} \sum_k \left(\exp(-\frac{t - t_j^k}{\tau_{1,ij}}) - \exp(-\frac{t - t_j^k}{\tau_{2,ij}}) \right)$, where the normalization factor B_{ij} ensures that the peak value of P_{ij} generated by a single spike equals to 1. The time constants $\tau_{1,ij}$ (fall time) and $\tau_{2,ij}$ ($\tau_{1,ij} > \tau_{2,ij}$) determine the time course of synaptic current. The synaptic rise time is given by $\tau_{rise,ij} = \frac{\tau_{1,ij} \tau_{2,ij}}{\tau_{1,ij} - \tau_{2,ij}}$. The variable t_j^k represents the time at which neuron j generates the spike k. A summation is performed over all spikes generated by neuron j.

Unless stated otherwise, parameter values of model neurons and synapses are based on previous studies (Shao et al. 2009), where parameter values were tuned within their experimental constraints until the results of model neuron simulations matched results from in vitro intracellular recordings. All conductances are expressed in terms of an

average membrane conductance, $g_m = 2.78$ nS. For the basic cellular parameters the values are: $V_{\theta,L10} = -39$ mV, $V_{\theta,Ipc} = -40$ mV, $V_{\theta,Imc} = -40$ mV, $V_{reset,L10} = -50$ mV, $V_{reset,Ipc} = -50$ mV, $V_{reset,Imc} = -60$ mV, $E_{L10} = -55$ mV, $E_{Ipc} = -61$ mV, $E_{Imc} = -64$ mV, $R_{L10} = 480$ MΩ, $R_{Ipc} = 135$ MΩ, $R_{Imc} = 240$ MΩ, $\tau_{L10} = 104$ ms, $\tau_{Ipc} = 25$ ms, $\tau_{Imc} = 50$ ms. For the spike-rate adaptation the parameter values are: $\tau_{sra,L10} = 50$ ms, $\tau_{sra,Ips} = 60$ ms, $\tau_{sra,Imc} = 80$ ms, $\Delta g_{sra,L10} = 0.375 g_m$, $\Delta g_{sra,Ipc} = 2.93 g_m$, $\Delta g_{sra,Imc} = 2.25 g_m$, and $E_{sra,L10} = E_{sra,Ipc} = E_{sra,Imc} = -70$ mV. The synaptic time constants for the excitatory synapses are: $\tau_{1,L10\to Ipc} = \tau_{1,L10\to Imc} = 7.6$ ms, $\tau_{2,L10\to Ipc} = \tau_{2,L10\to Imc} = 0.47$ ms, $\tau_{1,Ipc\to L10} = 10.0$ ms, $\tau_{2,Ipc\to L10} = 1.0$ ms (Shao et al. 2009). The synaptic time constants for the Imc projections are $\tau_{1,Imc\to L10/Ipc} = 5.6$ ms and $\tau_{2,Imc\to L10/Ipc} = 0.3$ ms, which are commonly used for GABAergic synapses (Destexhe et al. 1994). Autoradiographic studies indicate that the avian isthmotectal system is rich in GABA-A receptors and that GABA-B receptors are also present (Veenman et al. 1994). The potential contribution of GABA-B receptors to the network dynamics is not considered in this study. The synaptic reversal potentials $E_{L10\to Ipc/Imc} = 0.0$ mV, $E_{Imc\to L10/Ipc} = -80.0$ mV, and $E_{Ipc\to L10} = -5.0$ mV, are consistent with literature values for excitatory and inhibitory synapses (Koch 1999) and with in vivo electrophysiological studies, which suggest that GABA acts as an inhibitory neurotransmitter in this system (Felix et al. 1994). The maximum synaptic conductances for the L10 projections are held fixed, $g_{L10\to Ipc} = 2.1 g_m$ and $g_{L10\to Imc} = 1.5 g_m$. All others are specified in the text.

The anatomical features of the isthmotectal system (Wang et al. 2004, 2006) are incorporated in the weight matrix, w_{ij}. The synaptic conductances of the topographic projections (L10 → Ipc, L10 → Imc, Ipc → L10) are assumed to be described by a Gaussian distribution. For instance, the topographic L10 → Ipc projection from L10 neuron j to Ipc neuron i follows a Gaussian distribution, $w_{ij} = \exp\left(-\frac{(i-j)^2}{2\Delta_{L10\to Ipc}^2}\right)$, where $\Delta_{L10\to Ipc}$ describes the width of the distribution (Fig. 4.2*c*). The other two topographic projections, L10 → Imc and Ipc → L10, are generated in the same manner, however with different width parameters $\Delta_{L10\to Imc}$ and $\Delta_{Ipc\to L10}$, respectively. The chosen widths of the three topographic projections are $\Delta_{L10\to Ipc} = \Delta_{Ipc\to L10} = 11$ and $\Delta_{L10\to Imc} = 16$. The antitopographic Imc → L10 projection is generated according to an inverted Gaussian distribution $w_{ij} = \left(1 - D\exp\left(-\frac{(i-j)^2}{2\Delta_{Imc\to L10}^2}\right)\right)$, which dips near $i = j$. The distribution is specified by two parameters; the width $\Delta_{Imc\to L10}$ and the depth D of the dip. The synaptic conductance from Imc neuron j to L10 neuron i increases with increasing distance, $|i-j|$, between the two locations i and j. When $D = 1$, the antitopographic distribution is strict and there is no feedback from Imc neuron j to L10 neuron i at the same location, $i = j$. The global Imc → Ipc projection is specified by a uniform distribution, $w_{ij} = 1$.

Each neuron receives a noise current, $I_{noise,i}$, which is modeled as uncorrelated white noise, i.e. $\left\langle I_{noise,i}(t) I_{noise,i'}(t') \right\rangle = 2\sigma_i^2 \delta(t-t')\delta_{ii'}$ of standard deviation σ_i. The external

excitatory current input, $I_{e,i} = I_0 H(i-(c-s))H(c+s-i)$, to L10 neuron i represents the stimulus from the retinal ganglion cell. Here I_0 is the input current amplitude, H is a Heaviside step function, c is the location of the input center, and s is the stimulus half width, i.e., $2s+1$ neurons of the L10 type centered at location c receive current injections. The Heaviside step function, H, expresses that the current to L10 neurons is non-zero between neuron $\#(c-s)$ and $\#(c+s)$ and zero elsewhere.

The competition score is defined as the ratio $(r_2 - r_1)/(r_2 + r_1)$, where r_2 and r_1 are the average spike rates of 13 Ipc neurons around the two stimulation centers. The average Ipc spike rates are taken over a time window of 100 ms starting 50 ms after the onset of the novel stimulus. Competition score values can range from -1 (no activity shift) to +1 (complete activity shift). When the two locations display similar activities, the competition score is near zero. Similar activities arise when the two locations do not interact or when the two locations suppress each other.

The top-down input is modeled following anatomical and physiological considerations (Fig. 4.9). The AGF projects strongly and in parallel to the deep layers of the OT and to nuclei of the brainstem, including the n. isthmi (Knudsen et al. 1995). In the AGF sensory space is organized in a clustered representation in which neighboring neurons encode a similar location, but neighboring groups of neurons encode different, unpredictable locations (Cohen and Knudsen 1995). AGF microstimulation within a cluster tuned to a certain location in sensory space (i) increases the responsiveness of OT neurons tuned to the same location and (ii) decreases the responsiveness of OT neurons tuned to all other

locations (Winkowski and Knudsen 2006, 2007, 2008). At present, there is no compelling explanation for why clustered organizations exist (Cohen and Knudsen 1999). The two AGF inputs in our model (thick arrows, Fig. 4.9*a*) represent two different locations in sensory space.

To compare the simulated responses with recordings from deep tectal layers (Winkowski and Knudsen 2008), we introduce an additional read-out neuron, which is modeled as a Hill's function $\frac{ar^n}{r^n + b^n}$ (Fig. 4.9*c*). Here r is the input firing rate from presynaptic neurons, a is the saturation firing rate, b is the input firing rate when the output reaches the half of its saturation value, and n describes the steepness of the response curve.

4.3 Results

4.3.1 Structure of the isthmotectal model network

To investigate the dynamics of stimulus competition in the isthmotectal system, we represent the available anatomical (Wang et al. 2004, 2006) and physiological (Shao et al. 2009) information about the avian isthmotectal circuit (Fig. 4.2*a*) in a model network (see METHODS) consisting of 4 interacting populations of spiking model neurons (Fig. 4.2*b*) of the leaky integrate-and-fire type, including a spike-rate adaptation conductance. Tectal L10 neurons receive simulated retinal representations of visual stimuli, which are the sole inputs into this topographically-organized model network. The width of an axonal projection is expected to be an important structural feature of any system with competitive interaction. For the feedforward pathway, we describe the lateral spread of

individual axons in the L10 → Ipc and L10 → Imc excitatory projections by Gaussian distributions of their synaptic weights (Fig. 4.2*c*). The global Imc → Ipc inhibitory projection is described by a uniform distribution of synaptic weights. For the feedback pathway, we represent the Ipc → L10 excitatory projection by a Gaussian distribution of its synaptic weights. Imc neurons, in contrast, project diffusely upon L10 neurons, but little to the locus from which they receive input (Wang et al. 2004) This antitopographic GABAergic Imc → L10 feedback projection is described by an inverted Gaussian distribution, where the strength of synaptic weights dips at its center, corresponding to the location from which the Imc neuron receives its input. Thus, an Imc model neuron provides weak inhibition on the L10 neurons corresponding to the same location and stronger inhibition on distal L10 neurons. In summary, the experimentally-constrained isthmotectal model system consists of a specific combination of excitatory topographic, and inhibitory antitopographic and global projections (Fig. 4.2).

4.3.2 Competitive bottom-up selection of novel stimuli

The network response to two sequentially-presented stimuli with temporal overlap reveals the competitive nature of the isthmotectal network (Fig. 4.3*a*). The isolated target stimulus elicits regular and correlated spiking in L10 neurons, which in turn generates rhythmic bursting in a group of Ipc and Imc neurons corresponding to the target location. Such rhythmic Ipc bursting has been recorded in pigeon Ipc neurons in response to visual stimulation (Marin et al. 2005, 2007).

The additional and delayed presentation of a novel stimulus of equal or larger amplitude (Fig. 4.3*a*, 4.4) at a distant location has two effects on the population activity. The retinal input to L10 neurons at the novel location overcomes the inhibitory input from the Imc neurons at the distal target location. Approximately 50 ms after onset of the novel stimulus, the L10 neurons at the novel location start to spike, which in turn triggers spikes in the corresponding Ipc and Imc neurons. The delay has three causes: the L10 neuron membrane time constant ($\tau_{L10} = 104$ ms), the hyperpolarized level of the L10 membrane potential at the novel location at the onset of the novel stimulus, and the small size of the depolarizing current, which is the difference of the excitatory current (novel stimulus) and the inhibitory current (from the Imc target location). The Imc activity at the novel location provides inhibitory current in L10 neurons at the target location. This new inhibitory current together with the existing adaptation current overcomes the excitatory input current in the L10 target neurons, which ends spiking in these and the corresponding Ipc and Imc neurons at the target location. A complete shift in activity from the target to the novel location has occurred, even though stimulation at the target site continues for the entire duration of novel stimulus presentation.

Apart from the functionally significant shift in activity to novel stimuli of equal or larger amplitude (Fig. 4.3a), the population model (Fig. 4.2) reproduces four important in vivo observations previously recorded in the avian isthmotectal system (Marin et al., 2005, 2007): (i) Ipc neurons respond with rhythmic bursting to visual stimulation, (ii) the novel stimulus can be far for the shift in activity to occur, (iii) the delay in shift measured from the onset of the novel stimulus is variable between 35 and 100 ms, and (iv) Imc neurons

fire synchronously and at regular intervals. The retrodiction of these four in vivo observations indicates that the population model captures key anatomical and physiological elements of the avian isthmotectal pathway.

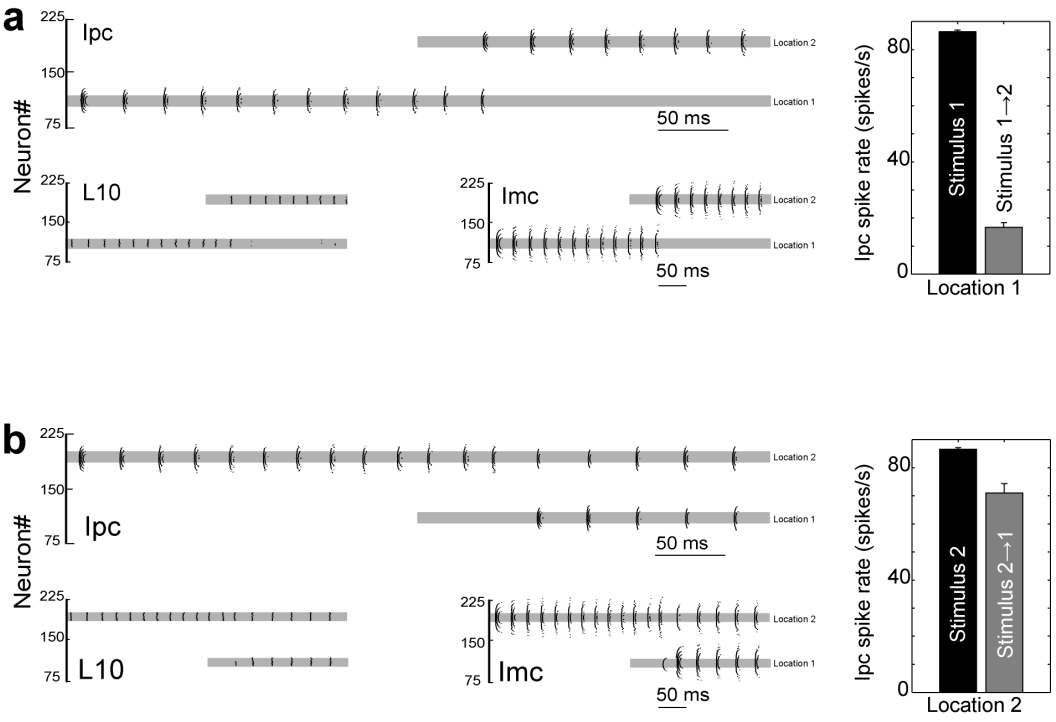

Figure 4.3 Competitive neural interaction between two retinal inputs in a population model of the avian isthmotectal system. *A*, Raster plots of spiking activity in L10, Ipc, and Imc model neurons in response to the presentation of a target stimulus followed by the presentation of a novel stimulus of slightly larger amplitude. The target stimulus consists of an input current of 0.4 nA starting at t = 0 ms into 15 L10 neurons centered on neuron #110 (location 1). The novel stimulus consists of an input current of 0.42 nA starting at t = 250 ms into 15 L10 neurons centered on neuron #191 (location 2). The location, width and timing of the stimuli into L10 neurons are indicated by the gray bar in the L10 raster plots. No current is injected into Ipc and Imc neurons, but, for comparison, the gray bar is also reproduced in the Ipc and Imc raster plots. The synaptic strengths are $g_{Ipc\to L10} = 0.01 g_m$, $g_{Imc\to Ipc} = 0.12 g_m$, and $g_{Imc\to L10} = 0.24 g_m$. The depth $D_{Imc\to L10}$ and the width $\Delta_{Imc\to L10}$ of the antitopographic Imc → L10 projection are 0.6 and 8, respectively. The input current has a noise of $\sigma = 0.05$ nA. Inset: Average spike rate of 13 Ipc neurons (5 trials) centered at neuron #110 (location 1) during isolated target (0.4 nA) presentation (time window 0 to 250 ms) and during concurrent target (0.4 nA) and novel (0.42 nA)

stimulus presentation (time window 250 to 500 ms). *B*, Raster plots of spiking activity in response to the presentation of a target stimulus (0.42 nA) followed by the presentation of a novel stimulus (0.4 nA) of slightly smaller amplitude. Other parameters are the same as in *A*. Inset: Average spike rate of 13 Ipc neurons (5 trials) centered at neuron #191 (location 2) during isolated target (0.42 nA) presentation and during concurrent target (0.42 nA) and novel (0.4 nA) stimulus presentation.

When the novel stimulus is of smaller amplitude than the target stimulus, no shift in activity occurs (Fig. 4.3*b*, 4.4). A small difference in input current causes no significant differences in the responses at the two locations when each stimulus is presented in isolation (Fig. 4.3*a* and 4.3*b*). Yet, for sequential stimulation with temporal overlap the response to a weaker novel stimulus (Fig. 4.3*b*) is qualitatively different from the response to a stronger novel stimulus (Fig. 4.3*a*) described above. The weaker novel stimulus overcomes the inhibitory current from the target Imc neurons and causes L10 spiking. Nevertheless, the corresponding Imc spike rate at the novel location does not generate sufficient inhibitory current in the L10 target neuron. The excitatory current in the target L10 neuron remains larger than the sum of the inhibitory and the adaptation current. As a result, L10 and thus Ipc neurons at target and novel location spike, however at a reduced rate.

This model result reproduces in vivo recordings from pigeon Ipc neurons, which demonstrated that a novel visual stimulus in a superior receptive field strongly suppresses target responses in an inferior receptive field, but showed only little suppression vice versa (Marin et al. 2007). We thus demonstrate that even though in the population model all locations have equal status, the observed response asymmetry can be implemented by an asymmetry in the retinal representation of the visual stimuli. When the amplitude of

the novel stimulus is varied systematically while the target stimulus amplitude remains fixed, the transition from no shift to complete shift occurs within a narrow range of novel stimulus strength below the value of the target stimulus strength (Fig. 4.4); a model prediction that is accessible for in vivo tests.

The model further predicts that in this range of novel stimulus strength the neural activities synchronize at the two locations (Fig. 4.3*b*). The synchrony is independent of the onset timing of the novel stimulus and is robust to noise in the system. Specifically, whether the activities are synchronous (for large inhibition) or antisynchronous (for small inhibition) depends on the strength of the recurrent antitopographic inhibition. The dynamics of synchrony between coupled neurons is complex (Lewis and Rinzel 2003). In the isthmotectal system synchrony emerges from the reciprocal inhibition (Imc → L10) between groups of neurons at the target and novel location.

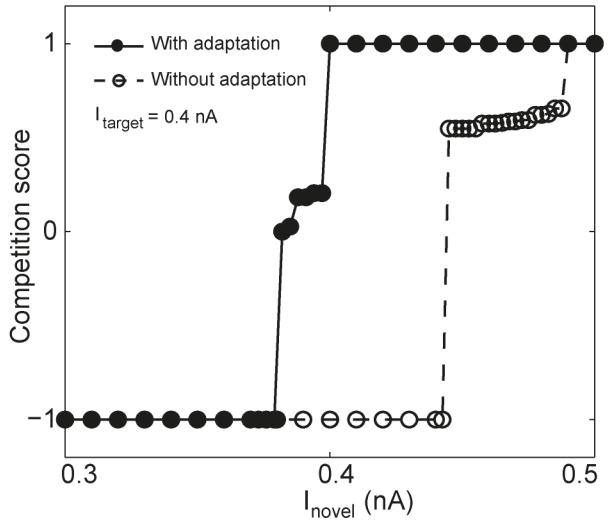

Figure 4.4 Change of competitive neural interaction between target and novel stimulus with varying novel stimulus amplitude. The competition score (see METHODS) is shown as a function of the novel stimulus amplitude. All parameters are the same as in Figure 3. The transition happens within a narrow range of novel stimulus strength around the value

of the target stimulus strength. Without spike-rate adaptation, the transition range shifts to larger values of novel stimulus strength.

4.3.3 Competitive bottom-up selection of stimuli in static visual scenes

To gain insight into the system response to static visual scenes, we investigated the model responses to two *simultaneously* presented stimuli, a target and a distant competitor stimulus. When the competitor is weaker than the target stimulus, the Imc activity at the target location generates a strong inhibitory current in the L10 neurons at the competitor location. The competitor-induced excitatory current in the L10 neurons is too small to trigger spikes. In contrast, when the competitor is stronger than the target, L10 neurons at the competitor location spike. In this case L10 neurons at the target locations are inhibited, which prevents them from spiking. The model generates three nontrivial predictions for simultaneous stimulus presentation (Fig. 4.5*a*). First, when a target and a distant competitor stimulus of different strength are presented simultaneously, the isthmotectal model network selects in a winner-take-all manner the strongest stimulus in this static visual scene. Second, for fixed target strength and varying competitor strength, the transition occurs around the value of the target strength. Third, the transition as a function of competitor strength can be gradual or switch-like, as the slope of the transition depends on the strength of the recurrent antitopographic inhibition. In the limit of zero recurrent antitopographic inhibition, no competition occurs. When this inhibition is weak the transition is gradual, when the recurrent antitopographic inhibition is strong the transition is switch-like. Interestingly, transitions around the target strength with a distribution of slopes have been observed in neurons of the isthmotectal system of barn owls in response to visual stimulation with a target and a competitor (Mysore et al. 2010,

Asadollahi et al. 2010). This in turn suggests a distribution of the recurrent antitopographic inhibition strength.

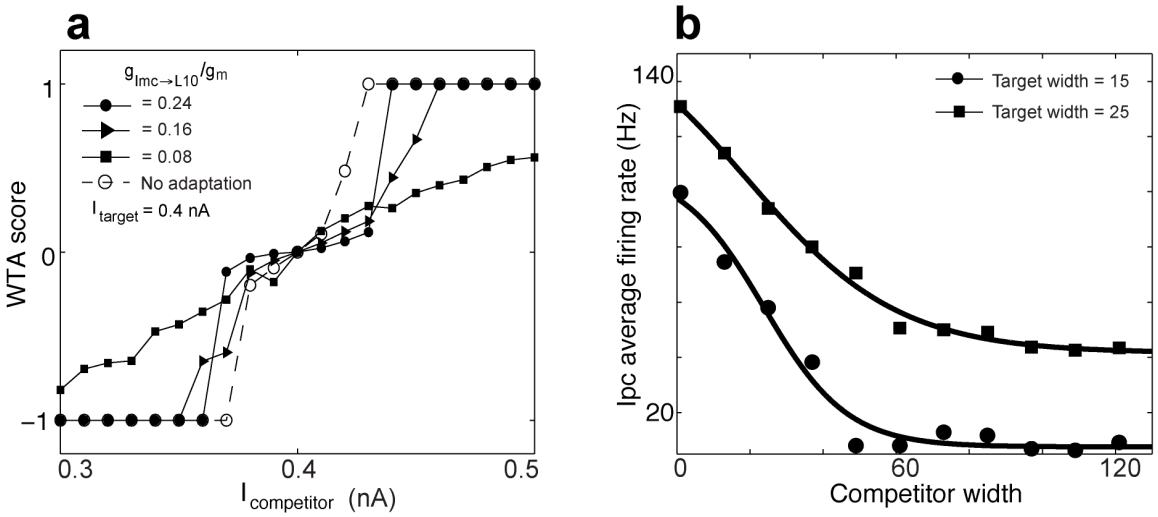

Figure 4.5 Competitive neural interaction between a target and a simultaneously-presented distant competitor. *a*, The target stimulus strength is kept fixed at 0.4 nA, the competitor strength is varied, and the results are expressed in terms of a winner-take-all (WTA) score, which is defined as the ratio $(r_2 - r_1)/(r_2 + r_1)$. Here r_2 and r_1 are the average spike rates of 13 Ipc neurons around the two stimulation centers. The average Ipc spike rates are taken over a time window of 450 ms starting 50 ms after the onset of the two stimuli. Other parameters are the same as in Figure 3. *b*, Ipc average firing rate at the target location (averaged over 3 Ipc neurons at the target center) as a function of competitor width for two different target widths. The target and competitor stimuli are of the same strength (0.4 nA). Network parameters are the same as in Fig. 4.3. The simulated results are fitted to a sigmoidal function (solid line).

When the sizes of the target and competitor stimulus are varied, the isthmotectal model network does not select the largest stimulus in a typical winner-take-all manner; rather the Ipc response at the target location continues to represent information about the target stimulus width (Fig. 4.5*b*). We consider two target widths and vary the width of the competitor stimulus. With increasing competitor width, the Ipc target response decreases until it reaches a steady state. Importantly, the steady-state value increases with target

width. Two circuit mechanisms cause this deviation from a winner-take-all behavior. First, with increasing competitor width the inhibitory synaptic current in L10 neurons saturates as the membrane potential hyperpolarizes towards the synaptic reversal potential. Second, the number of activated L10 neurons increases with increasing target width. Because of the width of the L10 → Ipc projection (Fig. 4.2*c*), this in turn increases the excitatory input to an Ipc neuron at the target location. Thus the Ipc target response increases with target width (Fig. 4.5*b*). This model prediction is consistent with recorded responses in owl Ipc in response to looming dots of varying final sizes (Asadollahi et al. 2010).

4.3.4 Recurrent antitopographic inhibition

An intriguing structural feature of the isthmotectal pathway is the combination of global feedforward (Imc → Ipc) and recurrent antitopographic (Imc → L10) inhibition mediated by Imc neurons (Wang et al. 2004), which determines complex responses of this dynamical system (Caudill et al. 2009). Pharmacological inactivation of the Imc demonstrated the essential role of Imc neurons in mediating the shift of Ipc activity to novel stimuli (Marin et al. 2007). This experiment, however, could not determine the individual roles of the global (Imc → Ipc) and antitopographic (Imc → L10) inhibition in the competitive stimulus selection. To address this question, we scanned the model parameter space for varying synaptic strengths, $g_{Imc \to Ipc}$ and $g_{Imc \to L10}$, of the two Imc projections and displayed the simulated response to sequential stimulation (Fig. 4.3*a*) of equal strength in terms of a competition score (see METHODS). This score is based on the Ipc activity within a time window after the onset of the novel stimulus. The Ipc

response was chosen as a measure of the simulation results, because the Ipc activity gates the processing in the tecto-rotundal visual pathway (Marin et al. 2007).

When both inhibitory projections are weak, neurons at the target and novel stimulus location respond largely independently to their local inputs (Fig. 4.6*a*). This model result reproduces the in vivo observation that Imc neurons are required for the shift in activity to happen (Marin et al. 2007). For increased strength of the feedforward inhibition, the global Imc → Ipc projection does not contribute to competitive interaction, but rather merely regulates the level of Ipc activity. With increasing strength of the antitopographic Imc → L10 feedback projection, however, stimulus competition sets in. The Imc activity at the novel location generates sufficient inhibitory current in the L10 target neurons, such that the sum of the inhibitory and the adaptation current overcomes the excitatory current. The L10 target neurons cease to spike, i.e., the Ipc competition score is $+1$. Further increase of the Imc → L10 projection strength mediates large inhibitory currents at both locations and dynamically reduces the L10 spike rate. Depending on the relative strength of excitation and antitopographic inhibition, either L10 neurons at the novel location do not spike (competition score equals -1) or L10 neurons spike at both locations (competition score near 0). In conclusion, given the weak Ipc → L10 excitatory feedback, the Imc → L10 antitopographic inhibition at intermediate strength is essential for the isthmotectal selection of novel stimuli. The experimental test of this model prediction requires the selective block of the Imc → L10 pathway within the avian isthmotectal system.

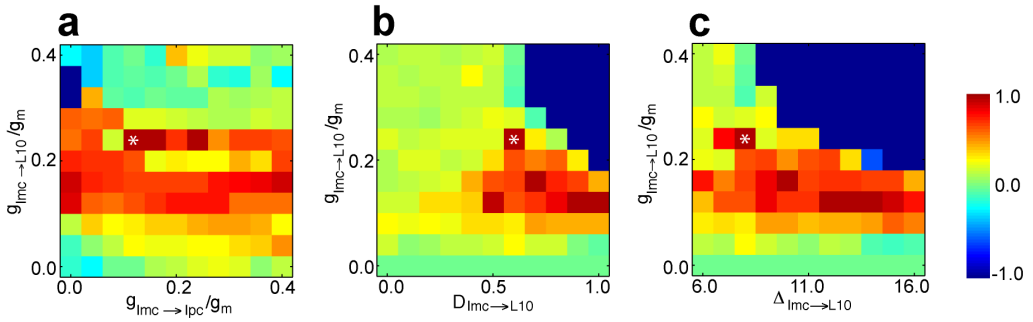

Figure 4.6 Recurrent antitopographic inhibition mediates competitive stimulus selection between two distant sensory inputs of equal strength. Parameter-dependence of novelty detection in the isthmotectal model network is expressed by the competition score as a function of A, global inhibition $g_{Imc \to Ipc} / g_m$ and recurrent antitopographic inhibition $g_{Imc \to L10} / g_m$; B, the strength $g_{Imc \to L10} / g_m$ and depth $D_{Imc \to L10}$ of the recurrent antitopographic inhibition; C, the strength $g_{Imc \to L10} / g_m$ and width $\Delta_{Imc \to L10}$ of the recurrent antitopographic inhibition. The competition score is color coded representing -1 (blue, no shift in activity), 0 (green, similar spike rates at both locations) to 1 (red, complete shift in activity to the novel location). The novel stimulus starts 250 ms after the onset of the target stimulus. Both stimuli are of the same amplitude ($I_{target} = I_{novel} = 0.4$ nA). Panels A to C show three cross sections through the multidimensional parameter space. The cross sections intersect at the point indicated by the white asterisk, which is also the parameter set chosen for Fig. 4.3 and 4.9. No noise is included in the simulations. All other parameters are the same as in Fig. 4.3.

The importance of the antitopographic inhibitory Imc → L10 projection within the isthmotectal system raises the question to what extent the two structural parameters, the depth $D_{Imc \to L10}$ and the width $\Delta_{Imc \to L10}$ of the dip in this feedback projection, influence the competitive interaction (Fig. 4.6*b* and 4.6*c*). When the depth or width of the dip is small, an Imc neuron exerts a strong inhibition on the L10 neuron from which it receives input. Thus, the L10 and Imc activity at the target location is too small for the spike-rate adaptation current to reach a significant level. Similarly, Imc activity at the target location mediates only a small inhibitory current in L10 neurons at the novel location. As a result, when the novel stimulus occurs, neurons at both locations fire at a reduced but

similar rate (competition score near 0). With increasing depth or width parameter, the inhibition of the L10 neurons at the target location is reduced. This leads to an increased spike rate with a concurrent increase in the spike-rate adaptation current at the target location and an increased inhibitory current at distal locations. When a novel stimulus occurs at a distant location, the corresponding L10 and Imc neurons start spiking. Consequently, the L10 neurons at the target location cease spiking as the sum of the currents from the continuing adaptation and the new antitopographic inhibition cancels the excitatory stimulus current (competition score equals $+1$). Further increase of the depth (width) of the antitopographic inhibition, $g_{Imc \to L10}$, decreases the inhibition of the L10 neurons at the target location, thus increasing the local spike rate. For large strength of the antitopographic Imc → L10 feedback projection, the Imc-mediated inhibitory current at distal locations prevents L10 neurons at these distant locations to spike in response to novel stimuli. As a result, there is no shift in activity in this parameter range (competition score equals -1). Consequently, a large depth or width narrows the range of inhibitory feedback strengths for which a shift in activity occurs.

Motivated by in vitro studies of the isthmotectal system (Shao et al. 2009), this model investigation assumed a weak Ipc excitatory feedback onto L10 neurons. With increasing strength of the Ipc → L10 excitatory feedback an appropriate level of recurrent inhibition is required to stabilize the system and for novelty shifts to occur (Fig. 4.7).

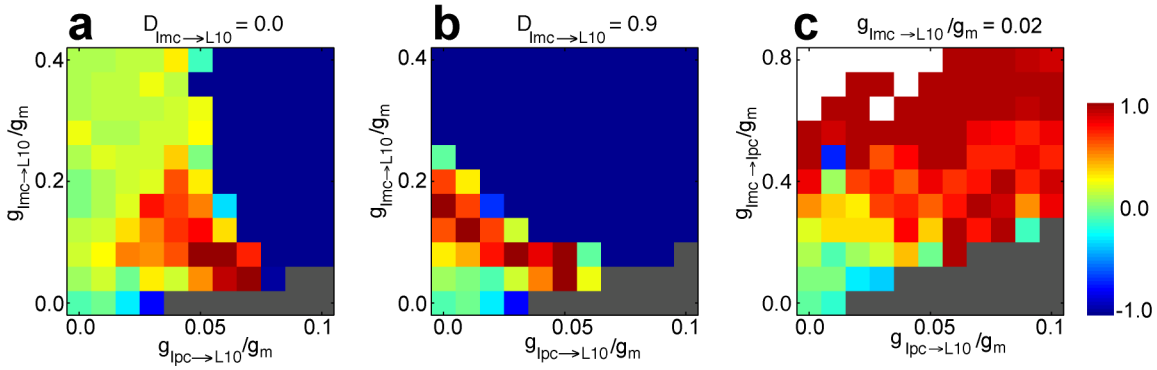

Figure 4.7 A new role arises for the topographic Ipc → L10 excitatory feedback when the inhibitory Imc projections are more homogeneous. The parameter-dependence of novelty detection in these isthmotectal model networks is expressed by the competition score (color code) as a function of *a*, the strength $g_{Imc\to L10}/g_m$ of a global Imc → L10 inhibition ($D_{Imc\to L10}=0.0$) and the topographic excitatory feedback $g_{Ipc\to L10}/g_m$, *b*, the strength $g_{Imc\to L10}/g_m$ of an antitopographic Imc → L10 inhibition ($D_{Imc\to L10}=0.9$) and the topographic excitatory feedback $g_{Ipc\to L10}/g_m$, *c*, the strength $g_{Imc\to Ipc}/g_m$ of a global Imc → Ipc inhibition and the topographic excitatory feedback $g_{Ipc\to L10}/g_m$. The color code and stimulus settings are as in Figure 6. Gray represents diverging activity; defined as an average firing rate of the center Ipc neuron above 1000 Hz. White represents vanishing activity.

A new role arises for the topographic Ipc → L10 excitatory feedback when the inhibitory Imc → L10 projection is homogeneous ($D_{Imc\to L10}=0$), i.e., no dip in the inhibitory projection. In this case, the inhibition of L10 neurons at the target location reduces spiking thus limiting the spike-rate adaptation current. The local inhibitory feedback thus prevents novelty shifts to occur for stimuli of equal strength. However, with increasing local Ipc → L10 excitatory feedback, the local inhibition can be overcome. This increases the spike rate and the concurrent spike-rate adaptation current, which promotes the occurrence of activity shifts in response to novel stimuli at distant locations (Fig. 4.7*a*). Interestingly, in this case competitive stimulus selection occurs only within a narrow parameter range of inhibition and excitation strength. When the inhibitory Imc → L10

projection is antitopographic ($D_{Imc \to L10} = 0.9$), the neural activity at the target location is sufficiently high, even without Ipc → L10 excitatory feedback, to allow for activity shifts in response to novel stimuli (Fig. 4.7*b*). In general, with increasing strength of the Ipc → L10 feedback, the Ipc activity plays a larger role in L10 responses and thus the nature of the inhibitory global Imc → Ipc projection changes from feedforward (Imc → Ipc) to feedback (Imc → Ipc → L10 → Imc). To illustrate this point, we consider a model with excitatory topographic Ipc → L10 projection and inhibitory homogenous Imc → Ipc projection, but with a weak Imc → L10 projection. In this case, competitive stimulus selection is possible, but requires strong excitation and inhibition (Fig. 4.7*c*).

In conclusion, these parameter scans show that stimulus selection in the avian isthmotectal system requires a careful balance of the physiological and anatomical parameters in the antitopographic Imc → L10 feedback projection.

4.3.5 Adaptation

Isthmotectal neuron firing rates adapt to somatic current injection (Shao et al. 2009). To quantify the role of adaptation in competitive stimulus selection in the avian isthmotectal system, we analyzed neural competition for varying amplitude of spike-rate adaptation, $\Delta g_{sra,L10}$ and $\Delta g_{sra,Imc}$, for L10 and Imc neurons, respectively. Because of their weak synaptic strength on L10 neurons (Shao et al. 2009), the role of Ipc spike-rate adaptation was not considered. For small values of spike-rate adaptation, $\Delta g_{sra,L10}$ and $\Delta g_{sra,Imc}$, the L10 and Imc spike frequency at the target location is high. As a result, the Imc-mediated inhibitory current in L10 neurons prevents the L10 neurons at the novel location from

spiking in response to the novel stimulus. Consequently, no shift in activity occurs, i.e., the Ipc competition score is -1 (Fig. 4.8). However, for intermediate values of spike-rate adaptation, $\Delta g_{sra,L10}$ and $\Delta g_{sra,Imc}$, the rate of L10 and Imc spiking at the target location is reduced, thus reducing the inhibitory synaptic current in L10 neurons at the novel location. The novel excitatory input to L10 neurons overcomes the inhibition. Consequently, the L10 and thus the Imc neurons at the novel location start to spike. The resulting Imc-mediated inhibitory current (together with the adaptation current) at the target L10 neurons reduce further the L10 response to the target excitatory input. As a result, Ipc neurons spike at both, the target and the novel location, which leads to a competition score near 0. With further increase of the spike-rate adaptation, the sum of the inhibitory synaptic current from the antitopographic projection together with the increased adaptation current in L10 neurons overcomes the target excitatory current. The L10 target neurons cease spiking, i.e., a shift in activity occurs and the Ipc competition score is near $+1$. In conclusion, spike-rate adaptation facilitates the isthmotectal selection of novel stimuli.

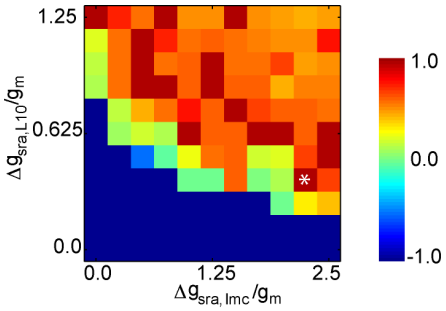

Figure 4.8 Spike-rate adaptation facilitates the selection of novel stimuli. Novelty detection is expressed by the competition score as a function of spike-rate adaptation $\Delta g_{sra,Imc}/g_m$ and $\Delta g_{sra,L10}/g_m$. The competition score is color coded representing -1 (blue, no shift in activity), 0 (green, similar spike rates at both locations) to 1 (red, complete shift in activity to the novel location). The novel stimulus starts 250 ms after the onset of

the target stimulus. Both stimuli are of the same amplitude ($I_{target} = I_{novel} = 0.4$ nA). The white asterisk indicates the parameter set chosen for Fig. 4.3 and 4.9. No noise is included in the simulations. All other parameters are the same as in Fig. 4.3.

This facilitation is documented further, when the amplitude of the novel stimulus is varied systematically while the target stimulus amplitude remains fixed (Fig. 4.4). Without spike-rate adaptation the novel stimulus has to be larger than the target stimulus for activity shifts to occur. In contrast, competition between simultaneously presented target and competitor stimuli is not significantly influenced by spike-rate adaptation (Fig. 4.5*a*).

4.3.6 Competitive interaction between top-down and sensory inputs

Electrical microstimulation in the avian arcopallial gaze field ([AGF], putative homolog of the primate frontal eye field region) increases the sensitivity of sensory responses for deep tectal neurons with a receptive field aligned to the AGF stimulation site, but decreases the gain of deep tectal neurons representing stimuli at other locations (Winkowski and Knudsen 2008). The AGF projects to both the optic tectum and the isthmic nuclei (Knudsen et al. 1995), suggesting that the mechanisms for the top-down control of tectal gain and sensitivity emerge from the interaction of the AGF and the sensory input within the isthmotectal circuit. The isthmic output, e.g., Ipc spiking, then modulates the responses of postsynaptic deep tectal neurons.

To elucidate these mechanisms, we simulated the interaction of a sensory input (from retinal ganglion cells) and a top-down input (from AGF) in the isthmotectal model

network for varying stimulus strength (Fig. 4.9*a*). Given the spatially broad tuning curves of sensory pathways, we assume that, at the level of the tectum, stimulus strength is usefully represented by the number of activated L10 neurons. We refer to the latter as the stimulus width.

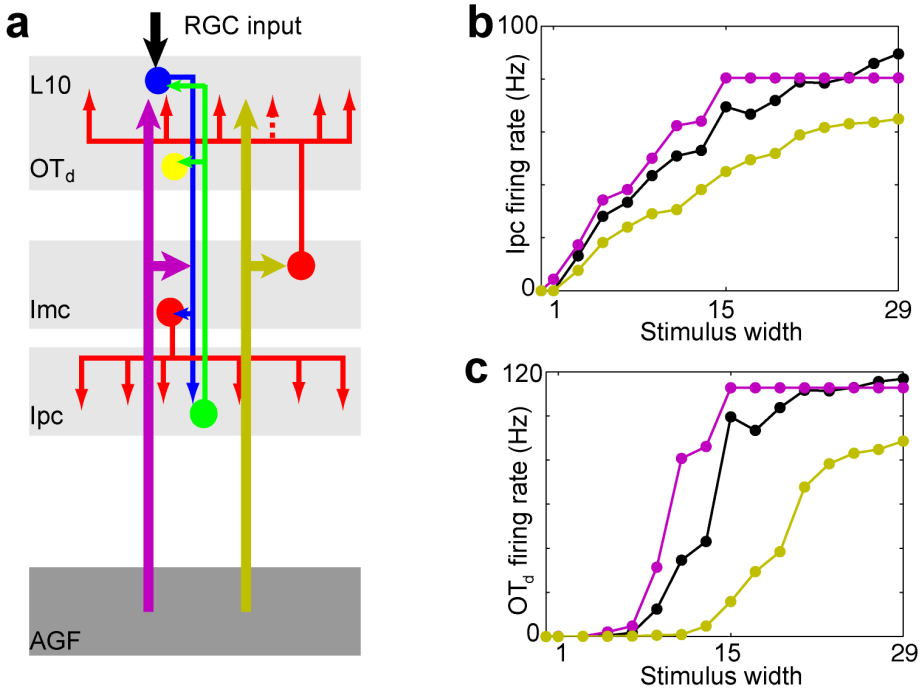

Figure 4.9 Competitive interaction within the isthmotectal system between a sensory input and a top-down input. *A*, Schematic of the isthmotectal model circuitry consisting of retinal ganglion cell inputs (RGC, black) and L10 (blue), Ipc (green), Imc (red) neurons and two external inputs from the AGF onto L10 neurons and the Imc neurons with projections to L10. The two AGF inputs (thick arrows) represent two different locations in sensory space. A representative deep tectal model neuron is assumed to receive inputs from a group of Ipc neurons. *B*, Average firing rate of the 13 central Ipc neurons (time window 250 to 800 ms) as a function of the stimulus width for three different situations of top-down modulation: no AGF input (black), aligned AGF input (purple), non-aligned AGF input (yellow). The external currents are $I_{target} = 0.2$ nA, $I_{AGF \to L10} = 0.1$ nA and $I_{AGF \to Imc} = 0.8$ nA. The AGF input consists of two excitatory current inputs in 13 L10 neurons and 13 Imc neurons. *C*, Average firing rate of the deep tectal model neuron ($n = 8$, $a = 120$ Hz, $b = 57$ Hz) as a function of the stimulus width for the three different situations of top-down modulation (colors as in *B*).

The isthmic responses to sensory stimuli of varying width emerge from the recurrent interaction of excitatory (L10) and inhibitory (Imc) neurons. In response to a sensory stimulus alone, the number of activated L10 neurons increases with increasing stimulus width and thus the average L10 firing rate increases. This in turn activates more Imc neurons and, because of the recurrent antitopographic inhibition, the average L10 firing rate of a group of neurons around the stimulation center saturates with increasing stimulus strength. Since Ipc neuron activity largely follows their L10 input (Fig. 4.3), the Ipc stimulus response function displays a qualitatively-similar sigmoidal form (Fig. 4.9*b*).

Guided by the available anatomical information (Knudsen et al. 1995), we represent the AGF control with two excitatory current inputs in a group of L10 and Imc neurons (Fig. 4.9a). When the sensory stimulus and the AGF control are aligned, the L10 response to the sensory input is increased because of the additional excitation from the AGF. Because of the antitopographic feedback of Imc neurons, the AGF excitation of Imc neurons has little effect on the local L10 responses. In contrast, when the sensory stimulus and the AGF control are nonaligned, the AGF input to distant Imc (and L10) neurons activates an antitopographic inhibition, which reduces the L10 response to the sensory stimulus. Consequently, compared to the control case, the Ipc stimulus response function is slightly shifted to smaller stimulus width for the aligned case, and overall reduced for the nonaligned case (Fig. 4.9*b*).

With these results at hand, we evaluated the stimulus-width response function of a deep tectal model neuron that is assumed to receive inputs from a group of Ipc neurons. A

single-neuron rate model (see METHODS) with the simulated Ipc activity as inputs qualitatively reproduces (Fig. 4.9*c*) the stimulus-width response function of deep tectal neurons in owls for the aligned and non-aligned top-down control scenarios (Winkowski and Knudsen 2008) and thereby indicates two distinct mechanisms for the top-down control of neural sensitivity and gain, respectively. Aligned AGF input increases the sensitivity of the deep tectal neuron via the excitation of L10 neurons at the sensory stimulation site. Non-aligned AGF input decreases the gain of the deep tectal neuron via the excitation of distant Imc neurons, which then provide antitopographic inhibition of L10 neurons at the sensory stimulation site. The top-down control of the L10 neurons isthen communicated from L10 to Ipc to the deep tectal neurons.

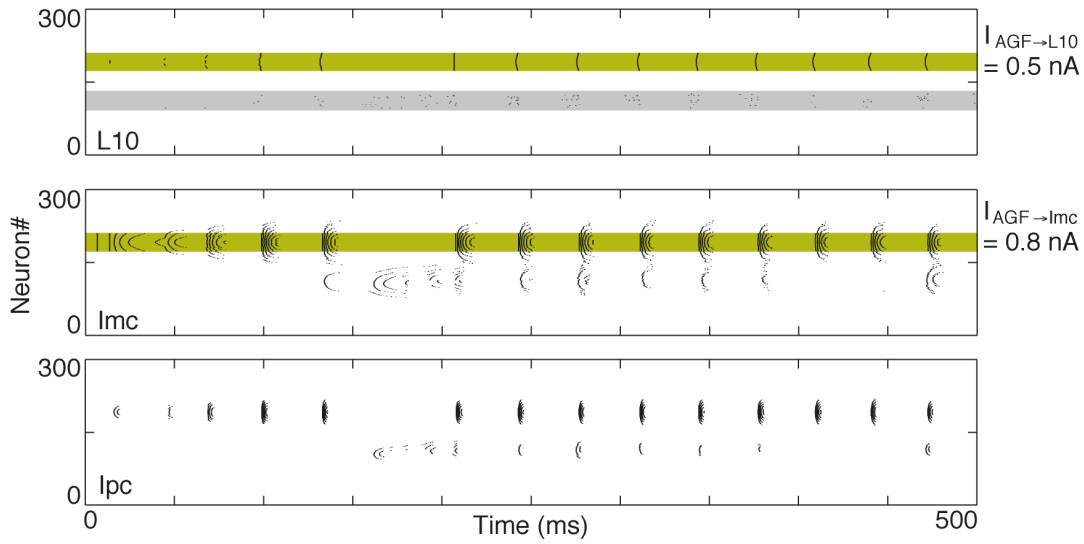

Figure 4.10 Ipc and Imc responses to a sensory input synchronize to distant isthmic activity induced by a top-down AGF input. A target stimulus consisting of uncorrelated Poisson current pulses ($I_{0,i}(t) = a_s / \tau_s t \exp(-t/\tau_s)$, $f = 100$ Hz, $a_s = 0.6$ nA, $\tau_s = 5.6$ ms) delivered to 25 L10 neurons (centered on neuron # 110; indicated by the gray bar in the L10 raster plots) triggers irregular spiking in this group of L10 neurons. The AGF input consists of continuous current inputs in 37 L10 neurons (0.5 nA) and 37 Imc

neurons (0.8 nA) centered on neuron # 191 (green bars in the L10 and Imc raster plots). The cellular and synaptic parameters of the network are the same as in Fig. 4.3 and 4.9.

In addition to its modulatory effect on steady-state firing rate, top-down inputs can also modulate temporal aspects of neural responses to sensory inputs (Reynolds et al. 2000; Fries et al. 2001; Mitchell et al. 2007). To evaluate the dynamics of competitive interaction between a sensory input and a nonaligned top-down input in the isthmotectal system, we stimulate a group of L10 target neurons with uncorrelated Poisson current pulses and mimic the top-down input with constant current input to a group of distant L10 and Imc neurons. When the nonaligned AGF input is sufficiently strong, Ipc and Imc responses at the target location become periodic and synchronize to the oscillatory bursts at the distant location, which is activated by the nonaligned top-down AGF input (Fig. 4.10). The synchrony is mediated by the Imc (nonaligned) → L10 (target) inhibitory projection, which imposes a temporal structure onto the otherwise irregularly firing L10 neurons.

4.4 Discussion

4.4.1 Mechanisms of competitive stimulus selection

Attention is a crucial component of sensory processing, yet, the circuit mechanisms that mediate attentional stimulus selection have remained elusive. The superior colliculus (mammals) and the optic tectum (other vertebrates) are intricately involved in stimulus selection and share common circuit features, including the nucleus isthmi. Investigating an anatomically- and physiologically-constrained network model of the avian

isthmotectal system, we found that recurrent antitopographic inhibition mediates competitive stimulus selection and that cellular spike-rate adaptation facilitates the selection of novel stimuli. Moreover, forebrain influences are integrated by their modulation of the isthmotectal circuitry, uniting both bottom-up and top-down mechanisms into a common control system.

Confidence in the validity of plausible model assumptions is supported by the fact that the model reproduces a wide range of in vivo observations from pigeons and owls (Marin et al. 2007; Winkowski and Knudsen 2008; Mysore et al. 2010; Asadollahi et al. 2010). The observations include shifts in activity to a novel stimulus, sharp transitions to strong stimuli, global competition, and changes in gain and sensitivity mediated by top-down control.

The extension of our investigation to a model network not constrained by the isthmotectal system revealed an alternative mechanism of competition, where competitive stimulus selection is mediated by homogeneous inhibition combined with a strong topographic excitation.

4.4.2 Recurrent antitopographic inhibition

The recurrent antitopographic inhibition extends throughout the entire structure, with a dip only at the center. This antitopographic organization is fundamentally different from the better-known surround inhibition in the center-surround organization. Here, the surround inhibition is largest at the center and vanishes asymptotically with increasing

distance. While this local organization is limited to local computations (contrast enhancement, edge detection, gain control); the far-reaching nature of the antitopographic inhibitory organization is ideally suited to mediate competitive interaction between distant sensory stimuli.

To date, the anatomical evidence for recurrent antitopographic inhibition is best documented for the avian isthmotectal system (Wang et al. 2004). The emergent role of the antitopographic inhibitory organization for stimulus selection raises the question whether this structural principle generalizes to other systems. In all species studied, reciprocal connections exist between the optic tectum (superior colliculus) and the nucleus isthmi (parabigeminal nucleus) (reviewed in Wang 2003; Gruberg et al. 2006; May 2006; Isa and Hall 2009). In reptiles and birds, the nucleus isthmi consist of spatially-separate cholinergic and GABAergic groups of neurons with topographic and diffuse, respectively, projections to the optic tectum (reptile: Sereno and Ulinski 1987; Powers and Reiner 1993; Saha et al. 2010; bird: Wang et al. 2004, 2006). The GABAergic diffuse isthmotectal projection modulates tectal cells and thereby, as shown here, can mediate the competitive interaction of visual stimuli in the avian isthmotectal system (Marin et al. 2005, 2007; Winkowski and Knudsen 2006; Mysore et al. 2010; Asadollahi et al. 2010). In mammals, the superior colliculus maintains topographic reciprocal connections with the parabigeminal nucleus (Graybiel 1978; Sherk 1979; Baizer et al. 1991; Jiang et al. 1996). The parabigeminal nucleus to SC projection is cholinergic (Wang et al. 1988; Hall et al. 1989; Hashikawa 1989), thus providing an excitatory topographic feedback. In contrast to birds and reptiles, for mammals, no

diffuse GABAergic projection from the parabigeminal nucleus to the superior colliculus has been reported. Rather, ACh release from parabigeminal nucleus axon terminals in SC activates GABAergic interneurons in the intermediate layers with broad projections (Binns and Salt 2000; Lee et al. 2001), which in turn inhibit projection neurons (Endo et al. 2005). Thus, in mammals the diffuse projection appears to be mediated by GABAergic interneurons within the superior colliculus that are activated by parabigeminal nucleus input.

4.4.3 Shifting spatial attention

The simulated competitive stimulus selection has an immediate functional significance for the avian isthmotectal system and the retino-tecto-rotundal visual pathway. Ipc axons form narrow tectal columns with hundreds of presynaptic terminals (Wang et al. 2006) (Fig. 4.2*a*), enabling Ipc neurons to gate tectal signal processing at that location (Wang 2003; Marin et al. 2007).

Attention is the selection of relevant signals from an enormous amount of often topographically-organized information. The isthmotectal system mediates a competitive stimulus selection, which results in a shift of Ipc axon terminal activity to the novel stimulus location in the retino-tecto-rotundal visual pathway. To date, the organization of the nucleus rotundus (pulvinar in mammals) has remained puzzling (Marin et al. 2003; Mahani et al. 2006). The simulated shift of Ipc activity may help to clarify this puzzle. This shift results in a selective mapping from the tectal topographic representation into

the rotundal representation. This implies that at any instant the rotundal representation contains the properties of only a single location in the visual scene, the selected location.

Interestingly, the isthmic activity that mediates the gating of tectal signals is not itself involved in the visual processing. Rather, isthmic activity selects the area of visual space that will be analyzed by tectal circuitry. This observation supports an early hypothesis of competitive stimulus selection, which postulates that the selection system itself is *not* responsible for the information processing relevant to the visual task, but merely selects which area of visual space should be inspected (Posner et al. 1980; Koch and Ullman 1985). This focal attention hypothesis was further popularized by the searchlight or spotlight metaphor (Crick 1984).

Perhaps surprisingly, psychophysical experiments indicate that focal selection does not necessarily involve contiguous parts of the visual field (Pylyshyn and Storm 1988; Sperling and Weichselgartner 1995). In other words, the spotlight does not seem to sweep continuously across the visual field. In this respect, the isthmotectal model results are consistent with focal selection in humans. Isthmic activity decreases at the target location, while increasing at the distant novel location (Fig. 4.3*a*). In terms of the spotlight metaphor, two (or more) spotlights are required; one spotlight fades at the target location while another spotlight brightens at the novel location. Neurons corresponding to locations between the target and novel location remain quiet during this process. From the model investigation, we know that in the isthmotectal system, the jump in activity is mediated by the long-range antitopographic inhibitory Imc feedback. This insight is

likely to provide a useful clue in the search for the underlying mechanisms of human focal selection.

The jump in isthmic activity, corresponding to a shift in spatial covert attention (no eye movements), is reminiscent of saccades and the concurrent shift in spatial overt attention (with eye movements). This may not be coincidental, as experimental evidence suggests a close relationship between covert and overt attention (Shepherd et al. 1986; Sheliga et al. 1995; Kustov and Robinson 1996). This relationship is particularly strong in the superior colliculus, which directs saccadic eye movements (Müller et al. 2005; Lovejoy and Krauzlis 2010). The excitatory isthmic feedback with axonal terminals in both, upper collicular layers of sensory processing and lower collicular layers of motor control, is thus ideally suited to communicate stimulus selection to the superior colliculus and to trigger concurrent jumps in spatial attention and saccadic eye movement to the same location.

4.4.4 The role of adaptation in stimulus competition

We show that adaptation within the isthmotectal circuitry, namely L10 and Imc spike-rate adaptation, can facilitate the competitive selection of novel stimuli (Fig. 4.4 and 4.8). We included cellular spike-rate adaptation in the model, because this implementation of adaptation is experimentally constrained in the avian isthmotectal circuit (Shao et al. 2009). However, our model investigation can not exclude that other implementations of adaptation, such as synaptic plasticity or delayed inhibition, contribute to isthmotectal stimulus competition as well.

Spike-rate adaptation depends on the activation history of the neuron. Thus a single neuron alone, receiving inputs from two locations, can not achieve novelty sensitivity. Rather, the enhanced sensitivity to a stimulus at a novel location is mediated by stimulus-specific adaptation. This adaptation depends on the stimulus history rather than on the activation history and has been described in visual and auditory pathways (Dragoi et al. 2002; Ulanovsky et al. 2003; Hosoya et al. 2005; Sharpee et al. 2006; Reches and Gutfreund 2008); although it has been challenging to pinpoint the biophysical implementation of adaptation in these complex circuits. In general, the computations to achieve stimulus-specific responses require a network to compare between current and past stimulus conditions (Abbott et al. 1997). In such a network, different stimuli activate separate paths to the stimulus-specific neuron and the adaptation is localized to the activated path (Eytan et al. 2003). This characteristic feature of stimulus-specific adaptation is present in the isthmotectal network, where stimuli at different locations activate adaptation in separate paths.

4.4.5 WTA networks

When a target and a distant competitor stimulus of different strength are presented simultaneously, the isthmotectal system can serve as a WTA network (Fig. 4.5*a*). We have shown that the observed distribution of slopes in the transition as a function of competitor strength (Asadollahi et al. 2010) can be reproduced by a distribution of the recurrent antitopographic inhibition strength (Fig. 4.5*a*). Interestingly, when the target and competitor stimulus width are varied, the Ipc response at the target location continues

to represent information about the target stimulus width (Asadollahi et al. 2010). Our model investigations reveal how this deviation from a winner-take-all behavior can be mediated by a combination of cellular and circuit mechanisms (Fig. 4.5*b*).

The theoretical analysis of neurally implemented maximum detectors has a long history (Koch and Ullman 1985). The architecture of model WTA networks falls into two broad categories: (I) lateral inhibition without self inhibition (Sum et al. 1999; Mao and Massaquoi 2007; Yuille and Grzywacz 1989) and (II) global inhibition with self excitation (Hahnloser et al. 1999, Brandt and Wessel, 2007). The anatomically-constrained model (Fig. 4.2) of the isthmotectal system includes elements of both network categories. The recurrent antitopographic inhibition (Imc → L10) belongs to category I, while the global inhibition (Imc → Ipc) with self excitation (Ipc → L10) belongs to category II. Depending on the relative strength of the inhibition and excitation, the stimulus maximum selection can be based on a combination of the two basic network categories. WTA selection and the selection of novel stimuli are related in that both require competitive interaction. However, the selection of novel stimuli poses higher requirements on the network. In a WTA network, strong inhibition usually ensures the selection of the winner (Hahnloser et al. 1999; Fig. 4.5*a*). In contrast, for inhibition above a certain level the network fails to respond to novel stimuli. Thus a network has to maintain its inhibition at an appropriate level to execute the task of novelty detection (Fig. 4.6).

4.4.6 Top-down modulation of the stimulus-response function

Our model provides new insight into the microcircuit mechanisms of top-down stimulus-response modulation (Fig. 4.9). Directing attention to a target stimulus enhances visual responses of cortical neurons (V4) to the attended stimulus while suppressing the responses to other stimuli (reviewed in Reynolds and Heeger 2009). The effects of focal attention on V4 visual responses can be mimicked by low-level electrical microstimulation of the macaque frontal eye field region (Moore and Armstrong 2003). This microstimulation paradigm was extended to the owl forebrain arcopallial gaze field ([AGF], putative homolog of the primate frontal eye field region), which projects to both the nucleus isthmi and the deep tectal layers (Knudsen et al. 1995). Stimulating an AGF site aligned with the receptive field of a recorded deep tectal neuron caused a leftward shift of the neurons stimulus-response function. In contrast, stimulating an AGF site outside the receptive field of a recorded deep tectal neuron reduced the responses across all stimulus levels (Winkowski and Knudsen 2008).

The observed differential effect of aligned and non-aligned AGF stimulation has led to the suggestion that AGF inputs involve two distinct mechanisms modulating tectal responses (Winkowski and Knudsen 2008). Our model investigation indicates two such mechanisms. The aligned AGF stimulation causes a leftward shift of the neurons stimulus response function via the direct AGF excitation of tectal L10 neurons. The non-aligned AGF stimulation, however, reduces the responses across all stimulus levels dynamically via the competitive interaction of the target stimulus and the distal top-down input onto L10 and Imc neurons. The long-range interaction is then mediated by the antitopographic

inhibitory Imc → L10 projection. The isthmotectal circuit thus integrates the top-down influence into the bottom-up competitive interaction network.

The top-down modulation results in stimulus-response functions may be mimicked, at least for simple stimuli, by the normalization model of attention. However, the phenomenological normalization model (Reynolds and Heeger 2009) and the circuit-based competitive interaction model (Fig. 4.2*b*, *c,* 4.9*a*) are fundamentally different. The former is based on feedforward mechanisms and steady-state firing rates alone, whereas the latter includes feedback and temporal aspects of the responses. Specifically, in response to simple stimuli, the circuit-based model predicts that nonaligned top-down input imposes periodic bursting on target responses that synchronize with the activity at the top-down input location (Fig. 4.10). We hypothesize that in natural viewing the differences in predictions of stimulus-response modulation between the two classes of models will become more apparent.

In conclusion, based on the detailed anatomical information of the avian isthmotectal system, the present study reveals a set of neural mechanisms for competitive stimulus selection. Given the parallels between attentional phenomenology of barn owls and rhesus monkey (Reynolds 2008; Winkowski and Knudsen 2008), it will be interesting to see to what extent this detailed circuit insight will assist useful working hypotheses for the investigation of attentional selection in monkey and man.

4.5 Acknowledgements

The authors thank Michael Ariel, Anders Carlsson, Baranidharan Raman, Larry Snyder, Jeff Zacks, and members of the Neurophysics Lab for critical reading of the manuscript.

4.6 GRANTS

This research was supported by NIH grant R01EY018818 to R.W..

4.7 References

Abbott LF, Varela JA, Sen K, Neslon SB (1999) Synaptic depression and cortigal gain control. Science 275: 220-224.

Asadollahi A, Mysore SP, Knudsen EI (2010) Stimulus-driven competition in a cholinergic midbrain nucleus. Nat Neurosci 13: 889–895.

Baizer JS, Whitney JF, Bender DB (1991) Bilateral projections from the parabigeminal nucleus to the superior colliculus in monkey. Exp Brain Res 86: 467-470.

Binns KE, Salt TE (2000) The functional influence of nicotinic cholinergic receptors on the visual responses of neurons in the superficial superior colliculus. Vis Neurosci 17: 283-289.

Bisley JW (2010) The neural basis of visual attention. J Physiol DOI 10.1113.

Brandt SF, Wessel R (2007) Winner-take-all selection in a neural system with delayed feedback. Biol Cybernetics 97: 221-228.

Caudill MS, Brandt SF, Nussinov Z, Wessel R (2009) An intricate phase diagram of a prevalent visual circuit reveals universal dynamics, phase transitions and resonances. Phys Rev E 80: 051923.

Cohen YE, Knudsen EI (1995) Binaural tuning of auditory units in the forebrain archistriatal gaze fields of the barn owl: local organization but no space map. J Neurosci 15: 5152–5168.

Cohen YE, Knudsen EI (1999) Maps versus clusters: different representations of auditory space in the midbrain and forebrain. Trends Neurosci 22: 128-35.

Crick F (1984) Function of the thalamic reticular complex: The searchlight hypothesis. Proc Natl Acad Sci 81: 4586-4590.

Desimone R, Duncan J (1995) Neural mechanisms of selective visual attention. Annu Rev Neurosci 18: 193-222.

Destexhe A, Mainen ZF, Sejnowski TJ (1994) Synthesis of models for excitable membranes, synaptic transmission and neuromodulation using a common kinetic formalism. J Computational Neurosci 1: 195-230.

Dragoi V, Sharma J, Miller EK, Sur M (2002) Dynamics of neuronal sensitivity in visual cortex and local feature discrimination. Nat Neurosci 5: 883-891.

Endo T, Yanagawa Y, Obata K, Isa T (2005) Nicotinic acetylcholine receptor subtypes involved in facilitation of GABAergic inhibition in mouse superficial superior colliculus. J Neurophysiol 94: 3893–3902.

Eytan D, Brenner N, Marom S (2003) Selective adaptation in networks of cortical neurons. J Neurosci 23: 9340-9356.

Felix D, Wu GY, Wang SR (1994) GABA as an inhibitory transmitter in the pigeon isthmotectal pathway, Neurosci Lett 169: 212–214.

Fries P, Reynolds JH, Rorie AE, Desimone R (2001) Selective Visual Attention Modulation of Oscillatory Neuronal Synchronization. Science 291: 1560-1563.

Graybiel AM (1978) A satellite system of the superior colliculus: the parabigeminal nucleus and its projection to the superficial collicular layers. Brain Res 145: 365-374.

Gruberg ER, Dudkin EA, Wang Y, Marin G, Salas C, Sentis E, Letelier JC, Mpodozis J, Malpeli J, Cui H, Ma R, Northmore D, Udin S (2006) Influencing and interpreting visual input: The role of a visual feedback system. J Neurosci 26: 10368-10371.

Hahnloser R, Douglas RJ, Mahowald M, Hepp K (1989) Feedback interactions between neuronal pointers and maps for attentional processing. Nature Neurosci 2: 746-752, 1999.

Hall WC, Fitzpatrick D, Klatt LL, Raczkowski D. Cholinergic innervation of the superior colliculus in the cat. J Comp Neurol 287: 495–514.

Hall WC, Moschovakis A (2004) The superior colliculus: New approaches for studying sensorimotor integration. London: CRC Press.

Hashikawa T (1989) Regional and laminar distribution of choline acetyltransferase immunoreactivity in the cat superior colliculus. Neurosci Res 6: 426–437.

Hosoya T, Baccus SA, Meister M (2005) Dynamic predictive coding by the retina. Nature 436: 71-77.

Ignashchenkova A, Dicke PW, Haarmeier T, Thier P (2004) Neuron-specific contribution of the superior colliculus to overt and covert shifts of attention. Nat Neurosci 7: 56-64.

Isa T, Hall WC (2009) Exploring the superior colliculus in vitro. J Neurophysiol 102: 2581-2593.

Itti L, Koch C (2001) Computational modeling of visual attention. Nat Rev Neurosci 2: 194-229.

Jiang ZD, King AJ, Moore DR (1996) Topographic organization of projection from the parabigeminal nucleus to the superior colliculus in the ferret revealed with fluorescent latex microspheres. Brain Res 743: 217–232.

Kastner S, Ungerleider G (2000) Mechanisms of visual attention in the human cortex. Annu Rev Neurosci 23: 315-341.

Knudsen EI (2007) Fundamental Components of Attention. Annu Rev Neurosci 30: 57-78.

Knudsen EI, Cohen YE, Masino T (1995) Characterization of a forebrain gaze field in the archistriatum of the barn owl: Microstimulation and anatomical connections. J Neurosci 15: 5139-5151.

Koch C (1999) Biophysics of computation. New York: Oxford University Press.

Koch C, Ullman S (1985) Shifts in selective visual attention: towards the underlying neural circuitry. Human Neurobiol 4: 219-227.

Kustov AA, Robinson DL (1996) Shared neural control of attentional shifts and eye movements. Nature 384: 74-77.

Lee DK, Itti L, Braun J (1999) Attention activates winner-take-all competition among visual filters. Nat Neurosci 2: 375-381.

Lee PH, Schmidt M, Hall WC (2001) Excitatory and inhibitory circuitry in the superficial gray layer of the superior colliculus. J Neurosci 21: 8145-8153.

Lewis T, Rinzel J (2003) Dynamics of spiking neurons connected by both inhibitory and electrical coupling. J Computational Neuroscience 14: 283-309.

Li X, Basso MA (2005) Competitive stimulus interactions within single response fields of superior colliculus neurons. J Neurosci 25: 11357-11373.

Lovejoy LP, Krauzlis RJ (2010) Inactivation of primate superior colliculus impairs covert selection of signals for perceptual judgments. Nat Neurosci 13: 261-266.

Mahani AS, Khanbabaie R, Luksch H, Wessel R (2006) Sparse spatial sampling for the computation of motion in multiple stages. Biol Cybernetics 94: 276-287.

Mao ZH, Massaquoi SG (2007) Dynamics of winner-take-all competition in recurrent neural networks with lateral inhibition. IEEE Transactions on Neural Networks 18: 55-69.

Marin G, Letelier JC, Henny P, Sentis E, Farfan G, Fredes F, Pohl N, Karten H, Mpodozis J (2003) Spatial organization of the pigeon tecto-rotundal pathway: An interdigitating topographic arrangement. J Comp Neurol 458: 361-380.

Marin G, Mpodozis J, Sentis E, Ossandon T, Letelier JC (2005) Oscillatory bursts in the optic tectum of birds represent re-entrant signals from the nucleus isthmi pars parvocellularis. J Neurosci 25: 7081-7089.

Marin G, Salas C, Sentis E, Rojas X, Letelier JC, Mpodozis J (2007) A cholinergic gating mechanism controlled by competitive interactions in the optic tectum of the pigeon. J Neurosci 27: 8112-8121.

May PJ (2006) The mammalian superior colliculus: laminar structure and connections. Progress in Brain Research 151: 321-378.

McPeek RM, Keller EL (2004) Deficits in saccade target selection after inactivation of superior colliculus. Nat Neurosci 7: 757-763.

Mitchell JF, Sundberg KA, Reynolds JH (2007) Differential attention dependent response modulation across cell classes in macaque visual area V4. Neuron 55: 131–141.

Moore T, Armstrong KM (2003) Selective gating of visual signals by microstimulation of frontal cortex. Nature 421: 370-373.

Mulckhuyse M, Theeuwes J (2010) Unconscious attentional orienting to exogenous cues: A review of the literature. Acta Psychologica 134: 299-309.

Müller JR, Philiastides MG, Newsome WT (2005) Microstimulation of the superior colliculus focuses attention without moving the eyes. Proc Natl Acad Sci 102: 524-529.

Mysore SP, Asadollahi A, Knudsen EI (2010) Global inhibition and stimulus competition in the owl optic tectum. J Neurosci 30: 1727-1738.

Olshausen BA, Anderson CH, Essen DCV (1993) A neurobiological model of visual attention and invariant pattern recognition based on dynamic routing of information. J Neurosci 13: 4700-4719.

Posner MI (1980) Orienting of attention. Quart J Exp Psychol 32: 3-25.

Powers AS, Reiner A (1993) The distribution of cholinergic neurons in the central nervous system of turtles. Brain Behav Evol 41: 326-345.

Pylyshyn ZW, Storm RW (1988) Tracking multiple independent targets: Evidence for a parallel tracking mechanism. Spatial Vision 3: 1-19.

Rabinovich M, Huerta R, Laurent G (2008) Transient dynamics for neural processing. Science 321: 48-50.

Ranganath C, Rainer G (2003) Neural mechanisms for detecting and remembering novel events. Nat Rev Neurosci 4: 193-201.

Reches A, Gutfreund Y (2008) Stimulus-specific adaptations in the gaze control system of barn owl. J Neurosci 28: 1523-1533.

Reynolds JH, Chelazzi L, Desimone R (1999) Competitive mechanisms subserve attention in macaque areas V2 and V4. J Neurosci 19: 1736-1753.

Reynolds JH, Pasternak T, Desimone R (2000) Attention increases sensitivity of V4 neurons. Neuron 26: 703–714.

Reynolds JH (2008) Three hundred million years of attentional selection. Neuron 60: 528-530.

Reynolds JH, Heeger DJ (2009) The normalization model of attention. Neuron 61: 168-185.

Saha D, Morton D, Ariel M, Wessel R (2010) Visual response properties of a cholinergic neuron in turtle nucleus isthmi. J Comp Physiol A, in press.

Sereno MI, Ulinski PS (1987) Caudal topographic nucleus isthmi and the rostral nontopographic nucleus isthmi in the turtle, Pseudemys scripta. J Comp Neurology 261: 319-346.

Shao J, Lai D, Meyer U, Luksch H, Wessel R (2009) Generating oscillatory bursts from a network of regular spiking neurons without inhibition. J Comput Neurosci 27: 591–606.

Sharpee TO, Sugihara H, Kurgansky AV, Rebrik SP, Stryker MP, Miller KD (2006) Adaptive filtering enhances information transmission in visual cortex. Nature 439: 936-942.

Sheliga BM, Riggio L, Craighero L, Rizzolatti G (1995) Spatial attention-determined modifications in saccade trajectories. Neuroreport 6: 585-588.

Shepherd M, Findlay JM, Hockey, RJ (1986) The relationship between eye movements and spatial attention. Quarterly J Exp Psychol 38A: 475-491.

Sherk H (1979) Connections and visual field mapping in cat's tectoparabigeminal circuit. J Neurophysiol 42: 1656-1668.

Shpiro A, Curtu R, Rinzel J, Rubin N (2007) Dynamical characteristics common to neuronal competition models. J Neurophysiol 97: 462-473.

Sperling G, Weichselgartner J (1995) Episodic theory of the dynamics of spatial attention. Psychological Review 102: 503-532.

Stein BE, Meredith MA (1993) The merging of the senses. Cambridge: MIT Press.

Sum JPF, Leung CS, Tam PKS, Young GH, Kan WK, Chan LW (1999) Analysis for a class of winner-take-all model. IEEE Transactions on Neural Networks 10: 64-71.

Ulanovsky N, Las L, Nelken I (2003) Processing of low-probability sounds by cortical neurons. Nat Neurosci 6: 391-398.

Usher M, Niebur E (1996) Modeling the temporal dynamics of IT neurons in visual search: A mechanism for top-down selective attention. J Cognitive Neurosci 8: 311-327.

Veenman CL, Albin RL, Richfield EK, Reiner A (1994) Distributions of GABAA, GABAB, and benzodiazepine receptors in the forebrain and midbrain of pigeons. J Comp Neurol 344:161–189.

Wang YQ, Takatsuji K, Yamano M, Tohyama, M (1988) Localization of neuroactive substances in the rat parabigeminal nucleus: an immunohistochemical study. J Chem Neuroanat 1:195–204.

Wang SR (2003) The nucleus isthmi and dual modulation of the receptive field of tectal neurons in non-mammals. Brain Research Reviews 41: 13-25.

Wang Y, Major DE, Karten HJ (2004) Morphology and connections of nucleus isthmi pars magnocellularis in chicks. J Comparative Neurol 469: 275-297.

Wang Y, Luksch H, Brecha NC, Karten HJ (2006) Columnar projections from the cholinergic nucleus isthmi to the optic tectum in chicks (gallus gallus): a possible substrate for synchronizing tectal channels. J Comparative Neurol 494: 7-35.

Winkowski DE, Knudsen EI (2006) Top-down gain control of the auditory space map by gaze control circuitry in the barn owl. Nature 439: 336 –339.

Winkowski DE, Knudsen EI (2007) Top-down control of multimodal sensitivity in the barn owl optic tectum. J Neurosci 27: 13279–13291.

Winkowski DE, Knudsen EI (2008) Distinct mechanisms for top-down control of neural gain and sensitivity in the owl optic tectum. Neuron 60: 698-708.

Wilson HR, Krupa B, Wilkinson F (2000) Dynamics of perceptual oscillations in form vision. Nat Neurosci 3: 170-176.

Yuille AL, Grzywacz NM (1989) A winner-take-all mechanism based on presynaptic inhibition feedback. Neural Computation 1: 334-347.

5 Competitive selection and local feedback modulate population coding of motion-sensitive wide-field neurons

5.1 Abstract

A salient stimulus gains the focus of attention via competitive mechanisms. The neural representation of the selected stimulus is enhanced and further mapped to higher visual area. The midbrain isthmic nucleus is involved in competitive selection and information flow control. Here we investigate the hypothesis that the retino-tectal synaptic transmission is modulated by cotransmission of acetylcholine (ACh) and glutamate from parvocellular isthmic (Ipc) nucleus. We show the blockade of nicotinic acetylcholine receptor (nAChR) alters the time course of synaptic depression. The suppression of tectal response to electric stimulation at Ipc nucleus by CNQX supports the hypothesis that Ipc neurons also innervate the optic tectum (OT) by glutamate. In a model of OT and its nucleus, we demonstrate that the release of ACh can lead to divisive modulation of the tectal responses to motion. The effect is dependent on stimulus intensities. We further reveal how the glutamatergic feedback might evoke coherent activity in the SGC-I population.

5.2 Introduction

Attentional modulation optimizes visual processing by enhancing neural response to attended location (Ito and Gilbert, 1999; McAdams and Maunsell, 1999) or altering coherent activities of neural population (Fries et al., 2001). The studies have suggested a two-phase algorithm the brain might adopt to accomplish such tasks through its intricate neural circuits. In the first phase, competitive mechanisms (e.g. winner-take-all) serve to determine the most salient location in topographic representation maps of visual field (Koch and Ullman, 1985; Reynolds et al., 1999). The selected region becomes the focus of attention and the visual representation of particular properties (spatial location, color, orientation etc.) is facilitated and further processed at high-level brain structure in the second phase (Maunsell and Treue, 2006; Knudsen, 2007). The circuitry that dynamically guides the attentional focus in the first phase is not necessarily directly involved in sensory information processing (Koch and Ullman, 1985; Olshausen et al., 1993). In a large scale, the thalamic pulvinar is hypothetically suggested as the major source of the routing control of the ventral stream in visual cortex (Anderson et al., 2005). However, a neurobiological understanding of the attentional control mechanism is still missing.

The mesencephalic OT (mammalian superior colliculus) is responsible for motion processing (Figure 5.1A). Neurons in deep and intermediate tectal layers are sensitive to translational and looming stimuli (Frost and Nakayama, 1983; Yan and Wang, 1986; Mysore et al., 2010). The OT forms reciprocal connections with the parvocellular (Ipc, mammalian parabigeminal nucleus) and the magnocellular (Imc) isthmic nuclei (Wang et al., 2004, 2006). Both nuclei contain topographic visual space maps (Wang and Frost,

1991) and send back their axons to OT in topographic and antitopographic manners respectively (Wang et al., 2004, 2006). This intertwined midbrain organization is thought to direct spatial attention together with forebrain network (Knudsen, 2011).

The nucleus structure Ipc innervates multiple layers of OT through its columnar axon terminals (Wang et al., 2006). The Ipc axons arborize densely at the retinorecipient layer 5 where the retina fibers contact the extensive circular dendritic field of SGC-I neurons (Figure 5.1 B, C). The feedback projection controls signal flow of the tectofugal pathway (Luksch et al., 1998; Karten et al., 1997; Marin et al., 2003) and local inactivation of Ipc nucleus impairs the response at corresponding Rt area. Responses of Rt and entopallium are found synchronous to the bursting activities of Ipc (Marin et al., 2007, 2012) but Ipc neurons show no direct axonal projections to the higher visual areas. Understanding the role of Ipc feedback in determining the circuit dynamics requires the assessment of two questions. Firstly, what is the interactive mechanism between Ipc axons and the targeted tectal neurons? Secondly, how is the Ipc-tectum interaction related to the observed circuit dynamics? Moreover, Ipc neurons are involved in competitive selections of multiple stimuli and are most responsive to salient stimuli in a visual scene (Marin et al., 2007; Asadollahi et al., 2011). Understanding the role of Ipc feedback is important for interpreting attention and gaze control in visual processing (Knudsen, 2011).

Here we studied the role of Ipc feedback on retino-tectal synaptic transmission in a tectal slice preparation and reveals its effect on tectal motion processing in an experimentally constrained model network. We show that the blockade of nAChR alters the dynamics of

synaptic depression. The excitatory response evoked by electric stimulation at Ipc nucleus is reduced by bath application of CNQX, indicating the involvement of glutamate in synaptic transmission. In the computational model, we demonstrate how the cotransmission of ACh and glutamate may modulate the response of tectal SGC-I cell to motion.

5.3 Methods

Experiments**:** Tectal slices were prepared from White Leghorn chick hatchlings (*Gallus gallus*; <5d old). All procedures used in this study were approved by the local authorities and conform to the guidelines of the *National Institutes of Health Guide on the Care and Use of Laboratory Animals*. Briefly, chickens were anesthetized, the brain was quickly removed and the optic tectum was sectioned at 300-450 μm. Stable whole cell recordings were obtained from a total of n = 67 SGC-I neurons with glass micropipettes pulled from borosilicate glass. The series resistance of recording was 10 ± 3 MΩ and was routinely compensated. Electro-stimulations were carried out with bipolar tungsten electrodes as described previously (Luksch et al. 2001, 2004). The SGC-I cells were recorded from the outer layer of tectal L13 and are characterized by their chattering response to somatic current injection. The cells have stable resting membrane potentials of -59.1 ± 7.3 mV (mean±SD). Sharp-onset spikes are recorded when pulse stimulations were delivered at tectal layer 2-4 and a second pulse within 30 ms always fails to drive any responses (Luksch et al 2001, 2004). Pulse train stimuli of certain inter-pulse-intervals Δt were typically repeated 5 times with a waiting time of 3-5 min between trials. Various stimulation intervals were tested in a pseudorandom sequence.

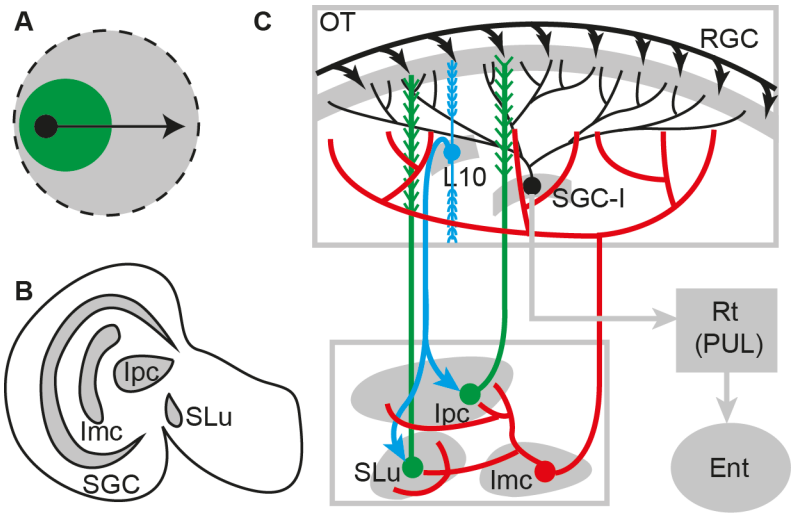

Figure 5.1 The schematics of the tectofugal pathway. A, The SGC-I neurons have large RF (gray) and the RF of the cell is modulated by local Ipc feedback (green). B, Tectal slice contains the layer 13 SGC neurons, the Ipc and SLu nucleus. C, The dendritic endings of SGC-I cells receive the axonal projection from retina at the retinorecipient layer 5. The retino-tectal synapses are modulated by the tectal-isthmic feedback loop, consisting of L10 (blue), Ipc and SLu neurons (green).

To determine the effect of acetylcholine on retino-tectal transmission, we bath applied to the slice [20 μM], mecamylamine (Sigma-Aldrich, St. Louis), a non-competitive nAChR antagonist and repeated the recording under the control condition. Washout was observed in 3/10 cases, which is consistent with the assumption that mecamylamine is a use dependent reversible drugs (Fedorov et al., 2009) and has a slow recovery/dissociation rate from nicotinic receptors (Papke et al., 2001), which might result in irreversible cumulative (use-dependent) block with repeated application. The role of mAChR receptors was also tested by bath application of the antagonist atropine but no significant response change was observed (n = 3, data not shown).

To exam whether the SGC-I response is stationary, we analyze the response probability of SGC-I neurons (n = 57) in control conditions by dividing the recorded trials into two halves and calculating the response probability over the first half ($P = 0.536 \pm 0.07$) and the second half ($P = 0.526 \pm 0.07$). No significant change is observed. To further test that the SGC-I responses are stationary over the recording period before and after application of mecamylamine, we recorded from a separate set of SGC-I neurons (n = 6) over a typical recording time of 50 minutes without drug application. The response probability for the first and second half trials are $P = 0.363 \pm 0.14$ and $P = 0.355 \pm 0.14$ ($mean \pm s.e.m.$), respectively.

We also tested the hypothesis that the Ipc axons release glutamate (Gonzalez-Cabrera et al, 2011). Intracellular whole cell patch recordings were made from tectal neurons while electric stimulations were delivered to Ipc nucleus with bipolar tungsten electrode. Ipc nucleus was located by identifying Ipc neurons with intracellular recording. The Ipc neurons typically have membrane time constant ~35 ms and membrane resistance ~114 MΩ. The Ipc neurons respond to step current injection with regular spikes and show numerous spontaneous activity. We then placed the bipolar tungsten electrode in the Ipc nucleus and recorded the response of tectal neurons while electric pulses are delivered. After recording 10~20 trials in the normal saline, [10 μM] CNQX (Sigma-Aldrich) was bath applied to the tectal slice and synaptic responses of tectal neurons were recorded.

Model. We constructed a 5-layer two-dimensional neural network whose architecture is constrained to the anatomy of the retino-tecto-rotundal and isthmotectal pathway. The

model network consists of 5 arrays of neurons, representing retina ganglion cells (RGC), SGC-I, tectal layer 10 neurons (L10), magnocellular (Imc) and parvocellular (Ipc) isthmic neurons, respectively.

RGC layer. The RGC layer is modeled as a $N_{RGC} \times N_{RGC}$ neuron grid, representing a visual field of 60°x60°. Unless otherwise stated, RGC array have a size of $N_{RGC} = 100$. Each RGC neuron is modeled as a binary neuron that either has a spiking or a non-spiking state. The presence of a stimulus in the visual field will randomly trigger the responses of corresponding RGC neurons. The dynamic response of each RGC neurons is modeled as a Poisson process of rate $r = r_{RGC} \exp(-\frac{(i_x - C_x)^2}{2\sigma_s^2} - \frac{(i_y - C_y)^2}{2\sigma_s^2})$, where C_x and C_y indicate the center of the stimulus. i_x and i_y determine the coordinate of *ith* RGC cell. The stimulus size is indicated by σ_s. r_{RGC} is peak firing rate triggered at the center of the stimulus.

SGC-I layer. We considered a 40 x 40 SGC-I neuron grid with its nodes uniformly distributed over the visual field considered. The dendrites of each SGC-I neuron sample the activities of RGC neurons and have a cosine distribution about the center of the receptive field $\rho(r) = a(1 + \cos(\pi r / R))$, where r is the distance between the receptive field center of the SGC-I dendrite and the RGC neuron. The receptive field radius R is experimentally constrained and chosen as $\sim 20^\circ$. The normalization factor $a = \pi N_d / (R^2(\pi^2 - 4))$ ensures $\int_0^R 2\pi r \rho(r)\, dr = N_d$, where N_d is the estimated number of

dendritic endings of each SGC-I cell and constrained as $N_d = 160$ (Mahani et al., 2006). Each SGC-I dendrite responds in a binary manner to RGC spikes with probability $P(\Delta t) = P_{\max}(1 - e^{-\Delta t/\tau})$, where Δt is the interval between two RGC spikes. The maximum response probability $P_{\max}$ is reached at the limit $\Delta t \to \infty$ when the interval between two stimulating pulse is large and according to the experimental measurement we set $P_{\max} = 0.9$. The time constant τ describes the recovery speed of SGC-I dendrites from synaptic depression. The dendritic spikes cause somatic spikes if no spike was generated previously at the soma within a refractory period of $T_r = 30$ ms (Luksch et al., 2004). Accordingly, SGC-I spike rate will not exceed the limit of 33.3 Hz. Moreover, the dendrite of the SGC-I neurons also receives modulatory inputs from the Ipc neurons. Each SGC-I dendrites is modulated by an Ipc neuron whose receptive field center is the most adjacent to the SGC-I dendrites. The dynamics of the modulation is described in details in following session.

L10, Ipc, Imc layers. The three layers represent the isthmotectal system and are modeled as three 40x40 neuron arrays. The neurons are modeled as leaky-integrate-fire type with spike-rate adaptation. The cellular and synaptic properties are modeled as described in previous works (Shao et al., 2009, Lai et al., 2011). The anatomical features of the isthmotectal connections are captured by the synaptic weights w_{ij}. Specifically, two types of connection structure, topographic and anti-topographic are described by 2D-Gaussian functions of the forms $w_{ij} = \exp(-\frac{(i_x - j_x)^2}{2\sigma_x^2} - \frac{(i_y - j_y)^2}{2\sigma_y^2})$ and

$w_{ij} = 1 - D\exp(-\frac{(i_x - j_x)^2}{2\sigma_x^2} - \frac{(i_y - j_y)^2}{2\sigma_y^2})$, respectively. The index i and j indicate the neuron at post and pre end of the synapses. The subscription x and y denotes the two dimensions at the neuron grids.

Cholinergic modulation. The release of ACh from Ipc neurons shortens the recovery time constant τ of SGC-I dendrites. Here we assume the dynamics follows the formula $\tau(t) = \tau_0/(1+\beta(t))$, where $\beta(t)$ could be interpreted as a quantity that described the amount of ACh that is released. Without presynaptic Ipc activity, no ACh is released and the quantity decays over time according to $\tau_\beta d\beta(t)/dt = -\beta(t)$. It has an increment $\beta(t) \to \beta(t) + \varepsilon e^{-\beta(t)}$ whenever an Ipc spike occurs. Here ε is the increment amount induced by Ipc spikes, when no acetylcholine is released $\beta(t) = 0$. The increment is dependent on the existing acetylcholine release and $\beta(t)$ cannot go unbounded. τ_β is a time constant that describes how long the acetylcholine will stay at the targeting location.

Response of SGC-I soma. The dendrites of a SGC-I neuron respond to RGC pulses in a binary manner with probability $P(\Delta t) = P_{\max}(1 - e^{-\Delta t/\tau})$. In response to Poisson pulse trains, the response probability could be effectively considered as having two components: the transient $P_o \sim P_{\max}$ and the steady state $P_s \sim P_{\max}\Delta t/\tau$ given a high RGC input rate ($\Delta t << 1$). We therefore decompose the dendritic response into two random processes: the transient response $D_{o,i}(t)$ that is triggered by the initial spike within the pulse train and the steady-state component $D_{s,i}(t)$ that is triggered by the rest, where i indicates the

dendritic index of a SGC-I neuron. The indices vary over time as the stimulus is moving across the visual field of the neuron. The somatic response $X(t)$ of a SGC-I neuron is therefore the superposition of the dendritic spikes $X(t) = \left(\sum_i \left(D_{o,i}(t) + D_{s,i}(t) \right) \right)_{T_r}$, the subscript indicates that the somatic response is modulated by the refractory period and two spikes will not occur within a time window of T_r ms.

Assuming that *ith* dendrites of a SGC-I neuron generated spike at a time set $\{t_j\}_i$, the firing rate of a SGC-I soma is evaluated by the formula $r_{SGC} = \left(\frac{1}{T} \int dt \left(\sum_{i,j} \delta_{o,i}(t - t_j) + \sum_{i,j} \delta_{s,i}(t - t_j) \right) \right)_{T_r}$. Here δ is the Dirac-delta function. We consider the spike train as a result of the transient and steady state response, denoted by the subscripts o and s, respectively. T_r indicates the refractory period of somatic spike.

To get a estimation of the SGC firing rate, we neglect the refractory period and assume that $T_r = 0$ ms. *Transient response of SGC-I soma*: The transient response of a SGC-I dendrite is evoked when the first spike in a RGC pulse train is delivered. Since the response probability is close to ~1, it is highly probable that a dendritic spike is triggered. In the presence of a moving dot, the transient response occurs shortly after the stimulus enters the RF of a SGC-I dendrite. Since only one transient spike will occur at each dendritic ending, the transient component of the somatic firing rate can be evaluated as $\frac{1}{T} \int dt \sum_{i,j} \delta_{o,i}(t - t_j) \approx \frac{n_d P_{\max}}{T}$, where n_d is the number of dendrites that confront the

moving dot during its presence. *Steady state response of SGC-I soma:* The steady state response is dependent on the intervals between RGC spikes. Given RGC rate of r_{RGC}, the pulse interval is approximately $\Delta t \sim \frac{1}{r_{RGC}}$. Given a high RGC input rate, the *ith* dendrite of a SGC-I neuron respond with Poisson spike train of rate $r_i = r_{RGC} P_s \sim P_{\max} / \tau$. The steady state somatic firing rate is accordingly estimated as $\frac{1}{T}\int_0^{T_D} dt \sum_{i,j} \delta_{s,i}(t - t_j) \approx \frac{n_d T_D P_{\max}}{\tau T}$, where T_D is time duration that a stimulus stays within the *ith* dendrite. The effect of acetylcholine is quantified by calculating the enhancement factor $F_e \equiv \frac{r_{SGC}}{r_{0,SGC}}$, where r_{SGC} and $r_{0,SGC}$ are the response rate of a SGC-I neuron with and without the modulation of Ipc activity, respectively.

Cross-correlation. The cross-correlation coefficients between two SGC-I neurons C_i and C_j are calculated by the formula $\rho_{ij} = \frac{\mathrm{cov}(m_i, m_j)}{\sqrt{\mathrm{var}(m_i)}\sqrt{\mathrm{var}(m_j)}}$, where m_i, m_j is the number of SGC spikes counted in a sliding time window of certain length. We divide the spike count into transient and steady state components as $m_i = m_{o,i} + m_{s,i}$. By assuming independence between the two components and no refractory period $T_r = 0$, we get a rough evaluation for the cross-correlation coefficient

$$\rho_{ij} \approx \frac{\mathrm{cov}(m_{o,i}, m_{o,j}) + \mathrm{cov}(m_{s,i}, m_{s,j})}{\sqrt{\mathrm{var}(m_{o,i}) + \mathrm{var}(m_{s,i})}\sqrt{\mathrm{var}(m_{o,j}) + \mathrm{var}(m_{s,j})}} \qquad (1)$$

To further understand the cross-correlation among the SGC-I population in the presence of glutamatergic modulation, we consider two SGC-I neurons i and j with response probability p to pulse stimulation. The dendrites of each SGC-I neurons could be naturally divided into two parts: (1) the dendrites that share common synaptic inputs from RGC neurons, the number of which are denoted by n_c (2) the dendrites that receive RGC excitation independently, denoted by n_s. Assuming a symmetric dendrite distribution, we have the dendritic number $\langle n_{s,j} \rangle = \langle n_{s,i} \rangle = n_s$. We decompose the spikes into two components: the response due to common pulse inputs and the independent pulse inputs, we accordingly have $m_i = m_{c,j} + m_{s,j}$. Each dendrite responds to the Poisson pulse train of rate r_{RGC} into a Poisson spike train of rate pr_{RGC} and therefore we have $\langle m_{c,i} \rangle = \langle m_{c,j} \rangle = n_c p r_{RGC} T$ and $\langle m_{s,i} \rangle = \langle m_{s,j} \rangle = n_s p r_{RGC} T$. The covariance between i and j SGC-I neuron is only dependent on the spikes induced by common RGC inputs and $\langle m_i m_j \rangle - \langle m_i \rangle \langle m_j \rangle = \langle m_{c,i} m_{c,j} \rangle - \langle m_{c,i} \rangle \langle m_{c,j} \rangle$. In order to estimate $\langle m_{c,i} m_{c,j} \rangle$, we consider the case when the common pulse inputs deliver a spike train of l spikes. Since the dendritic response of neuron i and j are independent given a fixed pulse train, we have $\langle m_{c,i} m_{c,j} \rangle_l = \langle m_{c,i} \rangle_l \langle m_{c,j} \rangle_l = l^2 p$. It follows that $\langle m_{c,i} m_{c,j} \rangle = \sum_{m=0}^{\infty} P_l l^2 p^2 = p^2 (n_c r_{RGC} T + (n_c r_{RGC} T)^2)$ where l obeys the Poisson distribution and we have $P_l = \frac{(n_c r_{RGC} T)^l e^{-n_c r_{RGC} T}}{l!}$. The spike number covariance between neuron i and j is accordingly $\langle m_i m_j \rangle - \langle m_i \rangle \langle m_j \rangle = p^2 n_c r_{RGC} T$ and the cross correlation coefficient

$\rho_{ij} = pn_c / (n_s + n_c)$. The cross-correlation is dependent on the response probability and the number of SGC-I dendrites that share common RGC inputs.

Glutamatergic modulation from Ipc neurons. In additional to its role as a cholinergic modulator, the axonal feedback from Ipc neurons might also use glutamate as neurotransmitter. We introduced an additional parameter to the model and assumed that each spike of Ipc neurons will trigger the corresponding dendrites of SGC-I neurons to spike with probability p_{Glu}.

5.4 Results

5.4.1 The role of ACh on retino-tectal synaptic transmission

To characterize the properties of synaptic transmission from RGC to OT, we locally stimulated the RGC axons at the superficial layers of the tectal slice and recorded the response of SGC-I somata. The effect of ACh on the transmission is determined by repeating the measurement with bath application of mecamylamine, a nAChR antagonist. Specifically, a pulse train of 10 electric pulses of regular interval Δt was delivered to the tectal layer 2-4 and the responses of SGC-I somata were recorded (Figure 5.2A). Consistent with previous findings (Luksch et al., 2004; Khanbabaie et al., 2007), when driven by single pulses, SGC-I cells respond either with one to two action potentials or with small EPSPs. The SGC-I responses typically have high probability to pulse#1 in the stimulation train and the probability decayed to a lower value for the following up pulse #2-10 (Figure 5.2A). The bath application of mecamylamine greatly reduced the number

of action potentials in response to pulse #2-10 (Figure 5.2A). In few cases (3/10), the effect was washed out when normal ACSF was re-applied to the slice (Figure 5.2A) and the response recovered to the control condition. The shape of pulse-driven action potential was not altered with the application of mecamylamine (Figure 5.2B). To test whether the cellular properties of SGC-I cells were altered during the application of mecamylamine, we measured the response of SGC-I somata to both depolarizing and hyperpolarizing step current. No significant change was observed in the response before or after the application of mecamylamine (Figure 5.2C).

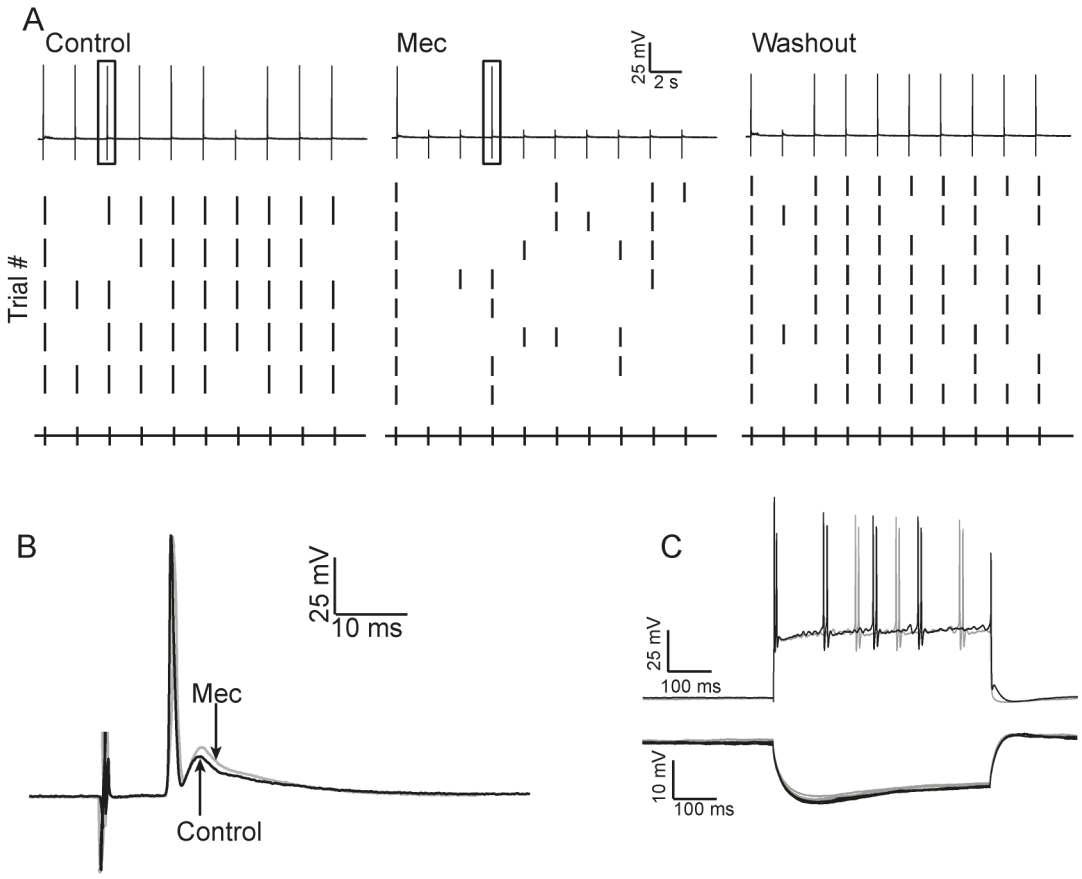

Figure 5.2 The responses of a SGC-I soma to sequential pulses. A, The response of a SGC-I cell to a sequence of 10 electrical pulses ($\Delta t = 2000$ ms). Top row, recorded membrane potential of the SGC-I neurons. The SGC-I cells typically had resting

membrane potential of -65 mV. Bottom row, rasters of the SGC-I response over multiple trials. Left, control condition. Middle, bath application of mecamylamine. Right, response after washout. B, Typical spike responses of a SGC-I cell (black box in A) are shown overlaid before (black) and after (gray) bath application mecamylamine. C, The cellular response of a SGC-I cell to depolarizing step current injection (top, I = 1.3 nA) and hyperpolarizing current injection (bottom, I = -0.1 nA). The response under control condition and mecamylamine is shown in black and gray, respectively.

The response probability of SGC-I cells depends on the pulse interval (Luksch et al., 2004; Khanbabaie et al., 2007). To further reveal the synaptic dynamics and the effect of ACh, we tested the retino-tectal synaptic transmission by using electro-stimulation of various pulse intervals (Figure 5.3A-J). The response probability is quantified by calculating the response probability P_i $(i = 1, 2...10)$ for each of the 10 stimulation pulses over multiple trials. For pulses of various intervals ($\Delta t = 500$ ms, 1000 ms, 1500 ms, 2000 ms, 4000 ms) the response probability of a SGC-I cell has a transient value P_1 close to 1 while triggered by the first pulse in the pulse train and the response probability P_{2-10} reaches to a steady state value when triggered by the following pulses #2-10 (Figure 5.3A-E). The steady-state response probability P_s is calculated by averaging over the response probabilities P_{2-10} (Figure 5.3F-J). After the application of mecamylamine, the response probability P_{2-10} was greatly reduced for the pulses of intervals $\Delta t = 1000$ ms 1500 ms, 2000 ms (Figure 5.3B-D) and the steady state response probabilities show highly significant changes (Figure 5.3G-I, paied t-test $p << 0.01$). The response probabilities P_{2-10} show relatively small changes for pulses of intervals $\Delta t = 500, 4000$ ms (Figure 5.3A, I) and the changes of steady state response (Figure 5.3F, J) are not

highly significant ($p = 0.61$, $p = 0.03$, respectively). The response probability to pulse #1 shows no significant change for all the pulse intervals tested ($p > 0.05$).

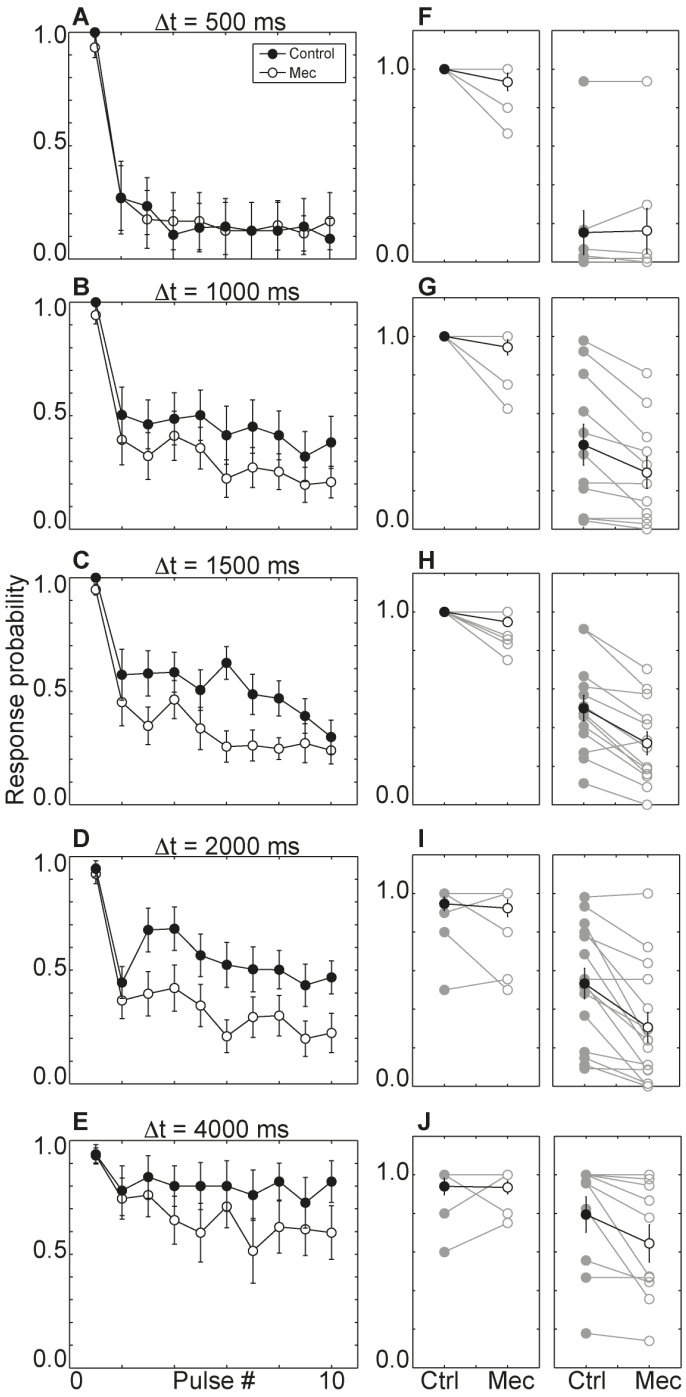

Figure 5.3 The response probability as a function of pulse No. A-E, The response probability of SGC-I cell as a function of pulse number. Various pulse intervals ($\Delta t = 500$ ms, 1000 ms, 1500 ms, 2000 ms, 4000 ms) were used to test the response

probability change before (black-circle line) and after (open-circle line) bath application of mecamylamine. The responses to pulse #2-10 show significant decrease after the bath application of mecamylamine for pulse intervals of $\Delta t = 1000$ ms, 1500 ms, 2000 ms. F-J, Left column: the response probability to pulse #1 The response for each individual cell is shown in gray, indicating the response probability before (filled circle) and after (open circle) the application of mecamylamine. The average responses of the population are shown in black, indicating the control (filled circle) and mecamylamine (open circle) conditions. Right column: the response probability of SGC-I cells to pulse #2-10.

The steady state response probability P_s is dependent on the stimulus intervals Δt in an exponential form of $P_s = P_{\max}(1 - e^{-\Delta t/\tau_0})$ (Figure 5.4A). The parameters of the formula are fitted to the experimental data. In the control condition, we have $P_{\max} = 0.87$ and $\tau_0 = 1888$ ms. Blocking nAChR greatly increases the recovery time constant $\tau_0 = 3596$ ms but the maximum response probability remains at a high value with $P_{\max} = 0.93$. The response probability varies greatly among the SGC-I population and results in a large deviation in the response. The percentile response change of the SGC-I cells provides a better way of showing the mecamylamine effects by minimizing the response variation across the SGC-I population (Figure. 5.4B).

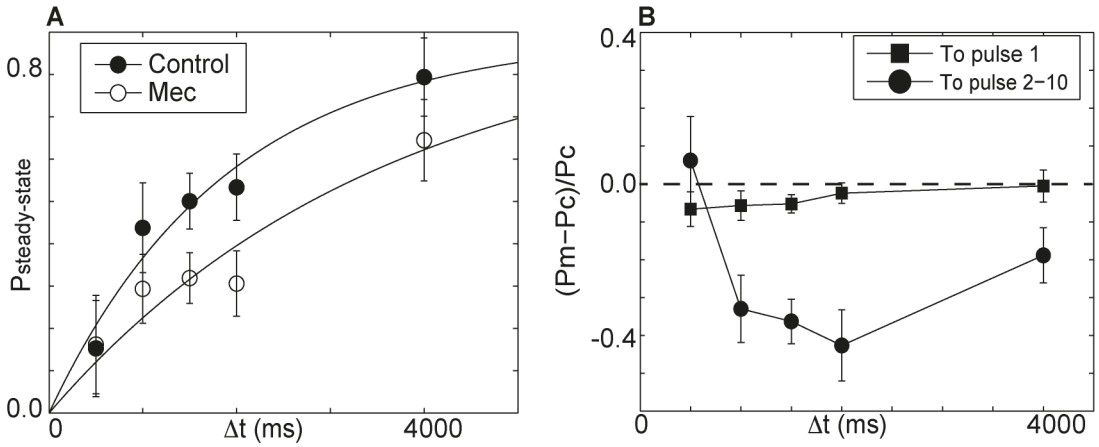

Figure 5.4 The steady-state responses of SGC-I neurons as a function of pulse intervals. A, The steady state response probability (to pulse #2-10) of a SGC-I cell as a function of

pulse interval. The steady response probability increases as the pulse interval increases. The response probability shows a significant decrease for pulse interval of $\Delta t = 1000, 1500, 2000$ ms with the application of mecamylamine (open circle), comparing to the control condition (black circle). B, The percentile change of response probability after the bath application of mecamylamine as a function of pulse interval. The response probability to pulse #1 shows little change (black square). In response to pulse #2-10, the percentile change increases as the pulse interval increases, peaking at $\Delta t = 2000$ ms and decreases as the pulse interval increases further.

5.4.2 Co-release of glutamate at Ipc axon terminals

Evidence is accumulating that Ipc neurons release glutamate (Wang et al., 1995; Wang, 2003; Gonzalez-Cabrera et al., 2011) in addition to the expected release of ACh(Medina and Reiner, 2004, Wang et al., 2006). To test whether Ipc axons interact with OT via glutamatergic neurotransmitter, we recorded intracellularly from the tectal neurons while stimulating the Ipc nucleus. Recorded tectal neurons respond with small EPSPs of amplitude ~3 mV to electric stimulations in Ipc nucleus (Figure 5.5A) and action potentials were occasionally evoked. The response was greatly reduced after bath application of CNQX (Figure 5.5A), indicating the involvement of glutamate in synaptic transmission. The EPSP peak is significantly reduced after bath application of CNQX (Figure 5.5B paired t-test, $p < 0.01$)

5.4.3 The model of retino-tecto-rotundal and isthmotectal pathway

In order to understand the role of Ipc feedback in motion processing, we constructed a computational model where both the retino-tecto-rotundal pathway and the isthmotectal feedback loop are considered (Figure 5.6A). The design of the model network is constrained by the available anatomical (Wang et al., 2004, 2006) and physiological information (Shao et al., 2009) of the OT and its nucleus. RGC neurons transfer visual

stimulus into Poisson spike train and activate the L10 neurons through topographic projections. The dendritic endings of SGC-I neurons follow cosine distribution (Figure 5.6B; Mahani et al., 2006) and are activated by the pulses generated at the corresponding RGC neuron. The topographic projections L10→Ipc, L10→Imc, and Ipc→L10 are represented by 2D Gaussian distributions. The RGC-SGC synapses are modulated by adjacent Ipc neurons whose RF is the closest. One individual Ipc axonal terminal can modulate multiple RGC-SGC synapses. The GABAergic Imc→L10 projection is represented by an inverted 2D Gaussian function and the synaptic weight of Imc→Ipc projection follows a uniform distribution.

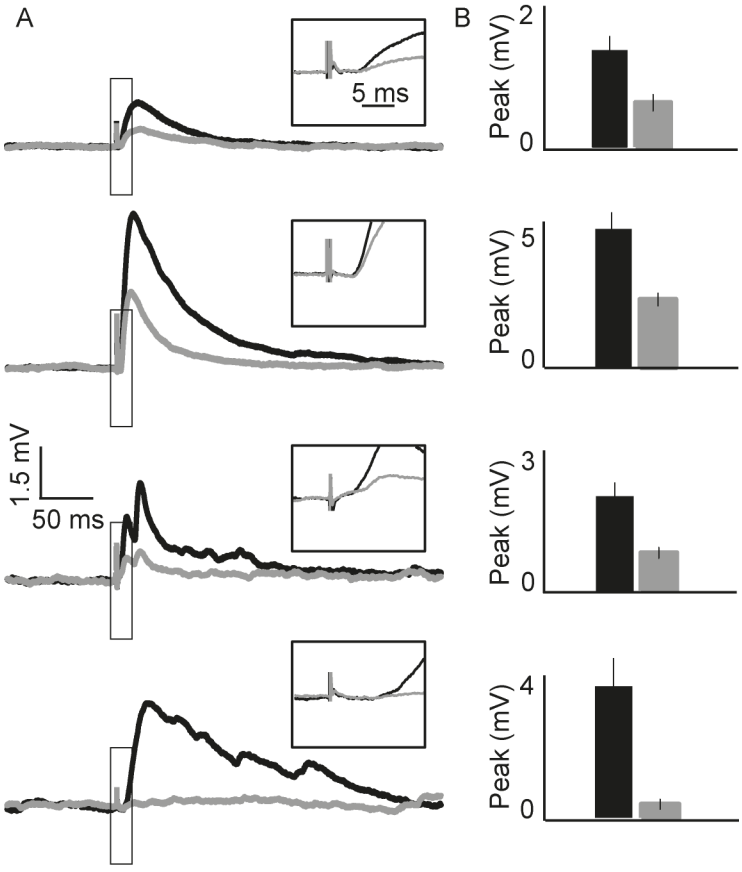

Figure 5.5 The response of tectal neurons to electric stimulations at the Ipc nucleus. A, The averaged EPSPs before (black line) and after (gray) bath application of CNQX. The

response shows a significant decrease with the application of CNQX. B, The amplitude of the EPSP before (black bar) and after (gray bar) the application of CNQX.

5.4.4 Divisive modulation of SGC-I response tuning curve

Divisive modulation, where the change of neural response is proportional to the neural activity, has been observed in various contexts (DeAngelis et al., 1994; Cavanough et al., 2002; McAdams and Maunsell, 1999; Treue and Martinez-Trujillo, 1999). The response of tectal neurons to looming stimuli is divisively attenuated in the presence of a competitor outside the receptive field (Mysore et al., 2010). Moreover, inactivation of Ipc neurons also results in divisive modulation on the tectal neuron response (Asadollahi and Knudsen, 2011). To understand the divisive modulatory effects, we activated the model network with single/multiple moving dots of various speeds and investigated the response change of SGC-I neurons with varying Ipc activity.

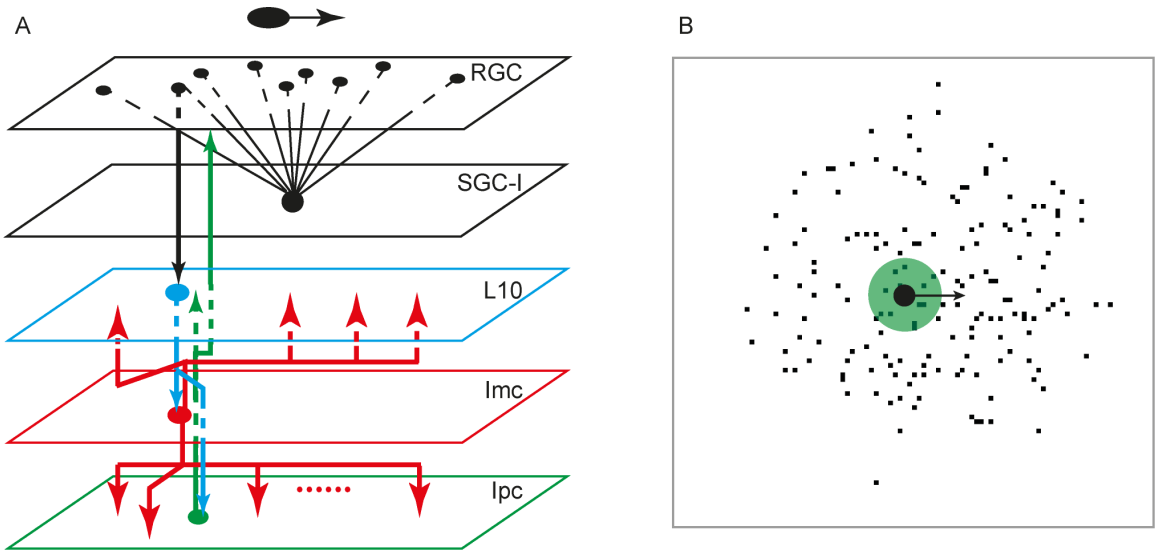

Figure 5.6 The architecture of the retino-tecto-rotundal and isthmotectal neural network. A, Five two-dimensional neuron arrays are used to represent the RGC, SGC-I, tectal L10, Ipc and Imc neuron groups. The stimulus is a moving dot modeled as a two dimensional Gaussian function. The SGC-I neuron has its dendritic endings distributed at the RGC layer following a cosine distribution. The projection from L10 to Ipc and Imc neurons

follows Gaussian distribution. The Ipc neurons project topographically to the L10 neurons with Gaussian distribution and feed back to the retino-tectal synapses with the most adjacent RF center. The Imc neurons send their inhibitory feedback broadly to the L10 and Ipc groups, with anti-topographic and homogeneous distribution respectively. B, The distribution of a SGC-I dendritic endings follows the shape of a cosine function. The green shade indicates the spatial extent of Ipc feedback from a single Ipc unit.

We consider the response of a SGC-I neuron by two components: the transient response and the steady-state response. Because of the high response probability, the transient component dominates the response of a SGC-I neuron (Mahani, 2006) and is proportional to the number n_d of dendritic endings on the trajectory of a moving dot (see methods). The response rate reaches a maximum when the stimulus is moving across the RF center of a SGC-I neuron where the distribution of dendrites has the highest density. The response decreases as the stimulus moves across the path away from the RF center, where the dendritic distribution has low density (Figure 5.7 A-D). The tuning curve of SGC-I neurons therefore follows a distribution close to a cosine function. On the other hand, within certain time interval T, the number of activated dendritic endings n_d increases as the speed of the stimulus increases and is approximately estimated as $r_{SGC} \sim \frac{n_d P_{\max}}{T}$. The firing rate of SGC-I neuron is therefore a monotonically increasing function of stimulus speed (Figure 5.7 A-D). Since the relevant parameter for SGC response rate is not altered by synaptic modulation, the transient response is not affected by Ipc feedback.

In contrast to the transient response, the steady state response has a much lower response probability that is proportional to $\sim \frac{P_{\max}}{\tau}$, provided a high RGC input rate. The response

rate is accordingly estimated as $\sim \frac{n_d T_D P_{\max}}{\tau T}$, assuming no refractory period (see methods), where T_D is the average duration within which a dendrite of the SGC-I neuron is exposed to the visual stimulus. The steady state response is dependent on Ipc activity since the recovery time constant τ varies with the release of ACh. In vitro observation indicates that blocking nAChRs prolongs the recovery time constant τ. The SGC-I somatic rate $r_{SGC} \sim \frac{n_d P_{\max}}{T}\left(1+\frac{T_D}{\tau}\right)$ decreases accordingly (Figure. 5.7A-D) without Ipc activity. With large recovery time constant τ, it follows that $\frac{T_D P_{\max}}{\tau} << 1$. Thus, the enhancement factor defined as the ratio between the SGC-I response rate with and without Ipc feedback has a form of $F_e \sim \left(1+\frac{T_D}{\tau}\right) / \left(1+\frac{T_D}{\tau_0}\right)$, where τ and τ_0 is the average value of the recovery time constant with and without the Ipc modulation, respectively. The enhancement factor is independent on dendritic distribution parameter n_d and is therefore constant over various stimulus locations (Figure 5.7E). The steady state response rate of a SGC-I neuron is also dependent on the parameter T_D, which is inversely proportional to the speed of a moving dot. A slow moving dot stays longer in the RF of a SGC-I dendrite (larger T_D) and the effect of acetylcholine is potentiated accordingly (Figure 5.7A-D). The enhancement factor therefore decreases as the stimulus speed increases (Figure 5.7F).

In the presence of multiple visual stimuli, the isthmotectal neural responses interact with each other through the global antitopographic feedback mediated by Imc axons. A salient

stimulus at a distal location suppresses the neural response triggered by a local stimulus through competition mechanisms (Lai et al., 2011). The suppressed activity of Ipc neurons reduced acetylcholine release at the postsynaptic RGC-SGC synapses. With the same mechanism described above, divisive modulation is observed (data not shown).

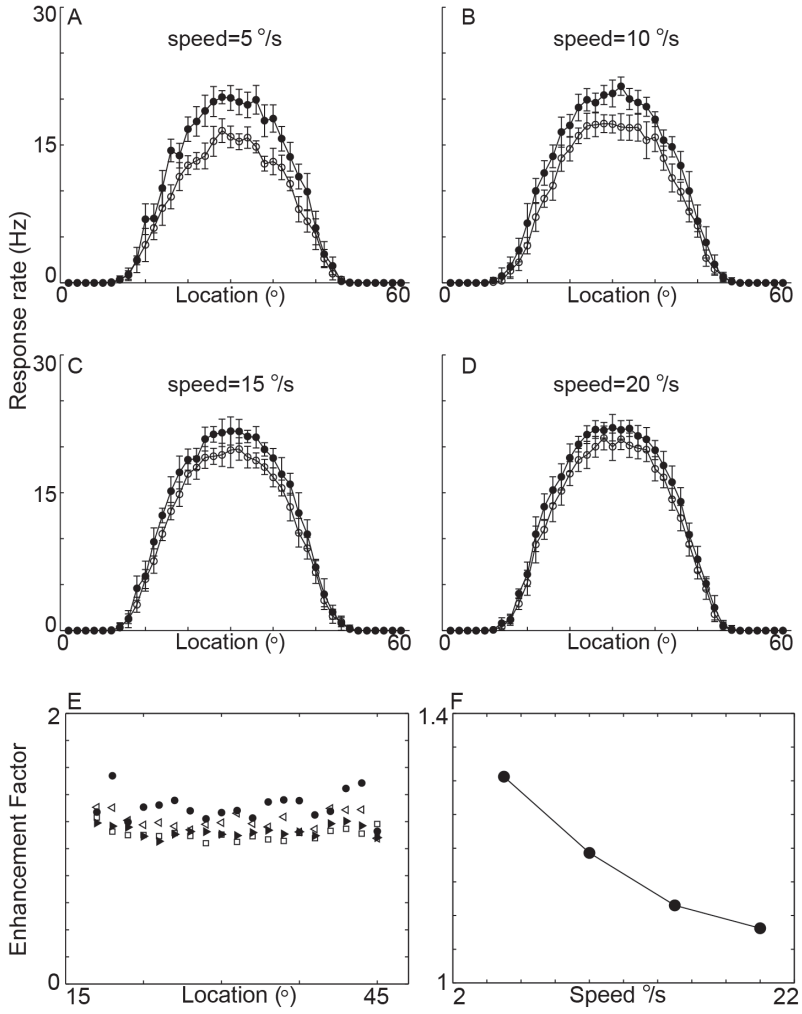

Figure 5.7 The response tuning curve to moving stimulus of different speed. The response rate is the average rate of the center 5 neurons at the center column (perpendicular to the direction of moving stimulus) of the simulated neuron sheet (over 10 trials, error bar indicates the SD). The stimulus size is chosen as $\sigma_s = 1.5°$ and the RGC layer has the size of $N_{RGC} = 100$. The projection parameters are chosen as $\sigma_{x,RGC\to L10} = \sigma_{y,RGC\to L10} = 3°$, $\sigma_{x,L10\to Ipc} = \sigma_{y,L10\to Ipc} = 3°$, $\sigma_{x,Ipc\to L10} = \sigma_{y,Ipc\to L10} = 5°$,

$\sigma_{x,\mathrm{Im}c\to L10} = \sigma_{y,\mathrm{Im}c\to L10} = 10°$, $D_{\mathrm{Im}c\to L10} = 1.0$, $D_{\mathrm{Im}c\to L10} = 0.0$. The dendritic parameters for the SGC-I cells are chosen as $P_{\max} = 0.9$, $\tau_0 = 2200$ ms. The modulatory parameters for the cholinergic feedback is chosen as $\varepsilon = 1.0$, $\tau_\beta = 200$ ms, The glutamatergic modulation is not considered here $p_{Glu} = 0.0$. A, speed = 5 °/s The tuning curve (black-dot line) is divisively attenuated when the Ipc units are inactivated (open-dot line) B, C, D, Tuning curve in response to stimulus of speed = 10 °/s, 15 °/s, 20 °/s. E. The enhancement factor is calculated at each stimulus location by taking the ratio between the SGC-I response with/without the Ipc modulation. The factor appears to be constant over different stimulus locations. F the average enhancement factor is calculated by taking the ratio between the average response rate with/without Ipc modulation.

5.4.5 The role of Ipc in modulating correlated activities of SGC-I population

The axonal endings of Ipc neurons terminate densely at the retinorecipient layer, overlaps spatially with the dendritic endings of numerous SGC-I neurons. It has been proposed that the axons of Ipc neurons might serve to coordinate the activity across the SGC-I population through this localized projection (Wang et al., 2006). Here we quantitatively examine the hypothesis by analyzing the cross-correlations among the SGC-I population. We activate the model network with a moving dot that starts at the RF center. The cross-correlation matrix is calculated between the neurons at the center column of the SGC-I grids. The direction of the moving dot is perpendicular to the considered SGC-I neuron column. Without Ipc feedback, the SGC-I neurons respond largely independent to uncorrelated RGC Poisson spike inputs (Figure 5.8A). We then tested the response correlations of the SGC-I population with two types of Ipc modulation. Firstly, we modeled the Ipc feedback as solely cholinergic. The activity of Ipc neurons leads to the release of acetylcholine, which shortens the recovery speed of the synaptic depression at the retino-tectal projections (see methods). The response rate of the SGC-I cells increases due to the Ipc modulation (Figure 5.8C) but little correlation is observed (Figure 5.8D).

Perhaps surprisingly, the simultaneous modulation of the wide field SGC-I cells by the local Ipc axons introduces little correlation in the population activity. The low steady-state response probability and small number of common RGC inputs shared by any two SGC-I cells are the major reasons that cause the low correlation. This issue is discussed in details in the following section.

We then tested an alternative model assuming the cotransmission of acetylcholine and glutamate from Ipc. In general, glutamate is an effective excitatory neurotransmitter that can evoke depolarization and action potentials at the postsynaptic neurons. Here, we assume the activity of Ipc axons will stochastically activate the spikes of SGC-I dendrites. When a moving dot enters the RF of Ipc neurons, it triggers the Ipc neurons to respond with rhythmic bursting (Figure 5.8E), the mechanisms of which were discussed previously (Shao et al., 2009; Lai et al., 2011). The spikes of Ipc neurons now locally activate the spiking response of SGC-I dendrites. Rhythmic responses are observed in the SGC-I populations and the frequency of the activity is tuned to the frequency of Ipc bursts (Figure 5.8E). Two mechanisms contribute to the correlation. First, the local Ipc axons excite multiple SGC-I cells with a relatively high probability through their contacting with SGC-Is' wide distributed dendrites. Second, the recurrent excitation and inhibition between the L10 and Imc neurons evoke correlated oscillatory activities among the Ipc population (Figure 5.8E), which imposes correlated inputs to the SGC-I population. The correlations between SGC-I neurons are therefore enhanced by Ipc feedback. Detailed discussion is shown in the following section.

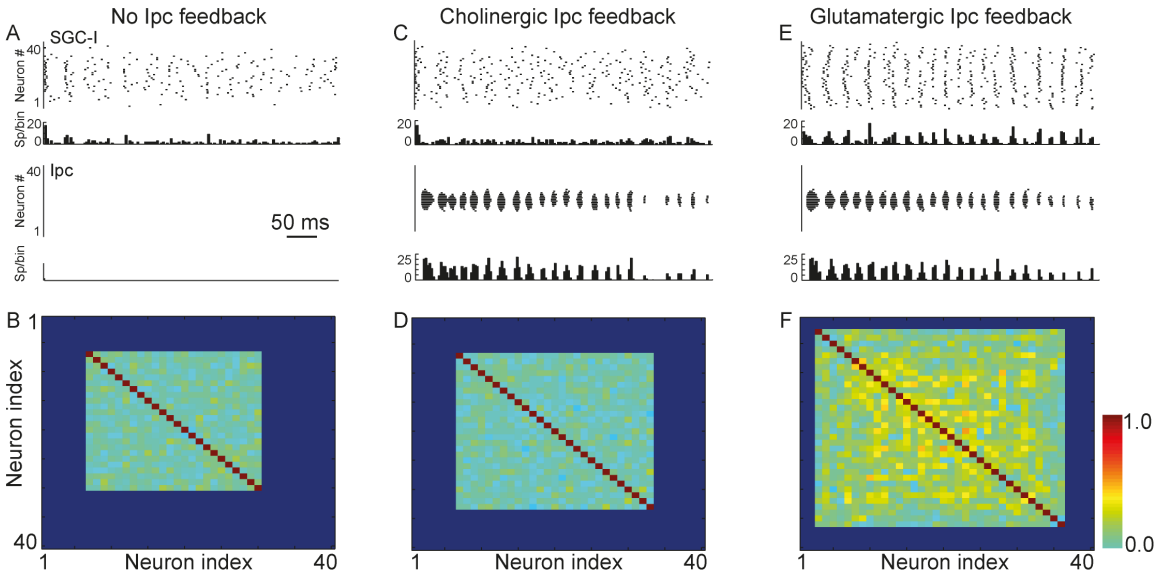

Figure 5.8 The cross-correlations of SGC-I population in response to moving stimuli. A, Raster of SGC-I neurons spiking activity in response to a moving stimulus without Ipc activity. The histogram is shown below the raster plots. The raster shows SGC-I activity at the center column of the neuron grids with the spot moving perpendicular to the column B, The cross-correlation matrix between the SGC-I neurons. The color is coded in a way where green indicate a low correlation close to 0 while red indicates a high correlation close to 1. C, Raster of SGC-I neurons and Ipc neurons in response to a moving stimulus with cholinergic feedback from Ipc. Histogram is shown below the raster plots of both neural group. No significant correlation is observed with the cholinergic modulation of SGC-I responses. The neural response decreases as the stimulus moves out of the RF of the Ipc neurons. D, The cross-correlation matrix between the SGC-I neurons. E, Raster of SGC-I neurons in response to a moving stimulus with glutamatergic feedback from Ipc. F, The cross-correlation matrix between the SGC-I neurons.

5.4.6 Analysis of the cross-correlation between two SGC-I cells

The cross-correlation between two SGC-I neurons has two components, resulting from transient response and steady-state response and the formula follows as $\rho_{ij} \approx \frac{\mathrm{cov}(m_{o,i}, m_{o,j}) + \mathrm{cov}(m_{s,i}, m_{s,j})}{\mathrm{var}(m_o) + \mathrm{var}(m_s)}$, assuming that $\mathrm{var}(m_o) = \mathrm{var}(m_{o,i}) = \mathrm{var}(m_{o,j})$. Here m_o and m_s is the spike counts with in a time window of certain length T_w. The steady

state term in the cross-correlation coefficient $\mathrm{cov}(m_{o,i}, m_{o,j}) = p_s^2 n_c r_{RGC} T_w$ and $\mathrm{var}(m_s) = p_s n_c r_{RGC} T_w$ are negligible comparing to the transient terms due to the low response probability $p_s << 1$ with or without Ipc feedback and small number of dendritic endings that share common RGC input $n_c << 1$, because of the sparse distribution.

To understand the correlation in the SGC population activity with the modulation of glutamate, we analytically calculated the cross-correlation coefficient between two SGC-I neurons that have a constant response probability p to RGC pulses. The cross-correlation coefficient between two SGC-I neurons is of the form $\rho_{ij} = p n_c / (n_s + n_c)$ (see Methods), where n_c is the number of dendrites that receive common RGC input and n_s is the number of dendrites that receive independent RGC input. Two major properties positively affect the response correlation between two SGC-I neurons. Firstly, the response probability p to the triggering spikes and secondly the number of dendrites n_c that shares common inputs from RGC axons. When all dendrites of the two SGC-I neurons share the same RGC inputs $n_s = 0$, the cross correlation is solely dependent on the response probability $\rho_{ij} \sim p$. The responses of the two SGC-I neurons are identical when $p \sim 1$, and accordingly the cross correlation follows $\rho_{ij} \sim 1$. On the other hand, when $n_c \sim 0$, the response of the two SGC-I neurons are independent and the cross correlation becomes $\rho_{ij} \sim 0$. In the presence of glutamatergic Ipc feedback, we assume that the spikes of Ipc neurons will cause spikes at the corresponding SGC-I dendritic endings with a response probability p_{Glu}. Moreover, the correlated activity of Ipc axons

effectively increases the number of dendrites n_c that shares the same pulse stimulations between two SGC-I neurons. The bursting activity of Ipc neurons together with the relatively large response probability p_{Glu} leads to the strong correlated activity of the SGC-I population.

5.5 Discussion

5.5.1 Cotransmission of ACh and glutamate from Ipc axons

Immunochemistry study indicates that Ipc contains cholinergic neurons (Medina and Reiner, 2004) and the isthmic structure has long been referred as cholinergic (Wang et al., 2006). However, recent studies found expression of mRNA for the vesicular glutamate transporter 2 in Ipc neurons (Gonzalez-Cabrera et al., 2011). Electrophysiological recordings also suggest that the Ipc-tectal projection could make use of two neurotransmitter systems, glutamate and acetylcholine (Wang et al., 1995; Wang, 2003). Here we show that the dynamics of retino-tectal synaptic transmission are regulated by nAChRs (Figure. 5.2, 5.3). We also recorded EPSPs/action potentials at postsynaptic tectal neurons while delivering electric stimulations at Ipc nucleus. The reduced response after bath application of CNQX suggests the involvement of glutamate in synaptic transmission (Figure 5.5). However, L10 axons also send collateral projections within the OT (Wang et al., 2006). Therefore, the possibility of that the recorded response change is resulted from the antidromic stimulation of glutamatergic L10 axons can not be excluded in this study. Interestingly, co-release of multiple neurotransmitters from the same axon terminal has been found common in mammalian center nervous system (Lu et al., 2008;

Chuhma et al., 2004). The idea once controversial to Dale's principle is now well established (Seal and Edwards, 2006).

5.5.2 The regulating mechanisms of nAChR on synaptic depression

Acetylcholine (ACh) is involved in multiple stages of visual processing (Yazejian and Fain, 1993; Endo et al., 2005) as well as cognitive functions such as attention, learning and memory (Mirza and Stolerman, 1998; Miranda and Bermudez-Rattoni, 1999; Levin and Torry, 1996; Hasselmo and Barkai, 1995). Although a wealth of data has been collected on the effect of postsynaptic ACh release (McCormick, 1993; Metherate, 2004; Lucas-Meunier et al. 2003, 2009), a functional interpretation of the ACh is still missing due to complex innervation of ACh synapses.

The decaying response of SGC-I cells to a sequence of electrical stimulations at the retinal fibers suggests the involvement of short-term synaptic depression (Luksch et al., 2004). This study reveals that the blockade of nAChR slows the recovery speed of synaptic depression. Ligand-gated ion channels formed from nAChRs are permeable to $[Ca^{2+}]/[Na^{+}]$ ions (Mulle et al., 1992) and its activation/inactivation can cause changes of intracellular $[Ca^{2+}]$ concentration. The residual $[Ca^{2+}]$ model (Pyle et al., 2000; Zucker and Regehr, 2002) provides us with one of many mechanistic interpretations of the electrophysiology data. Mechanisms of short-term synaptic plasticity vary from vesicle depletion to glial neuronal interactions and involve the use of $[Ca^{2+}]$ ions (Zucker and Regehr, 2002). Synaptic depression typically recovers with a time constant of a few seconds and is thought as a result of the depletion of releasable neurotransmitter pool at

the presynaptic side. The recovery speed of synaptic depression is dependent on the concentration of intracellular residual [Ca^{2+}] (Dittman and Regehr, 1998). The increment of residual [Ca^{2+}] will enhance the rate of refilling the releasable pool and thus potentiates the recovery of synaptic depression (Wang and Kaczmarek, 1998). Perhaps, under the experimental condition the blockade of nAChR leads to a decrement in the intracellular [Ca^{2+}] concentration and the refilling rate of the releasable neurotransmitter pool is accordingly reduced. As a result, the synaptic recovery time constant is prolonged.

5.5.3 Cholinergic feedback mediates divisive gain modulation

Divisive gain modulation is described in various contexts, including center-surround suppression (DeAngelis et al., 1994; Cavanough et al., 2002), attention enhancement (McAdams and Maunsell, 1999; Treue and Martinez-Trujillo, 1999) and competitive stimulus selection (Asadollahi et al., 2011; Mysore et al., 2010). Mechanisms such as voltage-dependent inhibition (Doiron et al., 2000) and synaptic noise (Ayaz and Chance, 2009) are thought to subserve the divisive response change.

In response to moving stimuli, the tuning curve of tectal neuron is divisively attenuated with local inactivation of Ipc units (Asadollahi and Knudsen, 2011) or with the presence of a competitor outside the RF (Mysore et al., 2010). The computational model suggests that the two observations could be mediated by the same underlying mechanism and the activity of Ipc feedback might be the key block that accounts for both phenomena. The tuning curve of a SGC-I cell follows from its dendritic distribution and the somatic response rate is proportional to the dendritic density at the stimulus location. The release

of acetylcholine from local Ipc neurons enhances the steady state response of a SGC-I soma and the enhancement is also proportional to the dendritic density. The suppression of the local Ipc activity, either through winner-take-all mechanism or through drug application, lead to the decreasing of tectal neural activity. The 'divisive inhibition' is therefore a phenomenon that results from synaptic dynamics as well as cellular morphology.

5.5.4 The role of Ipc feedback in modulating coherent activity of SGC-I population

The release of ACh regulates signal transmission between or within hierarchical levels in visual pathway (McCormick, 1988; Lucas-Meunier et al., 2009) and is involved in coherent neural activity, e.g. rhythmic oscillation, synchronization (Steriade, 2003; Rodriguez et al., 2004; Dickson et al., 2000). ACh shows a mixed role in regulating the coherence of neural response. *In vivo* stimulation of cholinergic nucleus basalis shift cortical neuron response from phasic to tonic (Metherate et al., 1992) while intracortical application of cholinergic agonist could also enhance the synchronization of Gamma oscillation (Rodriguez et al., 2004). *In vitro* recordings and model investigation illustrates that ACh could desynchronize cortical electroencephalogram by reducing the rate of synaptic depression (Tsodyks and Markram, 1997).

The cholinergic modulation from Ipc neurons enhances the steady state response rate but it contributes little to the cross correlation between SGC-I cells (Figure 5.8B). We demonstrated in a probabilistic model that the overlap between SGC-I dendrites could lead to correlated activities between two SGC-I neurons and the cross-correlation

increases with higher dendritic response probability. A large RGC projection field or a dense distribution of SGC-I dendrites could increase the overlaps of between SGC-I dendrites. However, morphological data suggests a sparse distribution of SGC-I dendrites (Mahani et al., 2006) and narrow radial arbors of retinal axons (Karten et al., 1997). The morphologically constrained network shows little correlated activities in the SGC-I population (Figure. 5.8B).

The model investigation reveals that the cholinergic feedback alone is not sufficient to account for the observed synchrony between Ipc and higher visual areas activities (rotundus, entopallium, Marin et al., 2012). By assuming that Ipc neurons trigger spikes at SGC-I dendrites, our model provides two interesting predictions. Firstly, the correlated bursting of Ipc neurons, generated via the isthmotectal interactions, synchronizes the activity of SGC-I neurons through its columnar feedback. The widely arborized SGC-I dendrites cause correlated activities across a large SGC-I population. Secondly, the Ipc-induced correlated activity ensures the stable information propagation through multiple stages along the visual pathway. Indeed, the bursting activities of Ipc neurons are critical in controlling the ascending visual signals. Blocking the Ipc activity either by a competitor or local CNQX application leads to suppressed activities of rotundus and entopallium (Marine et al., 2007, 2012). The model provides physiological understanding for the gating mechanisms and suggested the importance of glutamate in generating correlated activity in OT.

5.6 Reference

Ayaz A and Chance FS (2009) Gain modulation of neuronal responses by subtractive and divisive mechanisms of inhibition. J Neurophysiol 101:958-968

Abbott LF, Varela JA, Sen KV, Nelson SB (1997) Synaptic depression and cortical gain control. Science 275:220-224.

Asadollahi A, Mysore SP, Knudsen EI (2011) Rules of competitive stimulus selection in a cholinergic isthmic nucleus of the owl midbrain. J Neurosci 31:6088-6097.

Asadollahi A, Mysore SP, Knudsen EI (2010) Stimulus-driven competition in a cholinergic midbrain nucleus. Nat Neurosci 13:889-895.

Asadollahi A, Knudsen EI (2011) Cholinergic enhancement of visual representation in the owl optic tectum. SfN meeting. Poster: 197.16.

Anderson CH, Van Essen DC, Olshausen, BA (2005) Directed visual attention and the dynamic control of information flow. In: Neurobiology of Attention (Itti L, Rees G, Tsotsos J), pp. 11-17. San Diego: Elsevier.

Bruce Y and Gordon LF (1993) Whole-cell currents activated at nicotinic acetylcholine receptors on ganglion cells isolated from goldfish retina. Visual Neuroscience 10:353-361.

Cavanaugh JR, Bair W, Movshon JA (2002) Selectivity and spatial distribution of signals from the receptive field surround in macaque V1 neurons. J Neurophysiol 88:2547-2556.

Chuhma N, Zhang H, Masson J, Zhuang X, Sulzer D, Hen R, Rayport S (2004) Dopamine neurons mediate a fast excitatory signal via their glutamatergic synapses. J Neurosci 24:972-981.

Doiron B, Longtin A, Berman N, Maler L (2000) Subtractive and divisive inhibition: effect of voltage-dependent inhibitory conductances and noise. Neural Computation 13:227–248

Diesmann M, Gewaltig MO Aertsen A (1999) Stable propagation of synchronous spiking in cortical neural networks. Nature 402:529-533.

Dittman JS and Regehr WG (1998) Calcium dependence and recovery kinetics of presynaptic depression at the climbing fiber to purkinje cell synapse. J Neurosci 18:6147-6162.

DeAngelis GC, Freeman RD, Ohzawa I (1994) Length and width tuning of neurons in the cat's primary visual cortex. J Neurophysiol 71:347-374.

Dickson CT, Biella G, Curtis MD (2000) Evidence for spatial modules mediated by temporal synchronization of carbachol-induced gamma rhythm in medial entorhinal cortex. J Neurosci 20:7846-7854.

Endo T, Yanagawa Y, Obata K and Isa T (2005) Nicotinic acetylcholine receptor subtypes involved in facilitation of GABAergic inhibition in mouse superficial superior colliculus. J Neurophysiol 94:3893-3902.

Frost BJ and Nakayama K (1983) Signal visual neurons code opposing motion independent of direction. Science 220:744-745.

Fedorov NB, Benson LC, Graef J, Lippiello PM, and Bencherif M (2009) differential pharmacologies of mecamylamine enantiomers: positive allosteric modulation and noncompetitive inhibition. The Journal of Pharmacology and Experimental Therapeutics 328:525–532

Fries P, Reynolds JH, Rorie AE, Desimone R (2001) Modulation of oscillatory neuronal synchronization by selective visual attention. Science 291:1560-1563.

Ge S and Dani JA (2005), Nicotinic acetylcholine receptors at glutamate synapses facilitate long-term depression and potentiation. J Neurosci 25:6084-6091.

Gonzalez-Cabrera CA, Roth A, Marin GJ (2011) Glutamatergic and cholinergic phenotype of Ipc neurons. VGLUT2,CHAT and CHT1 mRNA expression in the chicken isthmo-tectal system. SfN poster:37.19.

Hasselmo ME, Barkai Edi (1995) Cholinergic modulation of activity-dependent synaptic plasticity in the piriform cortex and associative memory function in a network biophysical simulation. J Neurosci 15:6592-6604.

Ito M, Gilbert CD (1999) Attention Modulates contextual influences in the primary visual cortex of alert monkeys. Neuron 22:593-604.

Koch C, Ullman S (1985) Shifts in selective visual attention: towards the underlying neural circuitry. Human Neurobiol (1985) 4:219-227.

Knudsen EI (2007) Fundamental components of attention. Annu Rev Neurosci 30:57-78.

Knudsen EI (2011) Control from below: the role of a midbrain network in spatial attention. European Journal of Neuroscience. 33:1961-1972.

Karten HJ, Cox K, Mpodozis J (1997) Two distinct populations of tectal neurons have unique connections within the retinotectorotundal pathway of the pigeon (Columbia livia). J Comp Neurol 387:449-465.

Khanbabaie R, Mahani AS and Wessel R (2007) Contextual interaction of GABAergic circuitry with dynamic synapses. J Neurophysiol 97:2802-2811.

Lucas-Meunier E, Monier C, Amar M, Baux G, Fregnac Y, Fossier Philippe (2009) Involvement of nicotinic and muscarinic receptors in the endogenous cholinergic modulation of the balance between excitation and inhibition in the young rat visual cortex. Cerebral Cortex 19:2411-2427.

Luksch H, Khanbabaie R and Wessel R (2004) Synaptic dynaics mediate sensitivity to motion independent of stimulus details. Nat Neurosci 7:380-388.

Luksch H, Cox K, Karten HJ (1998) Bottlebrush dendritic endings and large dendritic fields: motion-detecting neurons in the tectofugal pathway. J Comp Neurol 396:399-414.

Lai D, Brandt S, Luksch H, Wessel R (2011) Recurrent antitopographic inhibition mediates competitive stimulus selection in an attention network. J Neurophysiol 105:793-805.

Levin ED, Torry D. (1996) Acute and chronic nicotine effects on working memory in aged rats. Psychopharmacology 123:88-97.

Lu T, Rubio ME, Trussell LO (2008) Glycinergic transmission Shaped by the corelease of GABA in a mammalian auditory synapse. Neuron 57:524-535.

Mahani AS, Khanbabaie R, Luksch H, Wessel R (2006) Sparse spatial sampling for the computation of motion in multiple stages. Biol Cybern 94:276-287.

McGaughy J, Everitt BJ, Robbins TW, Sarter M (2000) The role of cortical cholinergic afferent projections in cognition: impact of new selective immunotoxins. Behavioral Brain Res 115:251-263.

Miranda MI, Bermudez-Rattoni F (1999) Reversible inactivation of the nucleus basalis magnocellularis induces disruption of cortical acetylcholine release and acquisition, but not retrieval, of aversive memories. Proc Natl Acad Sci 96:6478-6482.

Mirza NR, Stolerman IP (1998) Nicotine enhances sustained attention in the rat under specific task conditions. Psychopharmacology 138:266-274.

Marin G, Letelier JC, Henny P, Sentis E, Farfan G, Fredes F, Pohl N, Karten H, Mpodozis J (2003) Spatial organization of the pigeon tectorotundal pathway: an interdigitating topographic arrangement. J Comp Neurol 458:361-380.

Marin G, Salas C, Sentis E, Rojas X, Letelier JC, Mpodozis J (2007) A cholinergic gating mechanism controlled by competitive interactions in the optic tectum of the pigeon. J Neurosci 27:8112-8121.

Mysore SP, Asadollahi A, Knudsen EI (2010) Global inhibition and stimulus competition in the owl optic tectum. J Neurosci 30: 1727–1738.

Metherate R, Cox CL, Ashe JH (1992) Cellular bases of neocortical activation: modulation of neural oscillations by the nucleus basalis and endogenous acetylcholine. J Neurosci 12:4701-4711.

Medina DL, Reiner A (2004) Distribution of choline acetyltransferase immunoreactivity in the pigeon brain. J Comp Neurol 343:497-537.

McAdams, CJ and Maunsell, JHR (1999) Effects of attention on orientation tuning functions of single neurons in macaque cortical area V4. J Neurosci 19:431–441.

Mulle C, Choquet D, Korn H, Changeux JP (1992) Calcium influx through nicotinic receptor in rat central neurons: its relevance to cellular regulation. Neuron 8:135-143.

MAUNSELL, JHR and Treue, S (2006) Feature-based attention in visual cortex. Trends in Neuroscience 29:317–322.

Nakauchi S, Brennan RJ, Boulter J, Sumikawa K (2007) Nicotine gates long-term potentiation in the hippocampal CA1 region via the activation of α2* nicotinic Ach receptors. European Journal of Neuroscience 25:2666–2681

Olshausen BA, Anderson CH, Van Essen DC (1993) A neurobiological model of visual attention and invariant pattern recognition based on dynamic routing of information. J Neurosci 13:4700-4719

Pyle JL, Kavalali ET, Piedras-Renteria ES, Tsien RW (2000) Rapid reuse of readily releasable pool vesicles at hippocam-pal synapses. Neuron 28:221–31.

Reynolds JH, Chelazzi L, Desimone R (1999) Competitive mechanisms subserve attention in macaque areas V2 and V4. J Neurosci 19:1736–1753

Rodriguez R, Kallenbach U, Singer W, Munk MHJ (2004) Short-and long-term effects of cholinergic modulation on gamma oscillations and response synchronization in the visual cortex. J Neurosci 24:10369-10378.

Steriade M (2004) Acetylcholine systems and rhythmic activities during the waking-sleep cycle. Prog Brain Res 145:179–196.

Seal RP and Edwards RH (2006) Functional implications of neurotransmitter co-release: glutamate and GABA share the load. Current Opinion in Pharmacology 6:114-119.

Shao J, Lai D, Meyer U, Luksch H, Wessel R (2009) Generating oscillatory bursts from a network of regular spiking neurons without inhibition. J Comput Neurosci 27:591–606

Treue, S, and Martinez-Trujillo, JC (1999) Feature-based attention influences motion processing gain in macaque visual cortex. Nature 399:575–579.

Tsodyks MV and Markram H (1997) The neural code between neocortical pyramidal neurons depends on neurotransmitter release probability. Proc Natl Acad Sci 94:719–723.

Yan K and Wang SR (1986) Visual responses of neurons in the avian nucleus isthmi. Neurosci Lett 64:340-344.

Wang SR, Wu GY, Felix D (1995) Avian Imc-tectal projection is mediated by acetylcholine and glutamate. NeuroReport 6:757-760.

Wang SR (2003) The nucleus isthmi and dual modulation of the receptive field of tectal neurons in non-mammals. Brain Research Reviews 41:13–25.

Wang Y, Major DE, Karten H (2004) Morphology and connections of nucleus isthmi pars magnocellularis in chicks (Gallus gallus) J Comp Neurol 469:275-297.

Wang Y, Luksch H, Brecha NC, Karten HJ (2006) Columnar projections from the cholinergic nucleus isthmi to the optic tectum in chicks (Gallus gallus): a possible substrate for synchronizing tectal channels. J Comp Neurol 494:7-35.

Wang LY, Kaczmarek LF (1998). High-frequency firing helps replenish the readily releasable pool of synaptic vesicles. Nature 394:384-88.

Wang YC, Frost BJ (1991). Visual response characteristics of neurons in the nucleus isthmi magnocellularis and nucleus isthmi parvocellularis of pigeons. Exp Brain Res 87(3):624-33.

Yazejian B, Fain GL (1993) Whole-cell currents activated at nicotinic acetylcholine receptors on ganglion cells isolated from goldfish retina. Visual Neurosci 10: 353-361.

Zucker RS and Regehr WG (2002) Short-term synaptic plasticity. Annu Rev Physiol 64:355-405.

6 The dynamics of novelty preference in a competitive neural network with adaptation

In this chapter we consider a network that consists of two mutually inhibitory neurons with intrinsic adaptation regulation. We illustrate that the network is capable of competitively selecting multiple stimuli through winner-take-all (WTA) or novelty preference mechanisms. A reduced two-dimensional system is sufficient to reproduce the WTA activity of the full system while a 3-dimensional system is probably a minimum requirement to replicate the novelty preference behavior. We also discuss the role of connectivity strength and adaptation in determining the system's dynamics.

6.1 Introduction

To survive the complex environment, an animal has to choose from an enormous set of events and respond with most relevant course of action. To accomplish a task, competitive mechanisms are triggered while multiple stimuli are presented (Reynold et al., 1999; VanRullen and Koch, 2003). The representative neural activities corresponding to the stimuli might either be attenuated or enhanced through competitive mechanisms in a bottom-up or top-down manner (Knudsen, 2007). The modulatory effects of neural response also depend on the environmental context as well as the internal states of the animal (Reynolds and Heeger, 2009; Knudsen, 2007). However, the dynamics of competitive interaction in neural network are poorly understood (Rabinovich et al., 2008).

The WTA network has been thought as a mechanism to subserve competitive stimulus selections (Koch and Ullman, 1985). Lateral inhibition, an anatomical structure that could imply a WTA mechanism, has been found in multiple regions along the visual pathway from the retina to the visual cortex (Troy and Shou, 2002; Chisum and Fitzpatrick 2004). Prominent long-range inhibitory connections have been found in a midbrain structure: optic tectum (OT) and its isthmic nucleus (Wang et al., 2004), which is thought to involve in attentional control (Knudsen, 2011). So far, most discussions on the WTA mechanisms have been focused on the connection strengths between network neurons (Mao and Massaquoi, 2007). However, neurons as well as their synapses are adaptive units whose activities are dependent on the response history (Kohn, 2007). Adaptive responses, such as novelty detection are also found on a macroscopic level (Tiitinen et al., 1994; Aston-Jones, 1999).

In the following sections, we investigate the dynamics of competitive stimulus selection mechanisms by considering a two-neuron system with adaptation. We discuss the dynamic of the network by representing two types of competing stimuli. In the static scenario, two stimuli are presented simultaneously to the network while in the dynamic scenario, the stimuli are presented in sequence. The stability and bifurcation of the network is dependent on the parameters associated with inhibition strength and neural adaptation.

6.2 A competitive network with adaptation

To understand the dynamics of competitive stimulus selection, we compose a two-neuron network with reciprocal inhibition. The activities of model neurons are described by its firing rate $r_i(t)$ and the dynamics of the networks evolve according to the differential equation set

$$\begin{cases} \tau_r \dfrac{dr_i}{dt} = -r_i + \Lambda(s_i - I_{a,i} - \sum_{i \neq j} w_{ij} r_j) \\ \tau_a \dfrac{dI_{a,i}}{dt} = -I_{a,i} + A r_i \end{cases} \qquad i = 1, 2$$

where τ_r is the time constant of the firing rate. $\Lambda(x)$ is an activation function that transfers various neural stimulation into neural activity and is chosen as a rectified Hill's function with the properties that $\Lambda(x) = \dfrac{x^a}{(b^a + x^a)}$ if $x > 0$, and $\Lambda(x) = 0$ if $x \leq 0$, $a, b > 0$. It follows directly that the derivative of the activation function is $\Lambda'(x) = \dfrac{ab^a x^{a-1}}{(b^a + x^a)^2}$ if $x > 0$ and $\Lambda'(x) = 0$ if $x \leq 0$. s_i is the external stimulus triggered at the presence of an object. $I_{a,i}$ is the adaptation current that modulates the neural activity and is determined by the firing rate of the neuron. The negative sign indicates that the adaptation currents tend to reduce the neural activity. Weight matrix w_{ij} describes the strength of neural connections. If we assume a symmetric mutual inhibitory connection we have the weight matrix of the form $w_{ij} = \begin{pmatrix} 0 & w \\ w & 0 \end{pmatrix}$ and $w > 0$. The zero diagonal terms indicate that neurons do not synapse onto themselves.

6.3 WTA and novelty preference in the 4-dimensional system

While simultaneously presented with stimuli of different strength, a WTA mechanism could be triggered and the network could choose between two stimuli the strongest one (Fig. 6.1a). At the stimuli onset, both neuron 1 and 2 are excited. Due to the difference in stimuli intensity, the activity of neuron 2 increases slightly faster than neuron 1. The activity of neuron 2 then starts to suppress that of neuron 1 and eventually become the winner of the competition. In this situation, the network behaves as a maxima selector and only the neuron corresponding to the maximum stimulus is activated.

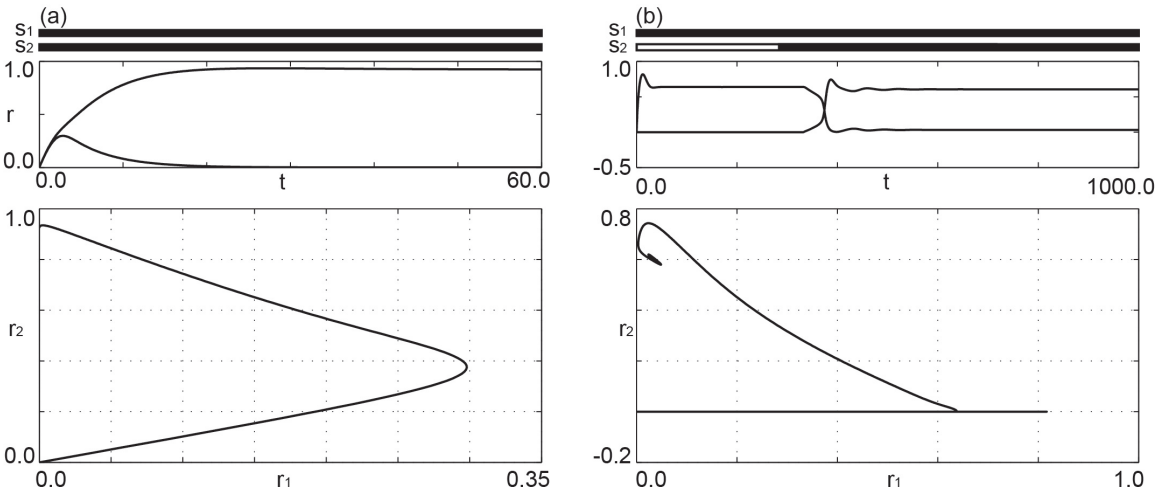

Figure 6.1: The response of the neural network to static and dynamic visual scenes. (a) Two stimuli $s_1 = 1.0$ and $s_2 = 1.1$ are delivered to neuron 1 and 2 simultaneously at $s_1 = 0.0$ (the time course is shown in black bar). The parameters are chosen as $A = 0.3$, $b = 0.5$, $a = 5.0$, $w = 1.5$, $\tau_r = 5.0$, $\tau_a = 10.0$. The top panel shows the neural activity as a function of time and the bottom panel shows the phase plot of the solution in the $r_1 - r_2$ plane. The initial condition is set as $r_1 = r_2 = 0$. (b) Two stimuli of the same strength $s_1 = s_2 = 1.0$ are delivered in sequence to neuron 1 and 2. s_1 is delivered at $t = 0.0$ and s_2 is delivered at $t = 333.3$. The parameters are chosen as $w = 1.2$ and $A = 0.69$, the rest of the parameters are the same as in (a).

Presenting two stimuli with the same intensity in sequential order sheds further light on the behavior of the network in responding to dynamic stimuli, where two stimuli have the same intensity but presented in sequential order. The appearance of the first stimulus triggered the response of neuron 1 that reaches to a steady state value after a while (Fig 6.1b). The onset of the second stimulus triggers the response of neuron 2 which in turn suppressed the activity of neuron 1 completely after a delay of about $\Delta t \sim 100$. While the two stimuli have comparable intensity, the network gives preference to the novel stimulus.

6.4 Stability analysis

To understand the dynamics of the system, we consider its stability in the presence of two stimuli of the same intensity, assuming $s_1 = s_2 = s_0$. Due to the symmetry, the fixed point has the property that $r_1 = r_2 = r_f$ where $r_f = \Lambda(s_0 - w' r_f)$ and $w' = (w + A)$ is the effective weight matrix. The adaptation current accordingly has the form of $I_{a,1} = I_{a,2} = A r_f$. The Jacobian matrix at the fixed point has the form of

$$J = \begin{pmatrix} -\frac{1}{\tau_r} & -\frac{w}{\tau_r}\Lambda'(x_f) & -\frac{1}{\tau_r}\Lambda'(x_f) & 0 \\ -\frac{w}{\tau_r}\Lambda'(x_f) & -\frac{1}{\tau_r} & 0 & -\frac{1}{\tau_r}\Lambda'(x_f) \\ \frac{A}{\tau_a} & 0 & -\frac{1}{\tau_a} & 0 \\ 0 & \frac{A}{\tau_a} & 0 & -\frac{1}{\tau_a} \end{pmatrix}, \text{ where } x_f = s_0 - (A + w) r_f .$$

The stability of the symmetric system is determined by the following parameters s_0, A, w, a, b, τ_a, τ_r. By rescaling the time constant, the last two parameters could be reduced to be one independent parameter. a and b determine the shape of Hill's function and the saturation rate as a function of inputs. The intensity of stimulus s_0 determines the active level of the network neurons. In the following sections, we focus on discussing the role of synaptic weights and adaptation in determining the dynamics of the system.

6.5 WTA in a reduced two-dimensional system

In order to further capture the essences that determine the WTA mechanisms we consider a reduced 2-dimensional system where we assume a neuron has no intrinsic adaptation and set $A = 0$. The Jacobian is reduced to $J = \begin{pmatrix} -\frac{1}{\tau_r} & -\frac{w}{\tau_r}\Lambda'(x_f) \\ -\frac{w}{\tau_r}\Lambda'(x_f) & -\frac{1}{\tau_r} \end{pmatrix}$, and $x_f = s_0 - wr_f$, and r_f is the fixed point of the system that follows $r_f = \Lambda(s_0 - wr_f)$. The eigenvalues of the Jacobian are $\lambda_{\pm} = -\frac{1}{\tau_r} \pm \frac{w\Lambda'(x_f)}{\tau_r}$. In the limit when the interactions between the two neurons are weak $w \to 0$, and the eigenvalues $\lambda_{\pm} \to -\frac{1}{\tau_r}$. The system has a stable fixed point where $r_f \to \frac{s_0^a}{s_0^a + b^a}$. When the interaction strength becomes stronger $w \to \infty$, and the fixed point loses its stability if $\lambda_+ > 0$.

We examine the response of the network by delivering stimuli of two different scenarios. In the case of static stimuli, we deliver two stimuli of slightly different intensity. Given a weak inhibitory strength between neuron 1 and neuron 2 (Fig. 6.2a), both neurons are activated and the responses reach a steady state where only a slight difference is observed between the two neurons. The differences between the neural responses increase as the synaptic strength increases. The activity of neuron 1 suppresses the response of neuron 2 completely when w goes beyond a certain threshold value.

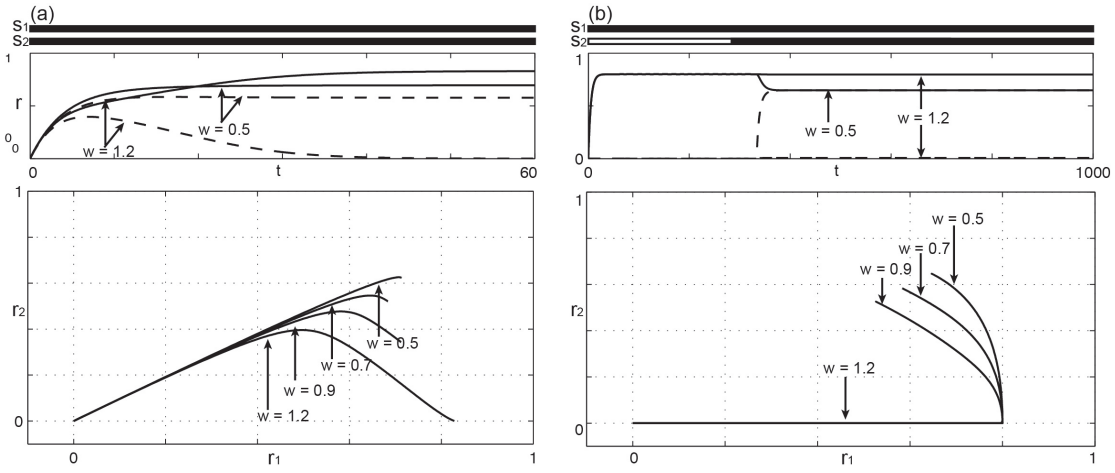

Figure 6.2 The behavior of a two-dimensional neural system. The parameters are chosen as $a = 2.0$, $b = 0.5$, $\tau = 5$. Time courses of the stimuli are shown in black bars. (a) Two stimuli $s_1 = 1.1$ and $s_2 = 1.0$ are simultaneously delivered to neuron 1 and 2. On the top panel, the responses of neuron 1 and 2 as a function of time are shown in solid and dashed line respectively. On the bottom panels the solution of the system is shown in the $r_1 - r_2$ plane (b) Stimuli $s_1 = 1.0$ and $s_2 = 1.0$ are presented at time $t = 0.0$ and $t = 333.3$, respectively.

In the 2-dimensional system, the response to two sequential stimuli of the same strength shows no novelty preference. The presence of s_1 excites the activity of neuron 1. In a network of weak interactions, the presence of stimulus s_2 at a later time suppresses the

response triggered by s_1, and the network eventually settles at a stable state where both neurons respond simultaneously with low firing rate (Fig. 6.2b). The increase of connection weights leads to a structural change in the system's dynamics. When w reaches beyond a certain threshold, the presence of s_2 can no longer suppress the activity at neuron 1 and the system shows little response to s_2. The WTA behavior of the 2-dimensional system resembles that of the 4-dimensional system. However, the 2-dimensional system fails to replicate the novelty preference behavior. The following section reveals that a 3-dimensional system is sufficient for a network to have novelty preference.

6.6 Novelty preference in a reduced 3-dimensional system

To replicate the novelty preference behavior, we introduce a third variable Δi that varies according to the rate difference between the two neurons. The network evolves according to the differential equation set

$$\tau_r \frac{dr_1}{dt} = -r_1 + \Lambda(s_1 - \Delta i - wr_2)$$
$$\tau_r \frac{dr_2}{dt} = -r_2 + \Lambda(s_2 + \Delta i - wr_1)$$
$$\tau_a \frac{d\Delta i}{dt} = -\Delta i + A(r_1 - r_2)$$

In the presence of two symmetric stimuli of the same strength $s_1 = s_2 = s_0$, the system has a fixed point of $r_1 = r_2 = r_f$, $\Delta i = 0$ and r_f satisfies the following relation $r_f = \Lambda(s_0 - wr_f)$. Notice the formula for the fixed point is the same as that of the 2-dimensional system and the existence of the third variable does not change the value of the fixed point. The

Jacobian has a simple form of $J = \begin{pmatrix} -\frac{1}{\tau_r} & -\frac{w}{\tau_r}\Lambda'(x_f) & -\frac{1}{\tau_r}\Lambda'(x_f) \\ -\frac{w}{\tau_r}\Lambda'(x_f) & -\frac{1}{\tau_r} & \frac{1}{\tau_r}\Lambda'(x_f) \\ \frac{A}{\tau_a} & -\frac{A}{\tau_a} & -\frac{1}{\tau_a} \end{pmatrix}$, where $x_f = s_0 - wr_f$ and the characteristic function has the following form

$$\lambda^3 + (\frac{2}{\tau_r} + \frac{1}{\tau_a})\lambda^2 + (\frac{2(1 + A\Lambda'^2)}{\tau_r \tau_a} + \frac{1 - w^2\Lambda'^2}{\tau_r^2})\lambda + (\frac{1 + 2A\Lambda' + (2wA - w^2)\Lambda'^2}{\tau_r^2 \tau_a}) = 0$$

We explored the responses of the network to dynamical stimuli presented in sequential order at various synaptic strengths (Fig. 6.3). With weak synaptic connections, both neurons respond with reduced activities to both stimuli (Fig. 6.3a). Given medium strength of synaptic weights, the novelty preference behavior appears (Fig. 6.3b). The novel stimulus appearing at a later time triggers an increasing activity of neuron 2 and the activity eventually takes over that of neuron 1. The whole network shifts its activity to responding to stimulus 2. The existence of the third variable enables the network to escape from one stable attractor to the other. As the synaptic connections become stronger, the neurons only respond to the first stimulus presented, similar to the case of the 2-dimensional system (Fig. 6.3c).

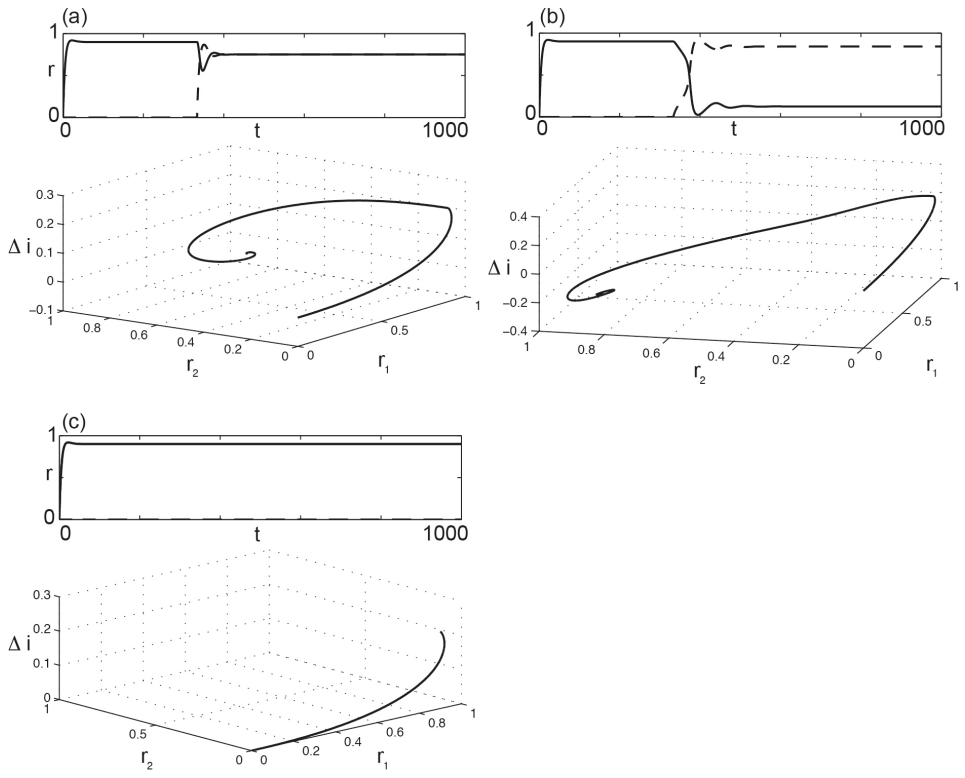

Figure 6.3 A three dimensional system reproduces the WTA selection and novelty preference. The parameters are chosen as $a = 5.0$, $b = 0.5$, $\tau_r = 5$, $\tau_a = 10$ $w = 1.0$. Two stimuli $s_1 = 1.0$ and $s_2 = 1.0$ are delivered to neuron 1 and 2 in a sequential order at time $t_1 = 0.0$ and $t_2 = 333.3$. (a) $A = 0.1$. The top panel shows the time course of the responses of neuron 1 (in solid line) and neuron 2 (dash line) respectively. On the bottom panels the solution of the system is shown in the $r_1 - r_2 - \Delta i$ space, no novelty preference shows up (b) activity shifts to novel stimulus $A = 0.25$ (c) $A = 0.3$ a supercritical Hopf-bifurcation occurs and the neurons start oscillating.

The variable Δi associated with the adaptation current is important for the novelty preference and we demonstrate its role in determining the dynamics of the system. We explore the behavior of the network as the adaptation current increases (Fig 6.4). With small adaptation (Fig 6.4a) the network behaves as that in a 2-dimensional system. The presence of the second stimulus in sequence does not alter the response that is triggered by s_1, and no response shift takes place. The increase of the adaptation enables the

network's ability to shift to a novel stimulus (Fig 6.4b). Further increase in adaptation leads to a supercritical Hopf-bifurcation in the system and the presence of two stimuli triggers the neurons into an out-of-phase stable oscillation (Fig 6.4c).

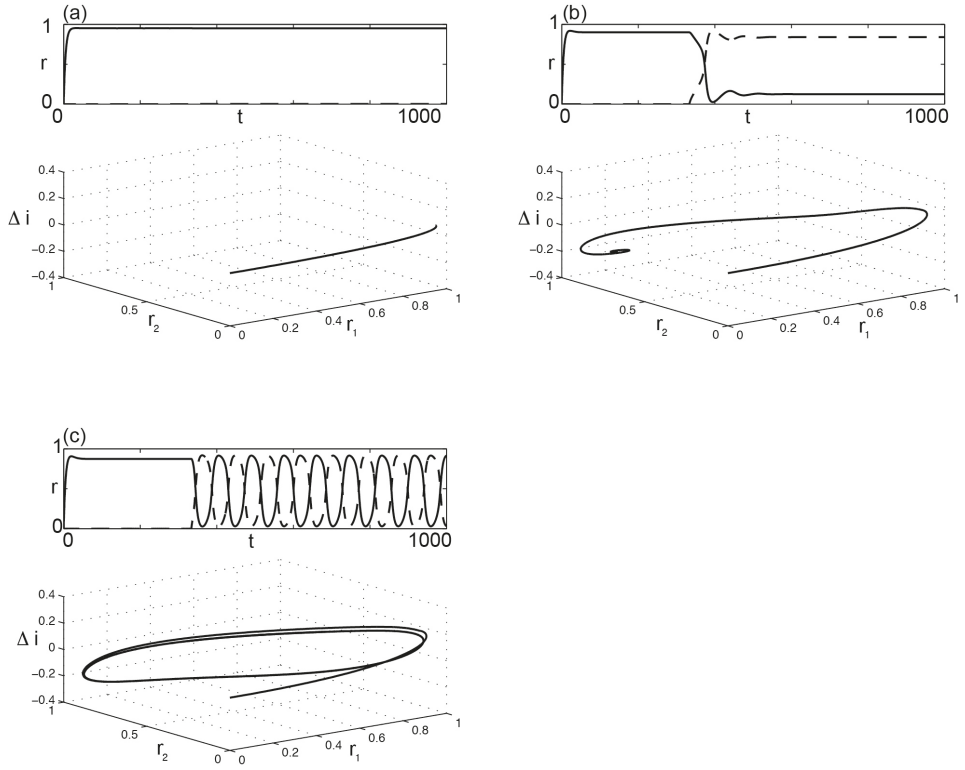

Figure 6.4 The effect of adaptation to the behavior of the neural system. The parameters are chosen as $a = 5.0$, $b = 0.5$, $\tau_r = 5$, $\tau_a = 10$ $w = 1.0$. Two stimuli $s_1 = 1.0$ and $s_2 = 1.0$ are delivered to neuron 1 and 2 in a sequential order at time $t_1 = 0.0$ and $t_2 = 333.3$. (a) $A = 0.1$. The top panel shows the time course of the responses of neuron 1 (in solid line) and neuron 2 (dash line) respectively. On the bottom panels the solution of the system is shown in the $r_1 - r_2 - \Delta i$ space. No novelty preference occurs (b) activity shifts to novel stimulus $A = 0.25$ (c) $A = 0.3$ a supercritical Hopf-bifurcation occurs and the neurons start oscillation.

6.7 Summary

We investigated the dynamics through numerical simulation of the 4-dimensional system and its corresponding images in 2 and 3-dimensional systems. The analysis suggests that triggering WTA mechanisms requires strong synaptic inhibitory connections and a 2-dimesional system is sufficient for this type of stimulus selection. The WTA mechanisms in neural network are also reminiscent of a biological switch that has been discussed much in biological systems such as protein synthesis (Thorn, 1997, Jr et al., 1998). Moreover, we show that a 3-dimensional system is sufficient for novelty detection in the presence of two dynamically presented stimuli. No proof has been made to show that a 3-dimension system is necessary in producing novelty preference behavior. The search through parameter space indicates that a balance of inhibition strength and adaptation are critical for the generation of novelty preference.

6.8 Reference

Aston-Jones, G (1999) The role of locus coeruleus in the regulation of cognitive performance. Science 283:549–554.

Chisum HJ, Fitzpatrick D (2004) The contribution of vertical and horizontal connections to the receptive field center and surround in V1. Neural Networks 17:681-693.

Jr. JEF, Machleder EM (1998) The biochemical basis of all-or-none cell fate switch in xenopus oocytes. Science 280:895-898.

Koch C, Ullman S (1985) Shifts in selection visual attention: towards the underlying neural circuitry. Human Neurobiol 4:219-277.

Knudsen EI (2011) Control from below: the role of a midbrain network in spatial attention. European Journal of Neuroscience 33:1961-1972.

Knudsen E (2007) Fundamental components of attention. Annu Rev Neurosci 30:57-78.

Kohn A (2007) Visual adaptation: physiology, mechanisms, and functional benefits. J Neurophysiol 97:3155-3164.

Mao ZH, Massaquoi SG (2007) Dynamics of winner-take-all competition in recurrent neural networks with lateral inhibition. IEE Trans Neural Netw 18:55-69.

Reynolds JH, Chelazzi L, Desimone R (1999) Competitive mechanisms subserve attention in macaque areas V2 and V4. J Neurosci 19:1736-1753.

Reynolds JH, Heeger DJ (2009) The normalization model of attention. Neuron 51:168-185.

Rabinovich M, Huerta R, Laurent G (2008) Transient dynamics for neural processing. Science 321:48-50.

Tiitinen H, May P, Reinikainen K, Naatanen R (1994) Attentive novelty detection in humans in governed by pre-attentive sensory memory. Nat 372:90-92.

Troy JB, Shou T (2002) The receptive fields of cat retinal ganglion cells in physiological and pathological states: where we are after half a century of research. Progress in Retinal and Eye Research 21:263-302.

Thorn CD (1997) Bistable biochemical switching and the control of the events of the cell cycle. Nonlinear analysis, Theory, Methods and Applications 30:1825-1834.

VanRullen R, Koch C (2003) Competition and selection during visual processing of natural scenes and objects. Journal of Vision 3:75-85.

Wang Y, Major DE, Karten HJ (2004) Morphology and connections of nucleus isthmi pars magnocellularis in chicks (Gallus gallus). J Comp Neurol 469:275-297.

7 Stability of a three-neuron system with delayed feedback

We consider the dynamics of a three-neuron system where neurons form reciprocal connections with each other. Delays are introduced for signal propagations. The stability of the system is discussed. The stable region in the parameter space shrinks as the delay increases. Rich dynamics, such as oscillation and multistability emerge as the parameter reaches beyond the boundary of the stable region.

7.1 Introduction

When forming a network, neurons communicate with each other by sending action potentials along their axons (Goodman BE and Waller SB, 2002). Transmission delays are introduced during the process due to the finite propagation speed of action potentials and the dynamics of neurotransmitter release. Delays can cause very complex dynamics, such as oscillation, multistablity and chaos (Campbell et al., 1995, Foss et al., 1997) in an otherwise stable system. However, the effect of delays to neural systems is poorly understood.

In the central visual pathway, the optic tectum (OT, mammalian superior colliculus) is one of the major targets of retinal efferent. Rhythmic oscillatory bursts (Marin et al., 2007; Goddard et al., 2011) are observed within the isthmotectal feedback loop, formed

by OT and its satellite nucleus (Ipc, Imc and SLu). However, intracellular recordings of individual isthmotectal neurons show no intrinsic oscillatory behavior (Jing et al., 2009). Recordings from the tectal slices indicate delayed signal propagation between isthmotectal elements (Meyer et al., 2008). Here we consider the isthmotectal system as a simplified 3-neuron system, where each neuron represents the OT, Ipc and Imc structure respectively (Fig. 7.1). Propagation delays are introduced. We analyzed the stability as the synaptic efficacies change continuously. The role of delay is also discussed in determining the system's stability. Dynamical behaviors such as stable oscillation, multistablity is observed. Coexistence of an oscillatory attractor and a stable fixed point is observed within a certain parameter range.

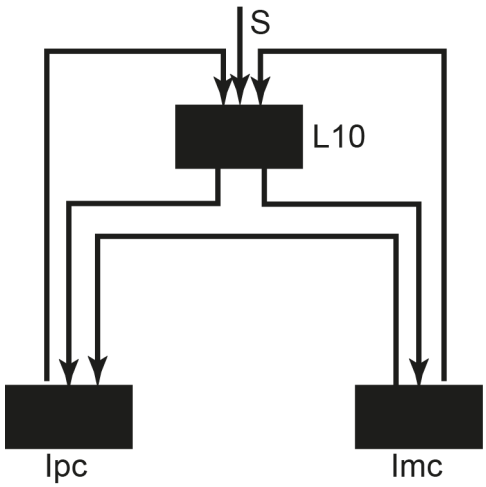

Figure 7.1 The schematics of the simplified three-neuron isthmotectal system: three types of neurons are considered, including tectal layer 10 neurons (L10), parvocellular (Ipc) and magnocellular (Imc) isthmic nucleus. The retina inputs are delivered to the L10 neuron and the L10 neurons further project to Ipc and Imc neurons respectively. The Ipc and Imc neurons send feedback to L10 neuron, forming two closed loops in the network. The Imc neuron also projects to Ipc neuron.

7.2 Isthmotectal system as a delayed 3-neuron system

To understand the dynamics, we simplify the isthmotectal system by considering the optic tectum (OT) and its nuclei isthmi (Ipc, Imc) as single neurons. The connection strengths between neurons are characterized by a weight matrix w_{ij}. The subscript indicates the synaptic efficacy from the *jth* neuron to the *ith* neuron. Propagation delays τ are introduced and we assume a homogeneous distribution of delays for all the connections. The dynamics of each neuron are described by a set of delayed differential equations (DDE)

$$\tau_m \frac{dr_i(t)}{dt} = -r_i(t) + F\left(\sum_j w_{ij} r_j\left(t-\tau\right) + s_i\right) \quad i = 1, 2, 3,$$

where $r_i(t)$ could be interpreted as the firing rate of the *ith* neuron and s_i is the external stimulus delivered to it. $F(x)$ is a transferring function that converts presynaptic neuronal activities into postsynaptic inputs and is normally chosen as a function of sigmoidal shape with the property that $F(0) = 0$. In this study, we choose the transferring function to be a hyperbolic tangent function $F(x) = \tanh(x)$ when $x \geq 0$ and $F(x) = 0$ when $x < 0$. The weight matrix of the isthmotectal system could be specifically written in the form $w_{ij} = \begin{pmatrix} 0 & W_{12} & W_{13} \\ W_{21} & 0 & W_{23} \\ W_{31} & 0 & 0 \end{pmatrix}$. We assume that no self-projections are formed within each neuron group and the diagonal terms in the matrix are set to 0. The synaptic connections between Ipc and Imc groups happen to be unidirectional and we accordingly set $W_{32} = 0$. The system could be simplified further by rescaling the time constant and setting $\tau_m = 1$. The neuronal dynamics then follows the DDE set

$$\frac{dr_i(t)}{dt} = -r_i(t) + F\left(\sum_j w_{ij} r_j\left(t-\tau\right) + s_i\right) \quad i = 1, 2, 3$$

7.3 Stability analysis

In the homogenous case, where no external stimuli are exerted, the system has a trivial fixed point $r_i = 0$. Linearizing the system at the fixed point yields

$$\frac{dr_i(t)}{dt} = -r_i(t) + \sum_j w_{ij} r_j\left(t-\tau\right) \quad i = 1, 2, 3$$

note that $\partial_r F = 1$ at the fixed point. We further impose an initial condition that all neurons are inactive and have the property that $r_i(t) = 0,$ when $-\tau < t \le 0$. Applying a Laplace transformation to the equation set, we get the expression of the system in frequency space

$$(1 + \lambda - e^{-\lambda\tau} w_{ij})\tilde{r}_j(\lambda) = 0$$

The exponential term follows from the Laplace transformation $L\left[r_i\left(t-\tau\right)\right] = \int_0^\infty r_i\left(t-\tau\right) e^{-\lambda t}\, dt = e^{-\lambda\tau}\tilde{r}_j$, where λ is the characteristic frequency of the system and $\tilde{r}_j$ is the function of neuron activity in the time domain. The weight matrix is assumed to be stationary over time. A non-trivial solution for the system requires that $\det(1 + \lambda - e^{-\lambda\tau} w_{ij}) = 0$. Written explicitly, we have the characteristic equation

$$(1+\lambda)^3 - \alpha(1+\lambda)e^{-2\lambda\tau} - \beta e^{-3\lambda\tau} = 0$$

where α and β are reduced parameters, satisfying $\alpha = W_{23}W_{32} + W_{12}W_{21} + W_{31}W_{13}$ and $\beta = W_{23}W_{31}W_{12} + W_{13}W_{32}W_{21}$. Given $W_{32} = 0$, we have a further simplified version of $\alpha = W_{12}W_{21} + W_{31}W_{13}$ and $\beta = W_{23}W_{31}W_{12}$. It turns out that the stability of the system is

determined by 3 effective parameters α, β, τ, two of which are derived from the synaptic connections and the other one from the delay.

Substituting $\lambda = 0$ into the characteristic equation we get the boundary of the stable region where α and β obey the relation

$B_1: \ 1 - \alpha - \beta = 0$.

Further analysis shows (Belair and Dufour, 1996) that λ has no real positive value when $\alpha < 1 - \beta$ if $\beta \geq -2$ and $\alpha < 3\left|\beta / 2\right|^{2/3}$ if $\beta < -2$. This particular boundary is independent of the delay τ.

We then get the boundary of the stable region where λ has a purely imaginary root by substituting $\lambda = i\omega$ into the characteristic function and get the real part and the imaginary part of the characteristic equation respectively as

$$\left(1 - 3\omega^2\right)\cos\left(3\omega\tau\right) + \left(\omega^3 - 3\omega\right)\sin\left(3\omega\tau\right) - \alpha\left(\cos\left(\omega\tau\right) - \omega\sin\left(\omega\tau\right)\right) - \beta = 0$$
$$\left(3\omega - \omega^3\right)\cos\left(3\omega\tau\right) + \left(1 - 3\omega^2\right)\sin\left(3\omega\tau\right) - \alpha\left(\omega\cos\left(\omega\tau\right) + \sin\left(\omega\tau\right)\right) = 0$$

We can solve α and β as a function of ω and the boundary curves have the form

$$B_2: \begin{cases} \alpha = \dfrac{\left(3\omega - \omega^3\right)\cos\left(3\omega\tau\right) + \left(1 - 3\omega^2\right)\sin\left(3\omega\tau\right)}{\omega\cos\left(\omega\tau\right) + \sin\left(\omega\tau\right)} \\ \beta = \dfrac{\left(1 + \omega^2\right)\left(\left(\omega^2 - 1\right)\sin\left(2\omega\tau\right) - 2\omega\cos(2\omega\tau)\right)}{\omega\cos\left(\omega\tau\right) + \sin\left(\omega\tau\right)} \end{cases} \quad \text{if } \omega \neq -\tan(\omega\tau)$$

and

$$B_3:\ \alpha = \frac{\sin(3\omega\tau)}{\omega\cos(2\omega\tau)-\sin(2\omega\tau)}\beta + \frac{3\omega-\omega^3}{\omega\cos(2\omega\tau)-\sin(2\omega\tau)}$$

if $\omega = -\tan(\omega\tau)$

In the parameter plane, we show the stability boundary curves in black lines for delays of different values (Fig. 7.2 a-c). We also solve the characteristic equations numerically and show in shaded areas where the maximum real parts of the solution have negative values. As the delay increases, the shaded area shrinks and the stable point is more likely to lose stability. The maximum real part of the solution is shown in Fig. 7.2 d-f.

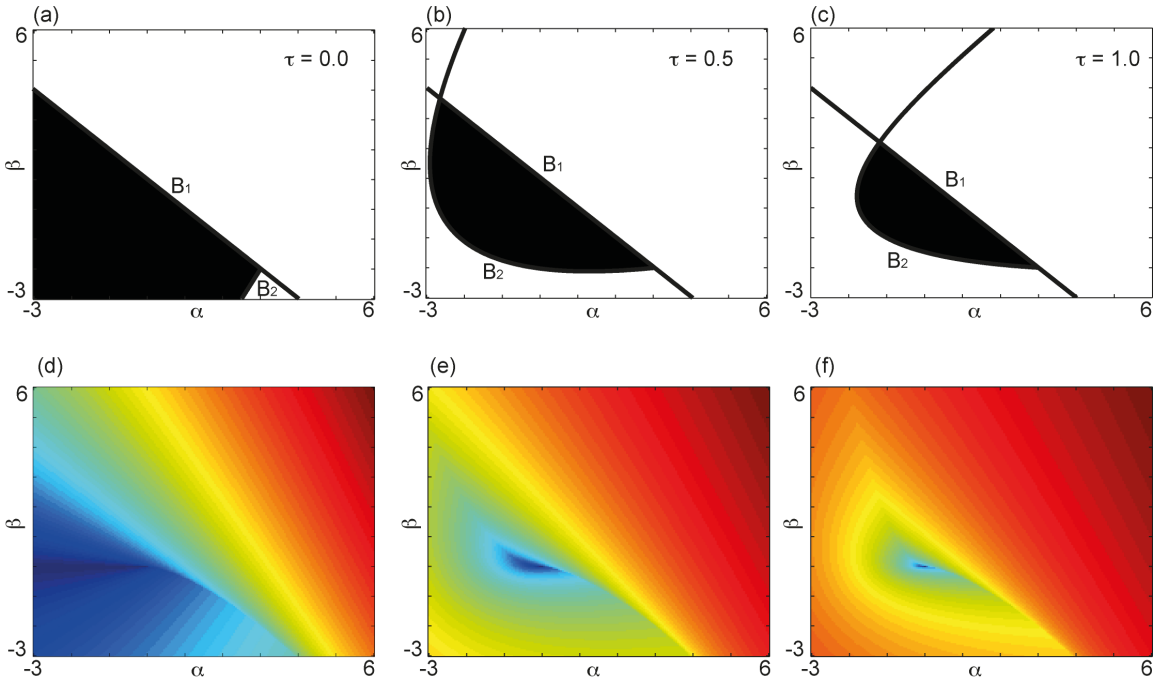

Figure 7.2 Stability analysis of the 3-dimensional system (a) The stability region in $\alpha-\beta$ plane when $\tau=0$. The black lines show the analytical solution of the stable boundaries labeled as B_1 and B_2 respectively. (b) and (c) show the stable region in $\alpha-\beta$ plane when $\tau=0.5$ and $\tau=1.0$. (d)-(f) show the maximum real part of the solution to the characteristic equation. Color coded in a way that red indicates a large value and blue indicates a small value.

7.4 Bifurcations

We assume that the mutual connection between L10 and Ipc neurons is symmetric and $W_{12} = W_{21} = w$. The L10→Imc projection is chosen to have the same strength as that of L10→Ipc projection and $W_{31} = w$. The feedback from Imc is assumed to be inhibitory and is chosen to be negative. The effective parameters are therefore $\alpha = w^2 + wW_{13}$, $\beta = w^2 W_{23}$, and the two parameters are now independently determined by the two feedback connections Imc→L10 and Imc→Ipc. With a weak inhibitory Imc→Ipc connection, the system responds to RGC input of a constant value by reaching to a steady state where each neuron has a constant firing rate (Fig. 7.3).

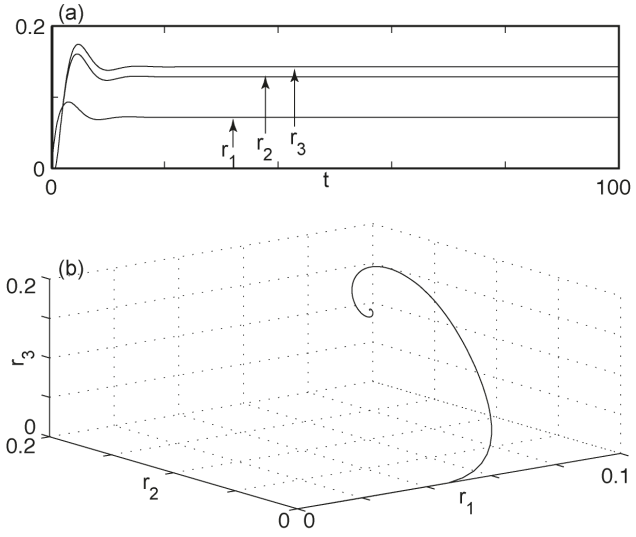

Figure 7.3 The stable steady-state behavior of the system. The parameters are chosen as $w = 2$, $W_{23} = -0.1$ and $W_{13} = -2.0$. The effective parameters are $\alpha = 0.0$ and $\beta = -0.4$. The initial condition is set as $r_i = 0.0$ when $-\tau \le t < 0$. A constant input is delivered to the L10 neuron and $s_1 = 0.1$ (a) The time course of the neural activity (b) the trajectory of the solution in the $r_1 - r_2 - r_3$ space.

As the inhibitory connection strength of Imc→Ipc increases the stable fixed point loses its stability by crossing the boundary B_2 and stable oscillation occurs via supercritical Hopf-bifurcation. The stimulus triggers the activity of L10 neurons, which in turn excite the activity of Ipc and Imc neurons after a certain period of delay. The activity of Imc neurons then exerts a much stronger inhibition on the Ipc neurons. The activity of L10 neurons is accordingly reduced, which leads to a decrease of the Imc inhibitory feedback. The interactions between excitation and delayed inhibition result in the oscillation of the system. The oscillation shows a phase delay among the oscillatory behaviors of the three neurons. The oscillation of L10 and Ipc neurons show comparable amplitudes.

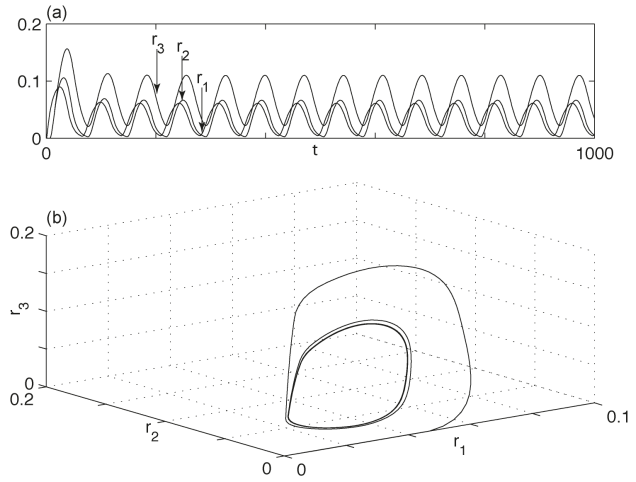

Figure 7.4 Oscillatory behavior with strong Imc→Ipc inhibition. The parameters are chosen as $w = 2$, $W_{23} = -0.6$ and $W_{13} = -2.0$. The effective parameters are $\alpha = 0.0$ and $\beta = -2.4$. The initial condition is set as $r_i = 0.0$ when $-\tau \le t < 0$. A constant input is delivered to the L10 neuron and $s_1 = 0.1$ (a) The time course of the neural activity (b) the trajectory of the solution in the $r_1 - r_2 - r_3$ space. Limiting cycle is formed.

On the other hand, increasing the connection from Imc to L10 neurons also leads to a supercritical Hopf-bifurcation in the system. The increase of W_{13} leads a decreasing of

the effective parameter α. The oscillatory behavior of Imc and Ipc shows comparable amplitude and the activity between Imc and Ipc is almost synchronous (Fig. 7.5).

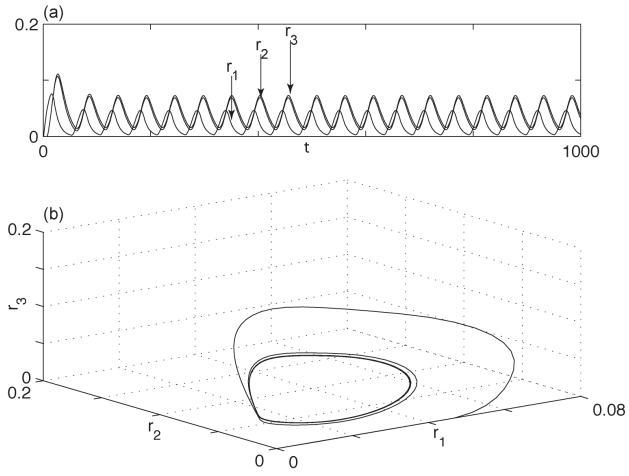

Figure 7.5 Oscillatory behavior with strong Imc→L10 inhibition. The parameters are chosen as $w = 2$, $W_{23} = -0.1$ and $W_{13} = -4.0$. The effective parameters are $\alpha = -4$ and $\beta = -0.4$. The initial condition is set as $r_i = 0.0$ when $-\tau \le t < 0$. A constant input is delivered to the L10 neuron and $s_1 = 0.1$ (a) The neural activity as a function of time. (b) The trajectory of the solution in the $r_1 - r_2 - r_3$ space. A limiting cycle is formed.

7.5 Bistability

Postsynaptic recordings from Ipc neurons reveal the excitatory response to stimulation of Imc nucleus. Here we consider the dynamics of the neural network when the feedback from Imc to Ipc is excitatory. While the synaptic weight W_{23} becomes positive, the effective parameter β becomes positive as well. The effective parameter pair α and β reach the region where the two stability boundaries B_1 and B_2 intersect with each other. Multiple stable attractors could appear in the phase space while the effective parameter pair is carefully chosen within the region. Fig. 7.6a shows a case where two attractors, a stable fixed point and a limit cycle coexist in the $r_1 - r_2 - r_3$ phase space. Dependent on the

initial condition, the neurons might either reach to the stable fixed point or to the stable limit cycle. External noise might induce transition from one attractor to the other (Fig. 7.6b).

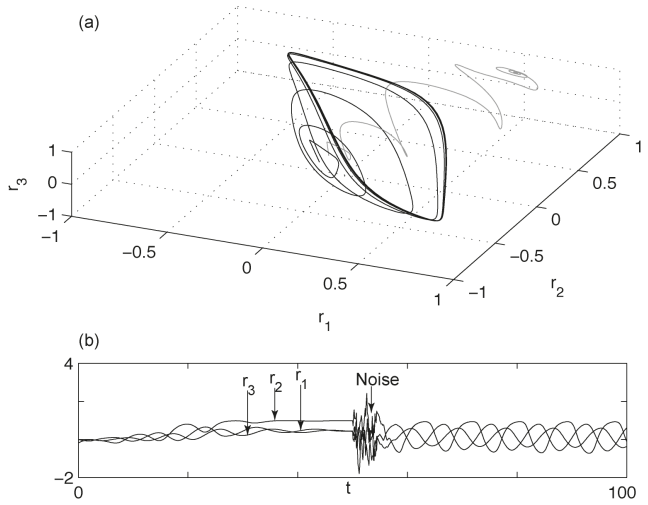

Figure 7.6 Coexistence of oscillation and stable fixed point. The parameters are chosen as $w = 1.0$, $W_{23} = 4.0$ and $W_{13} = -1.3$, $\tau = 2.0$. The effective parameters are $\alpha = -0.3$ and $\beta = 4.0$. A constant input is delivered to the L10 neuron and $s_1 = 0.1$. No rectification is considered in the transfer function. (a) The trajectory of the solution in the $r_1 - r_2 - r_3$ space. A limiting cycle is formed. For the stable fixed point (gray line) the initial condition is set as $r_1 = 0.0$, $r_2 = -0.2$, $r_3 = 0.0$ when $-\tau \le t < 0$. An initial condition of $r_1 = 0.0$, $r_2 = -0.3$, $r_3 = 0.0$ leads to the limiting cycle (black line). (b) A perturbative noise transits the system from the stable fixed point to the state of stable oscillation.

7.6 Reference

Blair J, Dufour S (1996) Stability in a three-dimensional system of delay-differential equations. Canadian applied mathematics quarterly 4:135-156.

Campbell SA, Belair J, Ohira T, Milton J (1995) Complex dynamics and multistability in a damped harmonic oscillator with delayed negative feedback. Chaos 5:640-645.

Foss J, Moss F, Milton J (1997) Noise, multistability and delayed recurrent loops. Phys Rev E 76:708-711.

Goodman BE, Waller SB (2002) Propagation of action potentials in myelinated vs. unmyelinated neurons. Advan in Physiol Edu 26:222-223.

Goddard CA, Sridharan D, Huguenard JR, Knudsen EI (2011) Gamma oscillations are generated locally in an attention-related midbrain network. Neuron 73:567-580.

Marin G, Salas C, Sentis E, Rojas x, Letelier JC, Mpodozis J (2007) A cholinergic gating mechanism controlled by competitive interactions in the optic tectum of the pigeon. J Neurosci 27:8112-8121.

Meyer U, Shao J, Chakrabarty S, Brandt SF, Luksch H, Wessel R (2008) Distributed delays stabilize neural feedback systems. Biol Cybern 99: 79-87.

Shao J, Lai D, Meyer U, Luksch H, Wessel R (2009) Generating oscillatory bursts from a network of regular spiking neurons without inhibition. J Comput Neurosci 27:591-606.